Frida Jerve

Advanced experimental analysis of a small-scale prototype with noble gases for the future upgrade of the detector cooling system at CERN

Master's thesis in Mechanical Engineering
Supervisor: Armin Hafner
Co-supervisor: Luca Contiero
June 2023

Master's thesis

NTNU
Norwegian University of Science and Technology
Faculty of Engineering
Department of Energy and Process Engineering

◉ NTNU
Norwegian University of
Science and Technology

Frida Jerve

Advanced experimental analysis of a small-scale prototype with noble gases for the future upgrade of the detector cooling system at CERN

Master's thesis in Mechanical Engineering
Supervisor: Armin Hafner
Co-supervisor: Luca Contiero
June 2023

Norwegian University of Science and Technology
Faculty of Engineering
Department of Energy and Process Engineering

NTNU
Norwegian University of
Science and Technology

Preface

This thesis is a Master's thesis in Sustainable energy systems at NTNU for the Department of Energy and Process Engineering as a part of the study program Mechanical Engineering. It was carried out in the spring of 2023 as a continuation of the project thesis written in the fall of 2022.

The thesis is based on work currently being done at CERN, the European Organization for Nuclear Research, in cooperation with NTNU. They are looking into new cooling technologies to upgrade their systems.

I want to thank my supervisor, Professor Armin Hafner, for the opportunity to write this thesis. And also for a lot of help and direction with the thesis. I would also like to thank my co-supervisor Luca Continero for his help with the hybrid heat cycle and his work with his Ph.D. thesis; it has been of great help and inspiration.

Lastly, I want to thank my friends and family for making all these years in Trondheim so great. Studentersamfundet will forever hold a special place in my heart.

Abstract

As part of the High-Luminous upgrade of the Large Hadron Collider at CERN in 2026, there are new requirements for cooling the detectors in the interaction points. The current system uses CO_2 as a refrigerant, and the new requirements are beyond the cooling capabilities of CO_2. Krypton is currently being studied as a refrigerant for the new system. This thesis looks at the requirements for the cooling system, given the demands for stability and the harsh environment surrounding the detectors. Then it looks into the current cooling system and how it fulfills the requirements. The final part of the theory assesses Krypton as a refrigerant and how the suggested new system operates.

A simplified version of the new system has been simulated using CO_2 as a refrigerant in Modelica. As a supplement to this, a mathematical simulation using Matlab has been made that uses target equations to simulate the heat cycle. This has also been made to assess how the system is affected by different flow areas in the motive nozzle in the ejector.

Both simplified systems work for the given operating conditions, a transcritical system with a given evaporation load representing the detector heat. The Matlab model does not calculate the ejector's physical properties correctly; this results in a different vapor quality out of the ejector than the one in the Modelica model. This difference affects the liquid mass flow rate and the entire passive loop. The changes in flow area in the motive nozzle decrease the vapor quality with increasing flow area. This result is the same effect as an adjustable position nozzle, but the response in the system is more significant than expected for small changes in the flow area. The mathematical model is only applicable for the given operating conditions. The recommendation for further work would be to investigate the optimized design for the motive nozzle.

The detectors at CERN are in an experimental cave that is closed off; it is, therefore, essential to have accurate measuring data. There has been an investigation into different inaccuracies in temperature and pressure sensors to analyze the effect of inaccurate measuring data.

The first method to look at this was to keep one measurement unchanged and change the other. This resulted in significant changes in enthalpy for many of the measurements since the calculations changed the phase state.

The other method looks at the resulting uncertainty in the heat transfer rate on the refrigeration side of the gas cooler. This showed that the temperature sensors had the most significant effect on the uncertainty of the heat transfer rates. Therefore the recommendation is to allocate more resources to invest in more precise temperature sensors.

Sammendrag

Som en del av High-Luminous oppgraderingen av Large Hadron Collider ved CERN i 2026, er det nye krav til kjøling av detektorene i interaksjonspunktene. Det nåværende systemet bruker CO_2 som kjølemiddel, og de nye kravene er utenfor kjøleevnen til CO_2. Krypton studeres for tiden som kuldemedium for det nye systemet. Denne oppgaven ser på kravene til kjølesystemet, gitt kravene til stabilitet og de krevende omgivelsene rundt detektorene. Deretter ser den på dagens kjølesystem og hvordan det oppfyller kravene. Den siste delen av teorien vurderer Krypton som et kjølemiddel og hvordan det foreslåtte nye systemet fungerer.

En forenklet versjon av det nye systemet er simulert med CO_2 som kjølemiddel i Modelica. Som et supplement til dette er det laget en matematisk simulering ved hjelp av Matlab, som bruker mållikninger for å simulere varmesyklusen. Dette er gjort for også å vurdere hvordan systemet påvirkes av ulike strømningsområder i driverdysen i ejektoren.

Begge de forenklede systemene fungerer for de gitte driftsforholdene, et transkritisk system med en gitt fordampningsbelastning som representerer detektorvarmen. Matlab-modellen klarer ikke å beregne de fysiske egenskapene inni ejektoren riktig, dette resulterer i en annen dampkvalitet ut av ejektoren, enn den i Modelica-modellen. Denne forskjellen påvirker væskemassestrømmen og dermed hele den passive sløyfen. Endringene i strømning i driverdysen reduserer dampkvaliteten med økende strømningsareal. Dette resultatet er den samme effekten som en justerbar posisjonsdyse, men responsen i systemet er større enn forventet for små endringer i strømningsarealet. Den matematiske modellen er kun anvendelig for de gitte driftsforholdene. Den videre anbefalingen er å jobbe videre med designet av driverdysen slik at denne er optimalisert.

Detektorene ved CERN befinner seg i en eksperimentell hule som er avstengt, det er derfor viktig å ha nøyaktige måledata. For å analysere effekten av unøyaktige måledata har det vært gjort en undersøkelse av ulike unøyaktigheter i temperatur- og trykksensorer.

Den første metoden som ble brukt for å se på dette var å holde den ene målingen uforandret og endre den andre. Dette resulterte i store endringer i entalpi for mange av målingene siden fasetilstand ble endret i beregningene.

Den andre metoden ser på den resulterende usikkerheten i varmeoverførings-hastigheten på kjølesiden av gasskjøleren. Dette viste at temperatursensorene hadde størst effekt på usikkerheten i varmeoverføringshastighetene, derfor er anbefalingen å allokere mer ressurser til å investere i mer presise temperatursensorer.

Table of Contents

List of Figures

List of Tables

Nomenclature

α	Void fraction $[-]$
$\dot{m}$	Mass flow rate $[kg/s]$
η	Efficiency $[-]$

μ	Entertainment ratio $[-]$	
ν	Kinematic viscosity $[cm^2/s]$	
ρ	Density $[kg/m^3]$	
h	Enthalpy $[kJ/kg]$	
p	Pressure $[bar$ or Pa$]$	
Q	Heat load $[W]$	
s	Entropy $[J/K]$	
T	Temperature $[°C$ or K $]$	
x	Vapour fraction $[kg/kg]$	

1 Introduction

1.1 Background

The European Organisation for Nuclear Research (CERN) is an international research center focusing on fundamental particles. CERN is located in Geneva in, Switzerland, and is a collaboration between 22 member countries; Norway is one of them. CERN has over 10 000 employees where 8000 of them are researchers. The main instruments used for the research are particle accelerators and detectors. These allow researchers to study how fundamental particles are created and can give insight into how the universe was constructed, (CERN) (2022a).

In 2026 CERN will begin a major upgrade to the biggest of the particle accelerators, the Large Hadron Collider. This upgrade will conclude in 2029 and will include new detectors and require a new cooling system for these detectors. Since the current refrigerant cannot provide the cooling required, they have begun looking into other refrigerants. Krypton has been chosen as the new refrigerant, and there will be built a test rig using Krypton at CERN and a hybrid cooling cycle test rig using Xenon at NTNU in Trondheim.

As a part of this research, the CERN team from NTNU, including the author of this thesis, went to CERN in October of 2022. We met the people that have developed the current system they have and got their input on that are the most critical requirements. We saw the facilities and how the current cooling systems are operated and controlled. Some key aspects we where introduced to was the importance of stability in the system and how the harsh environment surrounding the detectors affect the system.

1.2 Problem formulation

The background of this thesis is to investigate heat systems under particular requirements. The use of noble gases in these systems is new and needs further research. The scope is to look further into these systems and create insight into how they could work.

The first part of this thesis investigates ejector control strategies for a transcritical heat pump system. This is done by simulation. The next part of the thesis investigates the effects of uncertainty from temperature and pressure measurements.

The ejector simulations could be relevant for others looking into transcritical systems. Especially the assessment of the calculation of the speed of sound in a two-phase flow is of interest.

The uncertainty analysis is relevant for all test facilities. It is crucial for the systems at CERN since the passive loop is closed off and highly dependent on sensor measurements..

1.3 Objective of master thesis

The original objective of this master's thesis was to perform an experimental campaign to test a Xenon hybrid cycle. Therefore the objective for the master thesis is given below:
1. Review of relevant literature, e.g., detector cooling strategies requirements and energy (exergy) analysis methodologies.
2. Perform an experimental campaign of the small-scale prototype while simultaneously modeling the different components
3. Analyze and discuss the simulation and experimental results in terms of the controllability & stability of the cycle
4. Analyze and discuss the control strategy and performance of the ejector design and possible alternative designs
5. Master thesis report including first comparisons (results) as well as a discussion and a summary chapter
6. Proposals for further work

7. Draft scientific paper

The experimental campaign was difficult to perform within this master thesis timeline. The test rig was planned to be built at NTNU, tested at NTNU, and sent to CERN when the testing was finished. For several reasons it was more feasible to build the test rig at NTNU and send it to CERN to do tests there. These changes in plans, changed some of the objectives in this Masters's thesis and the the experimental campaign with numerical calculations and analysis of sensor error in the test rig.

1.4 Thesis structure

The theory chapter looks at the current requirements for a cooling system at CERN, the operation of the current cooling system being used, and the new requirements for the upgrade of the cooling system. Then it looks into noble gases as refrigerants and the current suggested Krypton system. The last part of the theory chapter looks into specific ejector design.

The method chapter is divided into three parts. The first part is how the Modelica model is simulated and the second part is how the Matlab numerical calculations are done. The third part is an uncertainty analysis of temperature and pressure sensors.

The results chapter is divided into five parts. The first and second parts are the results from the Modelica model and the Matlab model. The third part is a comparison between the two models. The fourth part presents the results of different flow areas in the motive nozzle that affect the simulation. The fifth and the last part of this chapter looks at how the uncertainty in temperature and pressure sensors affect enthalpy and heat transfer.

The discussion chapter is divided into the same subchapters as the result chapter and it presents specific recommendations and reflections on the results and how they could have been improved.

The conclusion chapter is a summary of previous chapters, achieved results and discussion of these.

In the chapter for recommendation for further works are specific recommendation and reflections given.

2 Theory

The theory chapter looks at the conditions surrounding the hybrid heat pump at CERN, the current system they use and what the requirements for the future system is. Then it looks into the refrigerants that are proposed and the current proposal for a new hybrid heat pump. This is the background for the simplified model that is being used later in the thesis.

Large parts of this theory chapter is referenced from this authors project thesis. The project thesis was written about the development of the Modelica model and sensor error, therefore the background theory is in large parts the same, Jerve (2022).

2.1 The Large Hadron Collider

The Large Hadron Collider (LHC) is the biggest particle accelerator at CERN, and it is 27 kilometers long and buried 100 meters underground. Along the accelerator are several detectors (ATLAS, CMS, ALICE, and LHCb). These are places at the interaction points (IP) where the beams of particles are brought to a collision.

There are two main sets of detectors in the interaction point. The first is the central detector, often referred to as the particle tracker or "the tracker." The tracker identifies the particle by charge and momentum and points to the exact point in space where it is located. The other part of the detectors is the calorimeters, which measure the energy associated with each particle. There is a

last part of the detectors called the Muon detectors, which identify Muons, the elusive particles that the tracker or the calorimeter can not correctly measure. Figure 1 is a detailed overview of the CMS interaction point. In this paper, the focus will be on the particle tracker, Petagna et al. (2019).
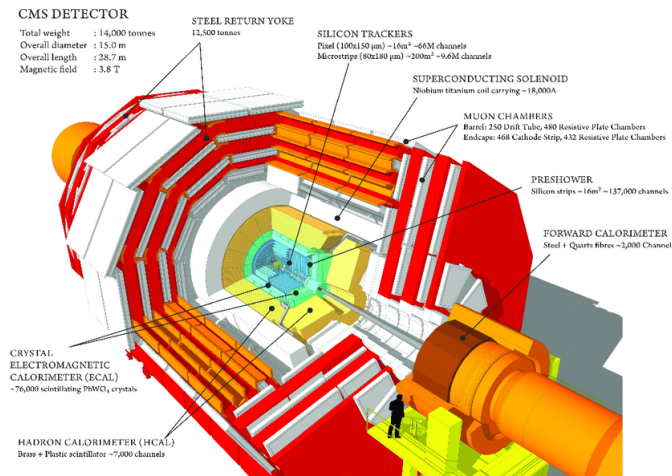
Figure 1: Overview of the CMS detectors.

The tracker contains a silicon-based semiconductor radiation detector comprising two different technologies: the "silicon Pixel" module and the "silicon Strip" module. The pixel module is matrices of pixels directly connected to the data reading and control circuits. Because this provides an exact measurement, this module is more expensive, requires more energy, and has a larger mass. This module is, therefore, only used in the innermost part of the tracker where precise measurements are crucial. The outer parts of the tracker consist of the strip module. Figure 2 shows an illustration of how the silicon pixel module is connected to the data reading modules and the minuteness of the size of each pixel detector.
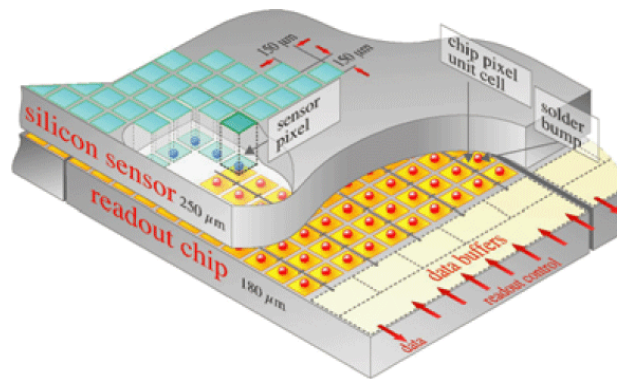
Figure 2: Silicon Pixel Module

There are constraints when it comes to the physical solution for cooling the trackers. The configuration for the whole IP is extremely tight to ensure a vacuum and sufficient coverage of detectors. This means that the pipes must have a small diameter as possible while still providing the cooling required. As there is a risk of asphyxiation with leakage of R744 (CO_2), Eckert et al. (2022), the primary system has to be installed on the surface. This results in a long distance between the cooling plant and the local heat sink. The pressure drop in the tubes is going to have a significant effect on the efficiency of the system.

The secondary part of the system, the cooler in contact with the detectors, referenced to the passive loop for the rest of this article, must be run without manual control or supervision. This is because the LHC has to be closed off during experiments due to radiation from the collisions. The environment for the passive loop is high in radiation and a strong magnetic field. To avoid oil degradation from radiation, the system should be oil-free, Ferrari et al. (2019).
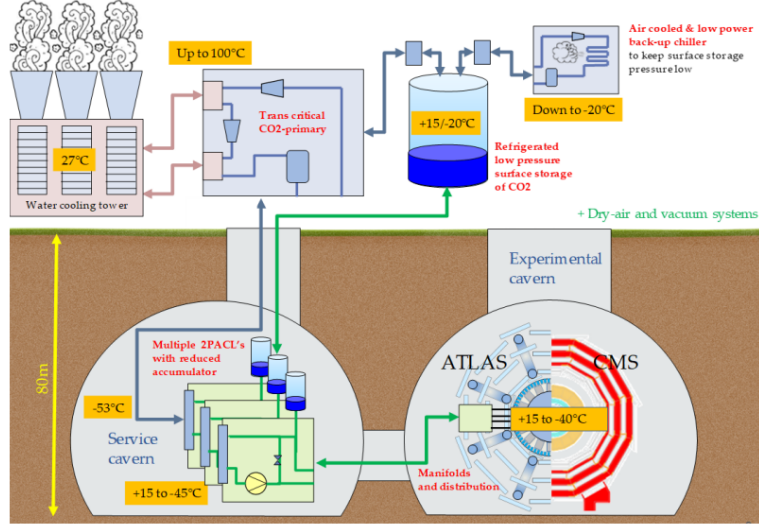
Figure 3: Overview of distance in the cooling systems (ATLAS and CMS)

Source: Barroca et al. (2021)

Figure 3 shows an outline of the setup for the interaction point CMS and ATLAS. The setup is similar for all interaction points, where there is a long distance between the passive loop and the primary cooling system. The right side is in the experimental cavern 100 meters underground and is not accessible when experiments run. This also means that this part of the system has to be maintenance-free for the larger part of the year. The left side is the primary system set up on the surface, Barroca et al. (2021).

All the detectors must be maintained at a level below 0 °C at all times. The internal levels are most exposed to radiation and need to be cooled below - 30 °C for the current radiation levels. With the future update, this will require more cooling,Petagna et al. (2019). The reason for this requirement is that the detectors are exposed to high radiation levels. When the collision happens at the interaction point, a short exposure of high intensity radiation damages the silicon detectors. This leads to the degradation of the charge collection efficiency. To avoid further damage, the detectors must be kept at a cooled temperature at all times, Fretwurst et al. (1994).

2.2 The current system for LHCb-VELO

The current system is a two-phase CO_2 system. The two-phase system is more efficient than single-phase cooling because it requires less flow. This is important in this system because the hardware for cooling needs to be minimized as there are space limitations, Verlaat, Beuzekom et al. (2008).

The system described in more detail here looks at the LHCb-VELO and the AMS-Tracker cooling system. The LHCb is one of the interaction points on the LHC, and the VELO is the new Vertex Locator, which is a pixel detector. The AMS-Tracker is the silicon tracker previously described, AMS is an abbreviation for Alpha Magnetic Spectrometer Experiment.

The small tubes in two-phase cooling require less flow, so when the pressure drop remains low, the tube can almost become isothermal. To have the smallest tube, it is required to have fluids that evaporate under high pressure. This type of fluid also allows for larger pressure drops since it is

related to absolute pressure and less significant for high-pressure fluids. This also makes the heat transfer capability high, Verlaat, Beuzekom et al. (2008).

In a tube, there will always be a pressure drop in the direction of the flow. In a two-phase flow, this will result in a decrease in temperature due to a decrease in saturation pressure. Two-phase flow also have the benefit of reduced mass flow and a smaller temperature gradient along the detector. Single-phase flow will increase temperature due to the lower heat capacity. Since the temperature of the tube walls is single-phase, there will be a big difference in those regions where the fluid is decreasing temperature in two-phase, and the wall temperature is still increasing. This will happen at a certain vapor quality, where the liquid no longer touches the walls, and there will be poor heat transfer resistance. This effect is called dry-out and is a risk of a less effective evaporator when using two-phase fluids because of the change in heat transfer coefficient. The dry-out zone is shown in figure 4. To reduce this risk, evaporation has to start at the active detector inlet temperature. To ensure this, the liquid can not be subcooled, and there can not be any liquid superheating, Verlaat, Beuzekom et al. (2008).
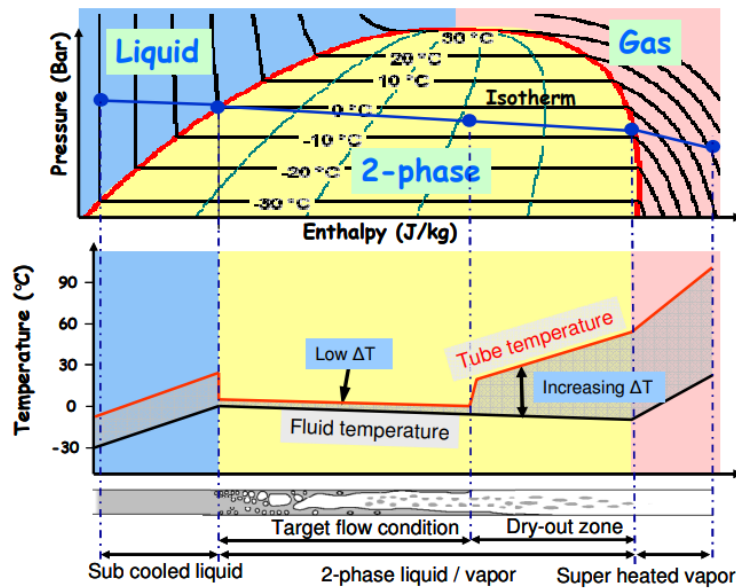
Figure 4: Dry-out zone for two-phase flow

Source: Verlaat, Beuzekom et al. (2008)

There are two methods to get the two-phase condition into the system, visualized in figure 5. The first is a vapor compression system, where an evaporator tube is used directly in a refrigeration cycle. This type of system is used in the Atlas inner detector. The other method is a liquid pumped system with an external cold source which is the system used at the LHCb-VELO thermal control system. This is called the 2-phase Accumulator Controlled Loop (2PACL). The pumped system uses cold transfer lines and therefore requires insulation, while the other uses warm transport lines. Insulation will take up extra space, but since the tubes are so small in diameter, this is a minor problem. The challenge with the vapor compression solution is that there are heaters in the detector to boil off the remaining liquid, and it requires an oil-free compressor which is hard to find. This makes the current solution, the 2PACL, a more suitable choice with its passive evaporator, Verlaat, Beuzekom et al. (2008).
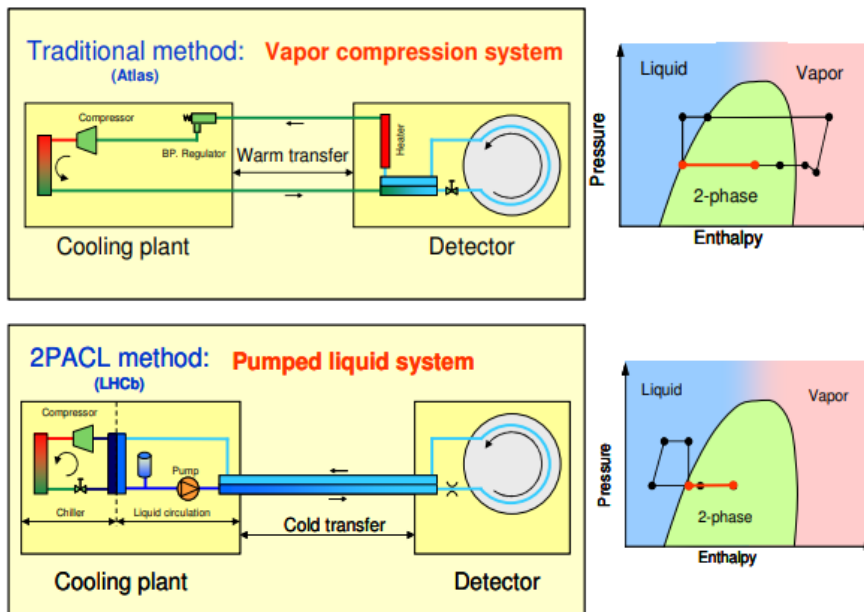
Figure 5: Two-phase cooling at CERN

The 2PACL was developed for this specific system but was later implemented to cool ATLAS, Verlaat and other (2017). A flow diagram for the system is presented in figure 6 and figure 7 show the associated P-H diagram for the system. The main benefit of this system is that it creates stable temperatures for the detectors without active hardware components like valves or heaters inside the experimental cavern. This method uses a capillary pumped loop applied in satellite cooling and is an evaporative heat transport system, Verlaat, Beuzekom et al. (2008).
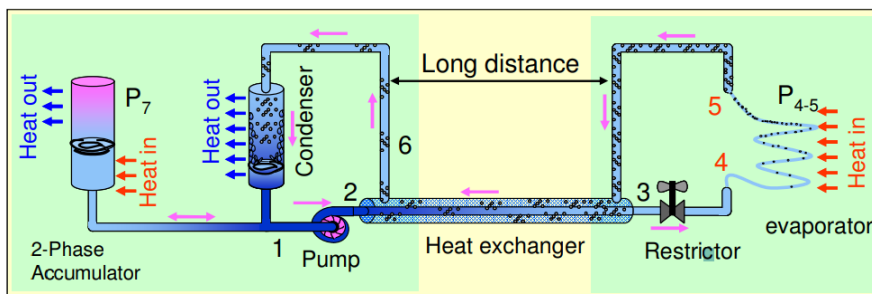
Figure 6: Current cooling system

Figure 7: Log PH diagram for 2PACL system

From the liquid side, the fluid enters the pump at point 1 in the P-H diagram in figure 7. It is pumped up to a certain pressure, still in liquid form, to a heat exchanger between points 2 and 3; this heat will reduce subcooling before the expansion. Point 3 to 4 is the liquid expansion down to the saturation line. Between points 4 and 5, the two-phase fluid takes up heat from the detectors, increasing the enthalpy and the vapor quality. The pumps provide overflow to avoid dry-out; the evaporator outlet can remain partly liquid. From points 5 to 6, the liquid goes back to the heat exchanger, and the heat exchanged from 5 to 6 is the same as from 2 to 3. From 6 back to pint 1 is the condenser. All the nodes 1,4,5 and 6 are kept at the accumulator pressure, represented by P7, Verlaat, Beuzekom et al. (2008).

The evaporator pressure is controlled by the two-phase accumulator, which is installed parallel to the system. The loop pressure is present as long as there is a presence of a saturated mixture and works as long as the chiller can keep the CO_2 outlet of the condenser colder than the accumulator saturation temperature. The pump is fed subcooled liquid and runs free of cavitation. To ensure the evaporator is always evaporating at the saturation temperature set in the accumulator, an internal heat exchanger heats the subcooled liquid, Verlaat, Beuzekom et al. (2008).

The LHC proton beam produces a large amount of radiation when particles collide. The radiation causes an increase in depletion voltage because the silicon crystal lattice is damaged, Beattie et al. (1997). Therefore permanent cooling is needed to avoid further degradation. A silicon temperature of less than -7 °C is sufficient to minimize the effects of the radiation damage. The cooling must also be supplied when the detectors are switched off to avoid degradation, Verlaat, Beuzekom et al. (2008).

If the detectors are switched off, there is no heat supply in the evaporator hence the subcooled liquid will enter the evaporator. The evaporator can become colder than the temperature set point, set by the accumulator, and then the accumulator is no longer able to control the evaportaor temperature. The detectors can become too cold if the set point is uncontrolled. To control this, the tubes in the heat exchanger, which are the transfer lines, are concentric. This means that the environmental heat will only affect the return line. The insulation on these tubes is tuned so there is enough heat from the surroundings to avoid subcooling even when the detectors are turned off, Verlaat (2007).

To avoid damage to the detectors and even cooling, the start-up phase of the heat pump is crucial. Pressure drops from the vapor passing through the pipes can occur, and if there is no liquid in the pumps, they will not start. To avoid this, the accumulators can be heated up to turn the fluid into a single-phase liquid. It will be heated to above the saturation pressure, so all the CO_2 is liquefied. From there, the pump can start without a problem, Verlaat (2007).

The VELO thermal control system (VTCS) is a cascade system of three hydraulic systems. A primary system with water, a secondary system with Freon (R507A), and a tertiary system with CO_2 closest to the detector, Verlaat (2005). A schematic of the system is shown in figure 8 The Freon chillers condense the CO_2 vapor and reject the heat to the cold water system at CERN. This is a standard chiller with a gas compressor, water condenser, evaporators, and expansion valves. The Freon chiller's main task is to control the expansion valves for the CO_2. Freon heat exchangers and control the frequency of the compressor between them, Verlaat, Beuzekom et al. (2008).
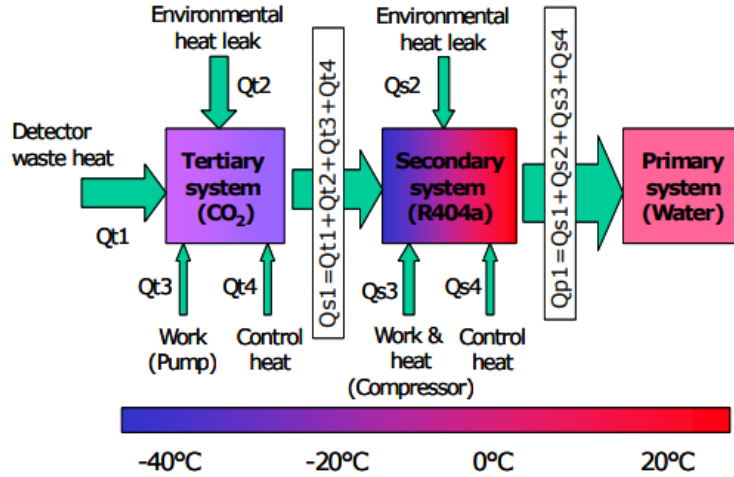
Figure 8: Block scheme for the VTCS cascade system

2.3   The future of LHC

The Large Hadron collider is going through a significant update to prepare for the High Luminosity program (HL-LHC) starting in 2026. The goal is to increase the integrated luminosity by a factor of 10 compared to the current system. The increase in luminosity will increase the capability of the number of collisions that can occur in a given time. This will increase the magnitude of radiation on the detectors, increasing the temperature. The current detectors will be replaced with a new generation of silicon detectors for the upgrade. To keep the new detectors at performance temperatures, there will also be a new cooling system. ATLAS will require a power of 300kW and CMS 500kW, all while ensuring the temperature of the refrigerants in the heat exchangers reaches -53 °C, Apollinari et al. (2015), (CERN) (2022b), Barroca et al. (2021).

2.4   Refrigerants at LHC

2.4.1 CO_2 in the current system

There are several reasons for the choice of CO_2 as a refrigerant in the current system. The first is the European Parliament's resolution to transition from HFCs to natural refrigerants with less climate footprint, European Parliament (2014). CERN has committed to a greener future and therefore sets natural refrigerants as a premise for their cooling systems. The other reason is that CO_2 has a higher latent heat than other HFCs. This means that for a given diameter, the pressure drop for CO_2 is lower for the HFCs, as shown in figure 9. Since there are space limitations in the cooling of the detectors, CO_2 is the best choice.
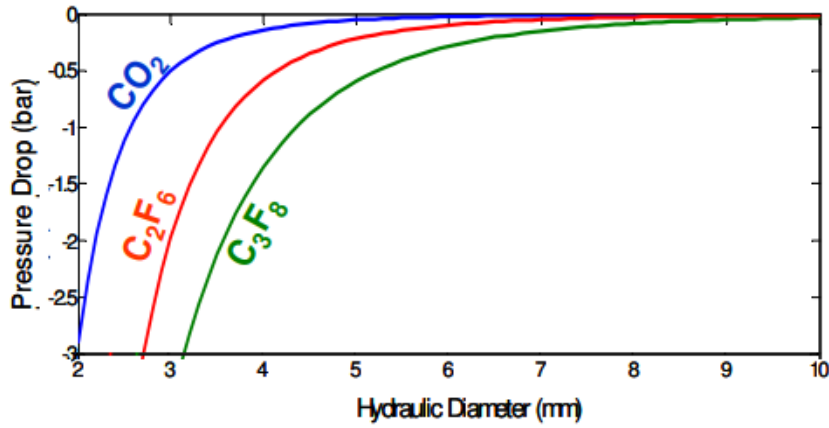
Figure 9: Pressure drop of CO_2, C_3F_8 and C_2F_6 for given tube diameter

As seen in the 2PACL system, CO_2 can be used with an oil-free mechanically pumped loop. CO_2 also has low toxicity, low flammability, and high radiation hardness. Radiation hardness is the ability to withstand ionizing radiation. This is an important property of a refrigerant in a highly radiated environment, Contiero, Barroca et al. (2022).

The HL-LHC requires lower cooling in the future, and CO_2 has a limit of -56 °C, represented by the triple point. When the temperatures required by the detector decreases, the condensing temperature of the chiller is limited by the triple point. This results in not enough subcooling to supply the pump. The conventional CO_2 cooling systems on the market today operate between -40 and -50 °C. Therefore, other options are being looked into, Barroca et al. (2021). For ultra-low temperatures below -56 °C, there are not a lot of options for natural refrigerants. Nitrous oxide (R744A) has a melting point of -91 °C and a critical temperature of 36.5 °C. The critical temperature is similar to CO_2 but has a lower freezing point. Nitrous oxide is a strong oxidizer; small amounts combined with fuel can explode due to heating from adiabatic compression so that the gas reaches decomposition temperatures. Stainless steel and aluminum can act like these fuels; it is therefore not recommended to use R744A in its pure form, Merrill (2008). The combination of nitrous oxide and CO_2, N_2O-CO_2, can have the wanted properties. It is a low-pressure working fluid in the two-phase region with high-pressure-temperature gradients in smaller tubes, Contiero, Barroca et al. (2022).

Another option is hydrocarbons like ethane and ethylene. Ethane has a critical point of 32 °C and a melting point of -182 °C. Ethylene has a critical temperature of 9.2 °C and a melting point of -169 °C. Both of the hydrocarbon's high flammability categories as a 4 in flammability in the NFPA704 hazard diamond, meaning that at normal atmospheric pressure and temperature, they will rapidly or entirely vaporize or could burn quickly.

If the hydrocarbons or R744A were to be implemented in an underground facility, strict safety regimes would be implemented to decrease the risk of explosion and fire.

2.4.2 Krypton and Xenon as refrigerants

The final option reviewed is the noble gases Krypton and Xenon. They are monoatomic, non-flammable, and generally unreactive. Krypton has a critical point of -64 °C and a melting point of -157.4 °C. Xenon has a critical temperature of 15.9 °C and a melting point of -111.8 °C. The noble gases have a high radiation hardness and are suitable for a highly radiated environment, Furtado et al. (2015).
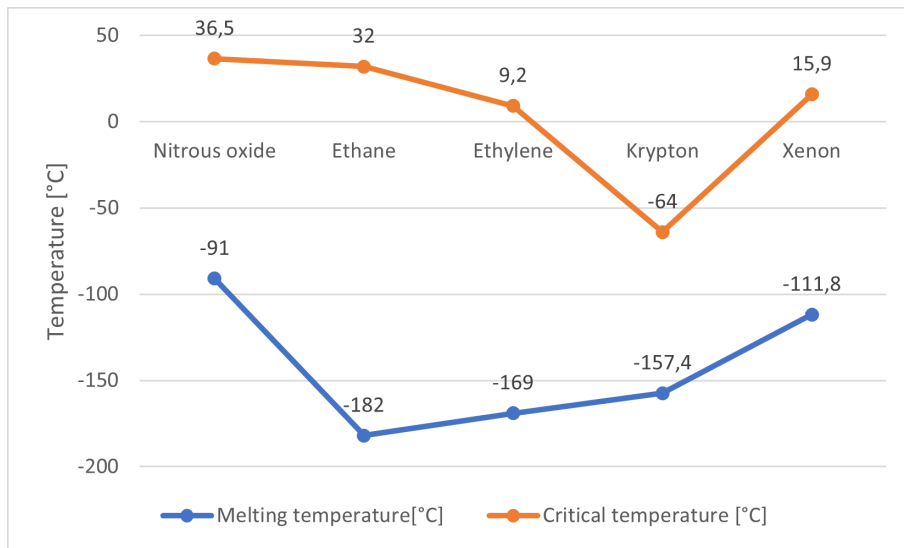
Figure 10: Melting and critical temperature for the refrigerant options
(Illustration made by Jerve 2022)

To decide which one of the refrigerants, that is the best choice for this application, there are two important requirements:

- The best thermal performance with the smallest possible pipe size

- Even temperature distribution over the detectors

To formulate this, the thermal gradients from the sensors, as the heat source, to the cooling pipe, as the heat sink, must be minimized. The pipes have to be small, so they fit the tight space they are placed in, but also to reduce the amount of mass that goes through the pipe. This will reduce the mass that is exposed to radiation, Contiero, Barroca et al. (2022).
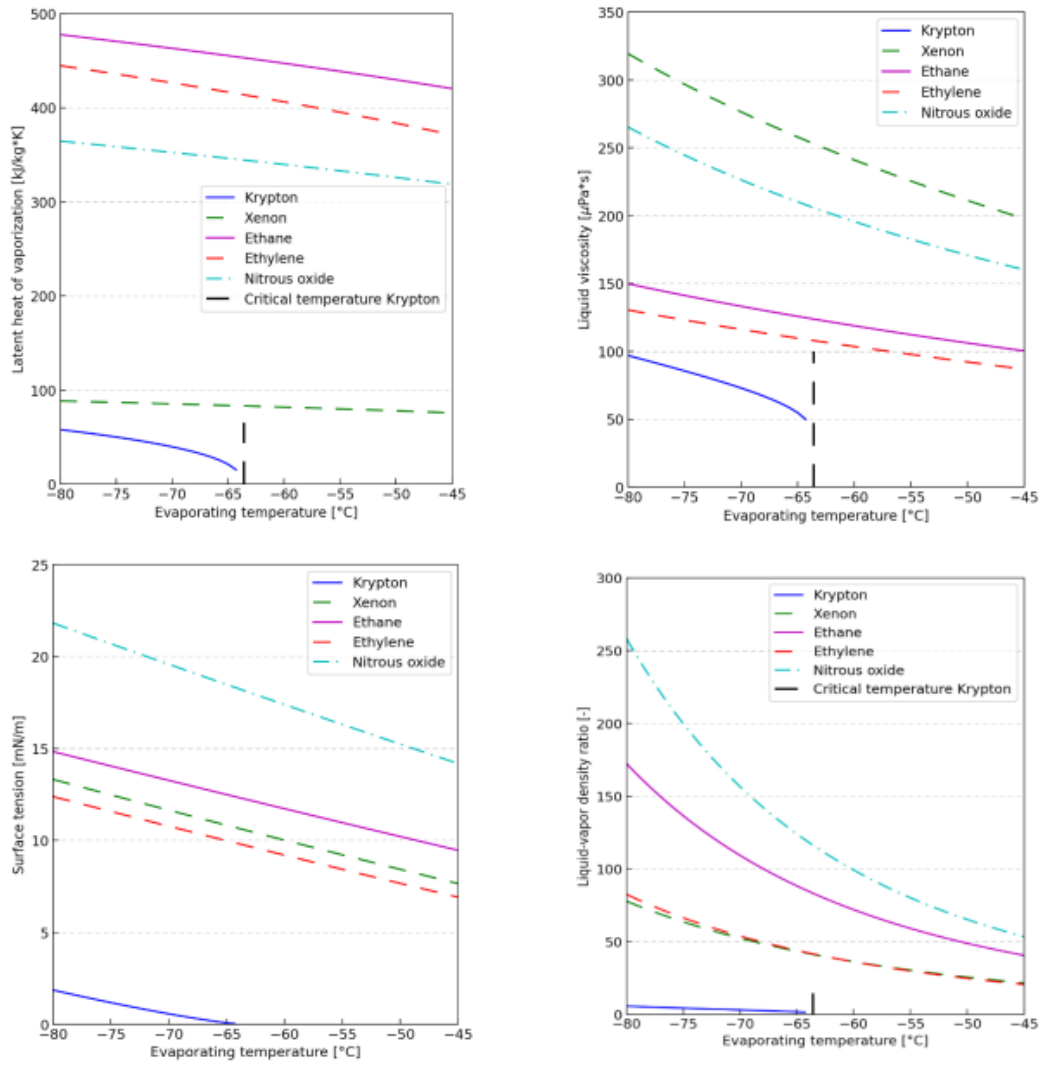
Figure 11: Thermodynamic properties of different refrigerants

Source: Contiero, Barroca et al. (2022)

Figure 11 shows the thermodynamic properties of the different refrigerants. The liquid viscosity is a measure of how easily a fluid flows; the lower the liquid viscosity, the easier the fluid flows. Low liquid viscosity combined with low surface tension assist the boiling process. A large liquid-vapor density ratio would lead to significant pressure drops along the pipes and, therefore, a change in temperature on the evaporator side.

One of the requirements is to have a homogeneous temperature over all the detectors so that all the detectors operate under the same conditions. To ensure this, it is essential to avoid dry-out. The evaporators can achieve this by being flooded to guarantee a two-phase flow and wetted walls; this is done by having a high mass flow rate. Therefore it should be a low latent heat of vaporization, which is how fast the vapor quality increases.

The other requirement is good thermal properties using the smallest pipe diameter. To compare the fluids, it is possible to use the volumetric heat transfer coefficient (VHTC), Petagna et al. (2019).

$$VHTC = \frac{Q}{V_{tube}\Delta T(\Delta P + HTC)} \tag{1}$$

Compared to the calculations for the heat transfer coefficient that accounts for heat flux (Q) and temperature change(Δ T), the VHTC alto takes into account the volume of the pipe (V_(tube), the pressure drop (Δ P) and the heat transfer coefficient (HTC). The change in pressure also accounts for the friction losses along the tube. Verlaat (2013) Figure 12 shows that for the same parameters: L = 2 m, Q = 200 W, T = -80 °C, vapor quality range 0-35%. All the high-pressure fluids preform well; Krypton has the highest VHTC for the smallest pipe diameter, at about 1.8 mm, Contiero, Barroca et al. (2022).
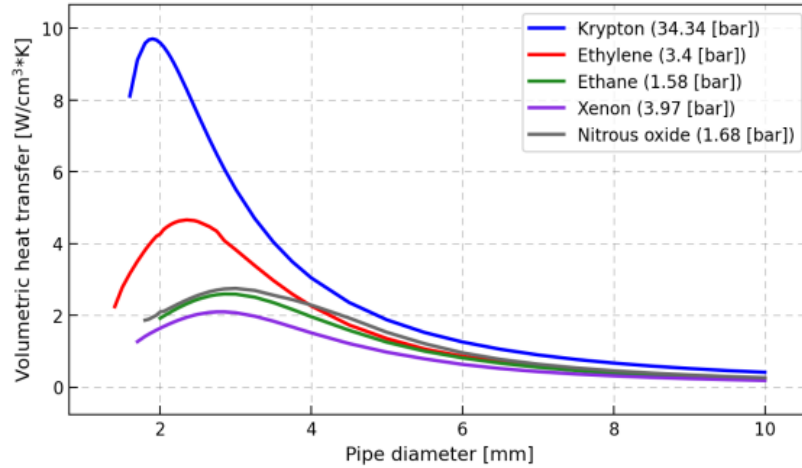
Figure 12: VHTC for different fluids given the same parameters
(L = 2 m, Q = 200 W, T = -80 °C, vapor quality range 0-35%)

Source: Contiero, Barroca et al. (2022)

The pressure losses and resulting temperature drop are relatively low below the critical domain for Krypton; this results in smaller thermal resistance for convection,Contiero, Barroca et al. (2022). This is shown in figure 13 with the same parameters as figure 12.
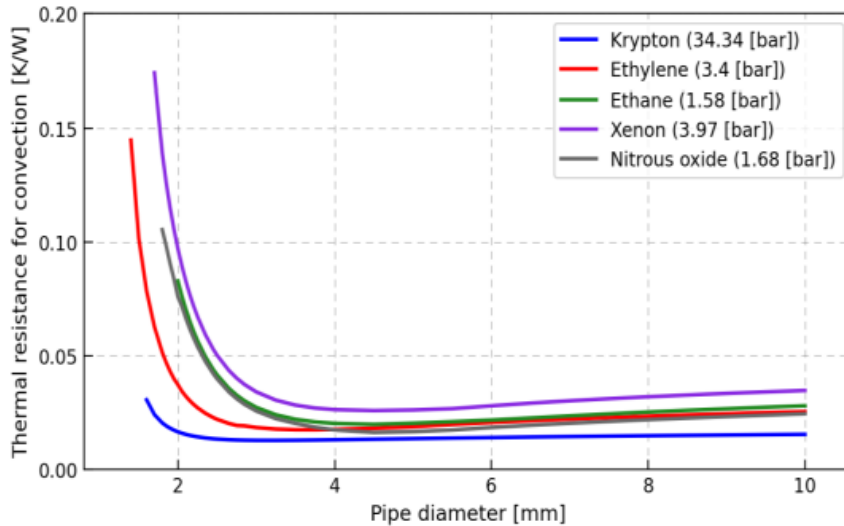
Figure 13: Thermal resistance by diameter for different fluids given the
same parameters
(L = 2 m, Q = 200 W, T = -80 °C, vapor quality range 0-35%)

Source: Contiero, Barroca et al. (2022)

Krypton stands out among the refrigerants for the given requirements. Ethylene, Ethane, N2O, and Xenon have lower reduced pressure and consequently larger temperature drops for this temperature range. They would have a much smaller capacity to remove heat due to the large pipe diameter. Krypton seems to be the refrigerant to move on with, it can allow high pressure drops which leads to higher velocities and higher heat transfer coefficients, Contiero, Barroca et al. (2022).

2.5 Krypton cycle

Developing a hybrid cooling cycle using Krypton is in process at NTNU in Trondheim and at CERN. It is the cycle that is designed by Luca Contiero that this thesis will focus on.

The system has the same requirements as the 2PACL cycle describes earlier. There the heat is rejected to a CO_2 chiller. In the hybrid Krypton cycle, the two-phase pumped loop is replaced with a hybrid refrigeration cycle but still requires a CO_2 chiller to reject heat, Contiero, Barroca et al. (2022).
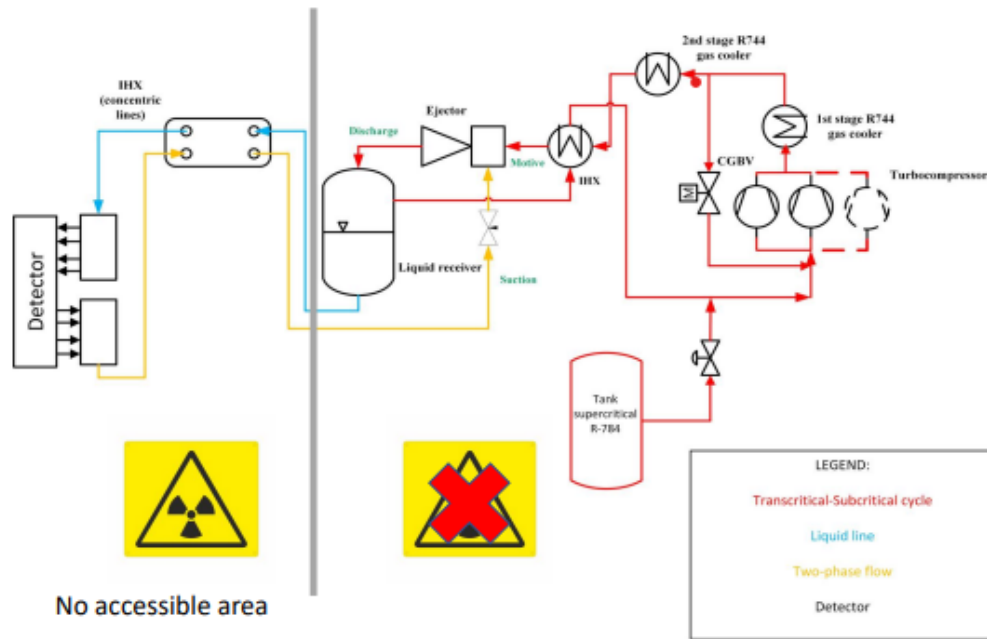
Figure 14: P&ID for a Krypton cycle

Source: Contiero, Hafner et al. (2022)

Figure 14 shows the hybrid Krypton cycle, with a passive loop and a primary cycle. Starting from the injection of pressurized krypton into the compressor, the refrigerant moves through parallel turbo compressors to the first gas cooler. The compressors work at a constant pressure ratio to avoid the surge envelope, providing a stable volumetric flow rate with good efficiency and a constant rotational speed. After the first gas cooler, a cold gas bypass valve is placed control the amount of refrigerant sent to the detectors. The first gas cooler is there to reduce the temperature of the fluid to avoid large amounts of mixing at the suction of the turbo compressors. Then there is a second gas cooler. This second gas cooler ensures necessary heat rejection to the CO_2-loop an the right temperature into the ejector. After the gas coolers, there is an internal heat exchanger as a subcooler before the ejector. This becomes the motive of the ejector. The suction stream into the ejector is mixed with the motive stream in the mixing chamber is the output of the concentric line internal heat exchanger in the passive loop. The outlet of the ejector is connected to a separator where the gas is returned to the subcooler. The liquid from the separator is the input of an internal heat exchanger with concentric lines. This cools the detectors, and the output from the detectors is sent back to the internal heat exchanger in the passive loop. The final output from this heat exchanger is sent back as the suction in the ejector, Contiero, Hafner et al. (2022).

The internal heat exchanger is made of concentric lines because there are long transfer lines between the primary cycle and the passive loop in the experimental cavern. A concentric line in the heat exchanger avoids double insulation for this long pipe; this is the same as in the 2PACL system, Contiero, Hafner et al. (2022).

2.5.1 Start-up

When Krypton is at room temperature in the experimental cavern, it is above the critical point. The room temperature of about 20°C is shown in figure 15. If the system were to begin from this gas state, the detectors would be exposed to thermal shock. As previously described, this is to be avoided. It has become a common practice to use a cooldown of about 1 Kelvin per minute, Contiero, Barroca et al. (2022).
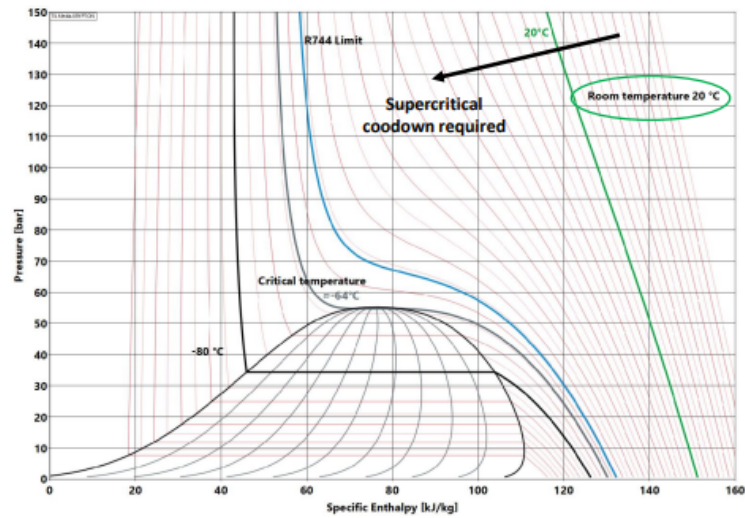
Figure 15: Log PH diagram for a Krypton cycle, showing the supercritical point

Source: Contiero, Hafner et al. (2022)

To change the starting point, the supercritical tank can be used to change the charge. The increased pressure would lead to new starting pressure levels. The injection can stop when desired levels are reached and the compression starts. This charging process has to consider the heat rejected through the gas coolers and the consequential loss of pressure.

The concentric line as insulation is a safety feature against overcooling, as it is with the start-up of the 2PACL system.

2.5.2 Supercritical operation

Suppose the system has to operate in the supercritical region. In that case, this would be a part of the start-up processes where it both cools and charges, as seen in figure 16. This could be necessary when the operating envelope hits the cooling limit of CO_2. This is because the subcritical conditions get closer to the limit of vapor quality acceptable before dry-out in the detector. This would result in a two-phase flow in the return line that the compressors can not handle. The other reason is that there would be a need for a different natural refrigerant in the gas cooler with a lower freezing point. The high pressure avoid overcooling of the detectors, Contiero, Hafner et al. (2022).
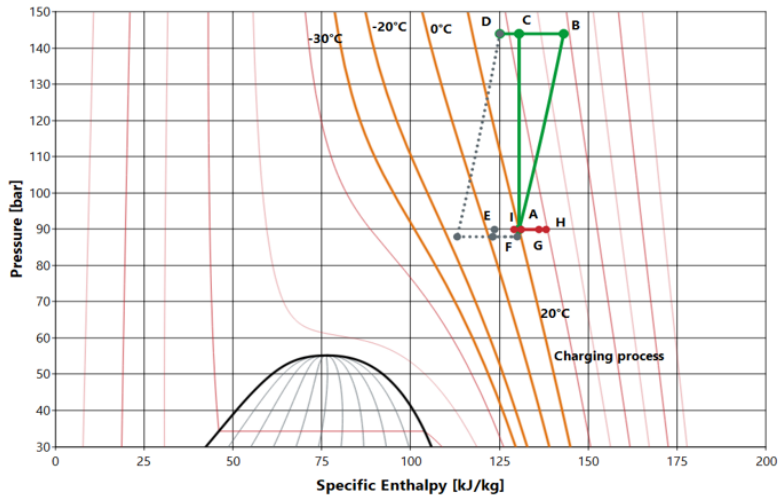
Figure 16: Log PH diagram for a Krypton cycle, showing the
supercritical operation

Source: Contiero, Hafner et al. (2022)

2.5.3 Transcritical-subcritical operation

The system can also operate in the transcritical-subcritical region after a supercritical cooldown using charging. The supercritical mode is used until the detectors' temperature is above the critical temperature of Krypton. The ejector mixes the outlet of the concentric line with the output of the internal heat exchanger and lowers the pressure, ensuring that it ends up in the two-phase region. The liquid receiver sends the liquid to the concentric line, which subcooles the liquid. Then the capillaries decrease the pressure isenthalpic to the saturation line. The detectors reject heat, and the liquid is back to the two-phase region and back to the suction of the ejector. This process is shown in figure 17, Contiero, Hafner et al. (2022).
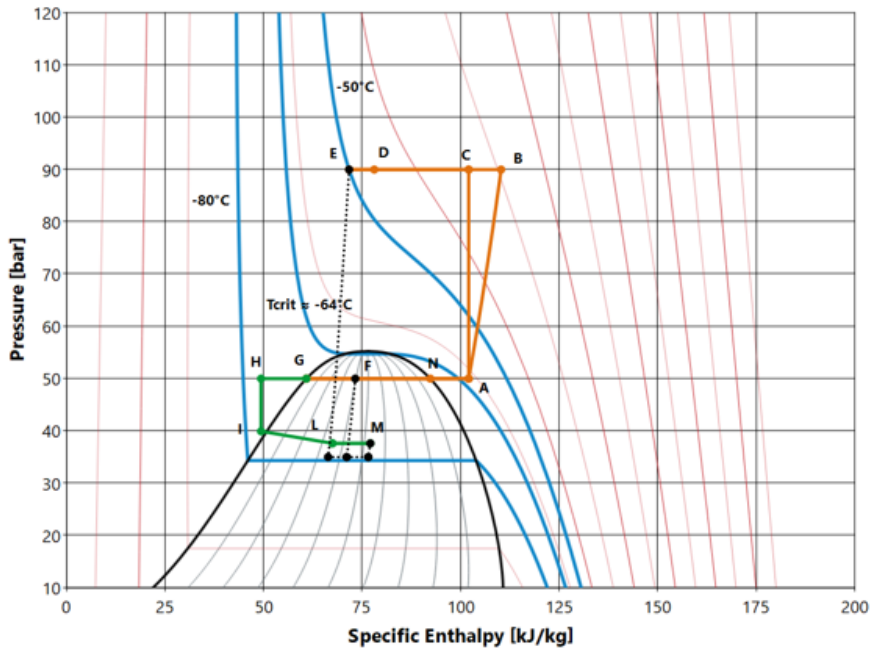
Figure 17: Log PH diagram for a Krypton cycle, showing the
transcritical cycle

Source: Contiero, Hafner et al. (2022)

15

2.6 Ejector

Since there can not be any active hardware, like valves in the passive loop, the flow in the capillary is determined by the ejector design. The benefit of the ejector is that it can control the properties going into the passive loop and therefore allow the passive loop to be operated at a significant distance from the compressor. This is similar to how the 2PACL system is used today. The low-pressure part will be located in the collider and cannot be maintained as long as the collider is running.
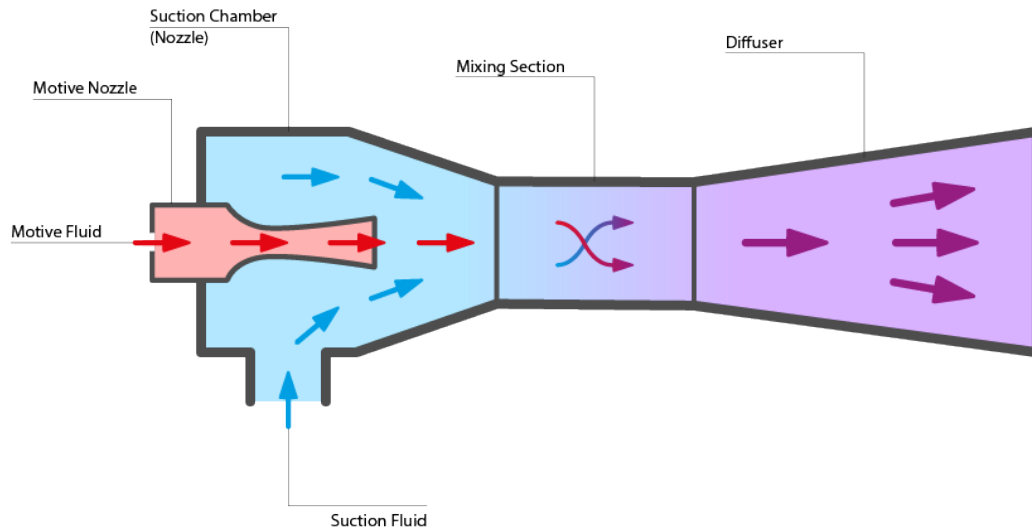
Figure 18: Main components and fluid flows through ejector

An ejector chances the performance of an ejector by fluid entertainment, with one fluid being swept along into an existing moving flow. The part of the ejector consists of a high-pressure stream into the motive nozzle, a lower-pressure stream into the suction nozzle, a mixing chamber, and a diffuser outlet where the outlet stream is a pressure between the high and low pressure. The outlet pressure depends on the motive nozzle, the suction nozzle, and how the mixing chamber and diffuser are designed. Figure 18shows the elements of an ejector. The effective nozzle flow area can be set to a design point or adjustable by a positing needle, S. Elbel and Lawrence (2016).

The driving nozzle, or the motive nozzle, is designed to accelerate the fluid to a high velocity and expand the motive fluid; by this maximizes the kinetic energy. The motive nozzle is part of controlling the entertainment ratio. As shown in figure 18, it is designed as a converging-diverging throat. It firstly restricts the fluid to the narrowest point and the highest velocity; after this, the nozzle has diverging throat that controls the expansion of the fluid, Y. Liu et al. (2021).

The suction nozzle is the other nozzle that controls the entertainment ratio; it proves a controlled entry of the suction fluid into the mixing section. The diameter is often larger than that of the motive nozzle to gradually expand the fluid, minimize flow losses, and maximize the efficiency of the fluid entry. The expansion of the fluid from the evaporator pressure increases the pressure and converts some of the pressure to kinetic energy. As shown in figure 18, the suction chamber converges into the mixing section to gradually accelerate the fluid velocity, Y. Liu et al. (2021).

In the mixing chamber, the low-pressure fluid from the suction nozzle combines with the high-pressure, high-velocity fluid from the motive nozzle. Since the motive nozzle fluid has a high momentum, it creates a suction and circulation effect, ensuring mixing in this chamber. This ensures fluid entertainment and energy transfer. The goal of the mixing chamber is to create a homogeneous fluid of the two entry fluids. The most important design factor of the mixing chamber is the length and, therefore, time spent in the chamber; the longer time, the bigger chance there is

for perfectly homogeneous fluid. Y. Liu et al. (2021)

The diffuser is designed with a diverging throat so that the fluid expands; it gradually converges the kinetic energy to pressure energy, resulting in a pressure recovery. To ensure this, the length and shape of the diffusion chamber have to be designed to gradually and uniformly expand the fluid. The design of the diffuser also has to ensure minimum flow separation, which results in losses.
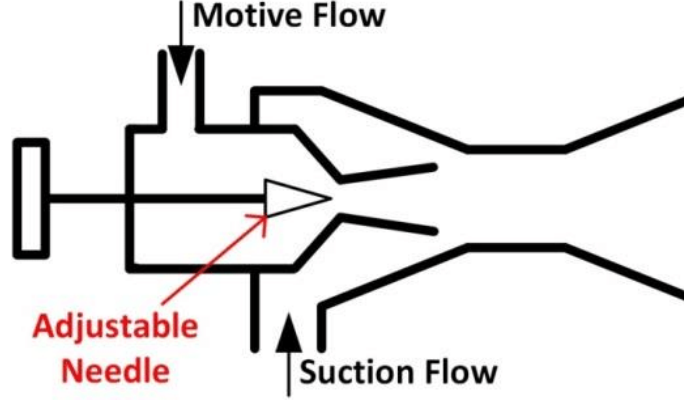
Figure 19: Adjustable needle position nozzle in an ejector

Source: Zhu and Stefan Elbel (2016)

An adjustable position motive nozzle is one way to control the ejector during operation. The previously described motive nozzle has a fixed motive nozzle, and therefore, the nozzle's design must be done before the ejector is manufactured. With an adjustable position nozzle, a needle in the middle of the throat can change position, thereby changing the flow area as shown in figure 19. This allows for more flexibility in the operation of the ejector as it changes the entertainment ratio and, thereby, the mixing effectiveness. This can be especially useful in operations with frequent changes in the evaporation load since it provides fine-tuning of the ejector system and can give a larger operating range. It is also useful in systems requiring controlled start-up or shut-down, as in the proposed hybrid cycle used at CERN. It allows close control of changes in fluid properties and working conditions.

The article "Investigation on performance of variable geometry ejectors for CO2 refrigeration cycles" shows that for set motive and suction efficiencies, the ejector pressure recovery reached a maximum as a function of the motive nozzle throat area and the diffuser discharge quality reaches a minimum as a function of the motive nozzle throat area, F. Liu et al. (2012).

Adjustable position nozzle ejectors are often used in the experimental analysis, and after experiments changed to a fixed position nozzle with the best efficiency. One of the main reasons for this is this is the increased complexity of the system. An adjustable position nozzle requires more components and control systems to optimize the use of the adjustable position. It also increases the chances for uncertainty in the system either by mispositioning of the needle or failure of the component. A fixed area nozzle with other control systems can provide adequate performance for many practical applications.

An important factor of the motive nozzle is that the outlet velocity is assumed to be sonic. To calculate the speed out of the motive nozzle, one needs to calculate the speed of sound in a two-phase fluid. This can be done by using the Brennen method for CO_2. This is the method that Modelica is using, Brennen (2009).

$$\frac{1}{\rho c^2} = \frac{\alpha k_V}{p} + \frac{(1-\alpha)k_L}{p^{1+\eta}} \tag{2}$$

where $k_v = (1 - \epsilon_V)f_V + \epsilon_V g_V$ and $k_L = \epsilon_L g * (p_c)^\eta$.

In this formula, ϵ_V and ϵ_L are fluid fractions, also called communicating fractions. They indicate how much of an exchange of mass there is. If they are both 0, it would be a homogeneous frozen model; if they were both 1, it would be a homogeneous equilibrium model. These factors are included since a limited amount of heat transfer occurs between each phase where they interface.

In this formula, f_V and f_L are thermodynamic properties; they are the partial isentropic derivation of the logarithmic density of the state given the logarithmic pressure.

In this formula, g_V and g_L are the vapor and liquid index, respectively. For CO_2 the g_L is approximately $g_L = 2.1(\frac{p}{p_c})^{0.566}$ The value for the vapor index is commonly set to 1 for CO_2. η is commonly set to 0.566. p_c is the critical pressure for CO_2 which is 73.77 bar.

f_v and g_v are in order of unity; therefore, the result is rather insensitive to ϵ_V. f_L is approximately 0, and g_L varies with pressure and has the biggest influence on the result. The resulting factors that are used is that $K_v = 1$ and $K_L = 2.1\alpha(p_{crit})^{0.566}$

α is the void fraction. The void fraction describes the fraction of liquid and gas in a two-phase flow; it is not the same as the vapor quality. Vapor quality is a measurement of how much of the total mass is vapor. The void fraction is based on volume. There are several methods of measuring the void fraction in a two-phase flow. Two of the most common methods, from Zivi (1964) and Smith (1969), are presented in equation 3 and 4.

$$\alpha = \frac{1}{1 + (\frac{1-x}{x})(\frac{\rho_g}{\rho_l})^{2/3}} \tag{3}$$

$$\alpha = \frac{x}{x + (1-x)(\frac{\rho_g}{\rho_l})(\frac{v_g}{v_l})} \tag{4}$$

Both of these use the vapor quality, x, the densities for gas, ρ_g, and liquid, ρ_l, and v_g and v_l are the mean velocities of the gas and liquid phase.

Pietrzak and Płaczek (2019) has made a correlations of void fraction in small channels for homogeneous flow and using the slip ratio S. This is shown in equation 5

$$\alpha = \frac{1}{(1 + S(\frac{\rho_g}{\rho_l})(\frac{1-x}{x})} \tag{5}$$

The slip ratio can be calculated by the CHISHOLM (1985) correlation. For a homogeneous flow S = 1, as there is no slip.

$$S = \sqrt{1 - x(1 - (\frac{\rho_l}{\rho_g}))} \tag{6}$$

Kong and Qi (2018) made a comparison of different methods of calculating void fraction compared to different vapor fractions and looked at different speeds of sound. The result was that the model chosen is highly dependent on the working fluid and operation conditions. A change of correlation could therefore improve the accuracy of the ejector modeling.

The first description of an ejector efficiency was introduced in 2007 by Köhler et al. (2007). It is not based on the design parameters of the ejector but on the parameters of the fluids in the ejector. Later there have been made improvements on the correlation of the ejector efficiency, but this method is used in this thesis, F. Liu (2014).

$$\eta_{ejector} = \frac{m_s(h'_{s,isen} - h_s)}{m_d(h_d - h'_{d,isen})} \tag{7}$$

The subscript s is the suction inlet, and d is the driver inlet. The enthalpy h_d is h_C in the model as the entry into the driving nozzle into the ejector, and $h_{d,isen}$ is calculated by the entropy at point C and the pressure in the ejector. In the same way, h_s and $h_{s,isen}$ are the enthalpies at the suction nozzle and are h_I.
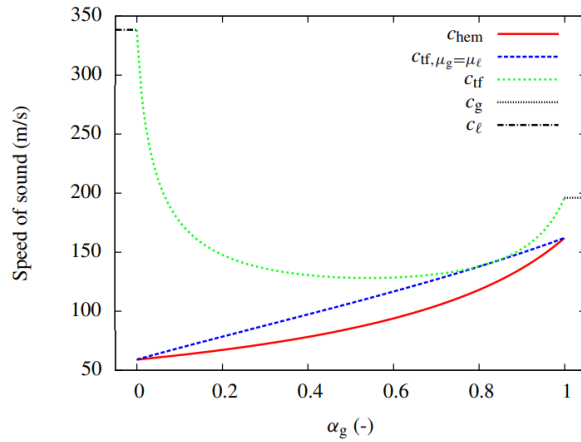
Figure 20: Adjustable needle position nozzle in an ejector

Figure 20 shows the relation between the speed of sound and void fraction. This model is made for a temperature of 250K. The figure shows c_g as the speed at the gaseous phase and c_l as the speed at the liquid phase. c_{hem} is the homogeneous equilibrium model, c_{tf} is the two-fluid model with no phase change and no slip, and $\mu_g = \mu_l$ is the two-fluid model with full chemical equilibrium and no slip, Aursand et al. (2013).

3   Method

The method chapter covers the various methods used in this master thesis. Firstly, the chapter describes the components in the test facility and how it corresponds to the simplified hybrid cycles using CO_2. The simplified cycle is used in two types of simulations, one using Modelica and one using Matlab. The chapter presents how the mathematical background for these simulations. The last part of the chapter is the method behind the uncertainty analysis.

3.1   Description of the test facility

Figure 21 shows the P & ID for the Xenon setup. It is similar to the P&ID of the Krypton cycle shown in figure 14. This part of the method chapter shows how the sensors are placed in the hybrid heat pump cycle and what the components are. For the setup of the Xenon test rig, some of the components are based on CO_2 components because they are designed for high pressure.
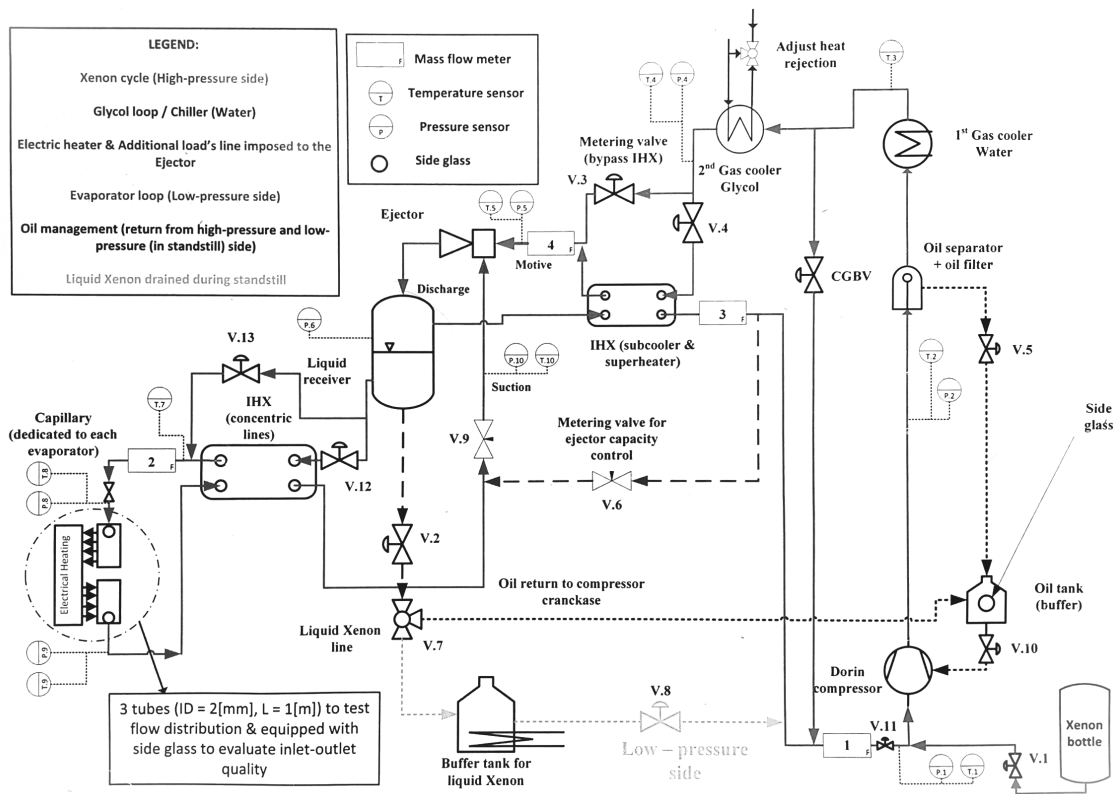
Figure 21: P&ID for a Xenon cycle showing the sensor points
(Illustration made by Luca Contiero 2022)

The compressor will be a Dorin compressor model CD180H, often used for transcritical CO_2 operations. There is a Xenon bottle connected to the compressor to charge the cycle. After the compressors, there is an oil separator with sight glass and oil filter. It is connected to a buffer tank for oil. After this, there are two gas coolers, one with water and one with glycerin. Both of these will be brazed plate heat exchangers. Between the two gas coolers, a cold gas bypass valve is used to lead refrigerant back to the compressor due to the excessive compressor capacity compared to the evaporator heat load.

Out of the last gas cooler, the fluid goes into a loop with an internal heat exchanger and metering valves. The internal heat exchanger has subcooling on the high-pressure side and superheated vapor at the compressor suction. The outlet of the internal heat exchanger goes into the motive of the ejector. The ejector is an ejector for CO_2 with a fixed geometry in the test facility. This marks the start of the passive loop with the liquid receiver. The liquid receiver uses sight glasses and has four flow lines, a gas line to the compressor and a liquid line to the passive loop. The third line is the two-phase from the ejector. The last line is for the oil recovery. The liquid out of the separator goes into another internal heat exchanger. The plan was to use concentric tubes for the heat exchanger to the passive loop, but this might not be feasible due to the length. Instead, a brazed plate heat exchanger will be used. In the passive loop, there is a set of capillaries before the evaporator to adjust the pressure, then evaporator tubes for the electric heating; this represents the heat from the sensors.

Some of the components are changed in the simplified model presented more precisely in the Modelica model. There are no bugger tanks or oil recovery. The two gas coolers are combined, and the internal heat exchanger between the gas cooler and the ejector is removed.

There will also be several sensors in the test rig to evaluate the results and the numerical calculations. Mass flow rate will be measured at four points:
M1 is at the suction for the compressor.
M2 is the liquid flow going through the evaporator.

M3 is the vapor from the liquid receiver.
M4 is the motive flow rate into the ejector.

There will also be 10 point of measuring the pressure and or temperature
$(P, T)_1$ is at the inlet of the compressor.
$(P, T)_2$ is the outlet of the compressor
$(T)_3$ is the outlet of the gas cooler with water
$(P, T)_4$ is at the outlet of the gas cooler with water and glycerin
$(P, T)_5$ is at the motive nozzle port in the ejector
$(P)_6$ is the pressure of the liquid receiver
$(T)_7$ is the temperature out of the concentric line that is the internal heat exchanger in the passive loop.
$(P, T)_8$ before the evaporator.
$(P, T)_9$ after the evaporator.
$(P, T)_1 0$ at the suction nozzle port for the ejector.

For the simplified model, $(P, T)_2$ and $(T)_3$ has been combined into one sensor. All the other sensor point will be evaluated.

3.2   Simplification of Xenon cycle using Modelica

Modelica is an object-oriented modeling language for component-oriented modeling of complex systems, e.g., systems containing mechanical, electrical, electronic, hydraulic, thermal, control, electric power, or process-oriented components. The non-profit Modelica Association develops the free Modelica language, The Modelica Association (2022).

The simulation made for this thesis is a two-phase refrigeration system to cool the specified input heating. It is a simplification of the Krypton cycle shown in figure 14. It uses Modelica and CO_2 as a refrigerant since it has similar pressure properties to Krypton and Xenon. This model aims to learn about the ejector system and how different sensors may affect the result. This model is only for the transcritical cycle, not the supercritical cooldown.

The following assumptions are done for the model:

- One dimensional steady flow for the working fluid in the system

- The pressure drop is assumed to be zero in the heat exchangers and the pipe

- Expansion and compression processes are assumed to be adiabatic

3.2.1 Transcritical Cycle
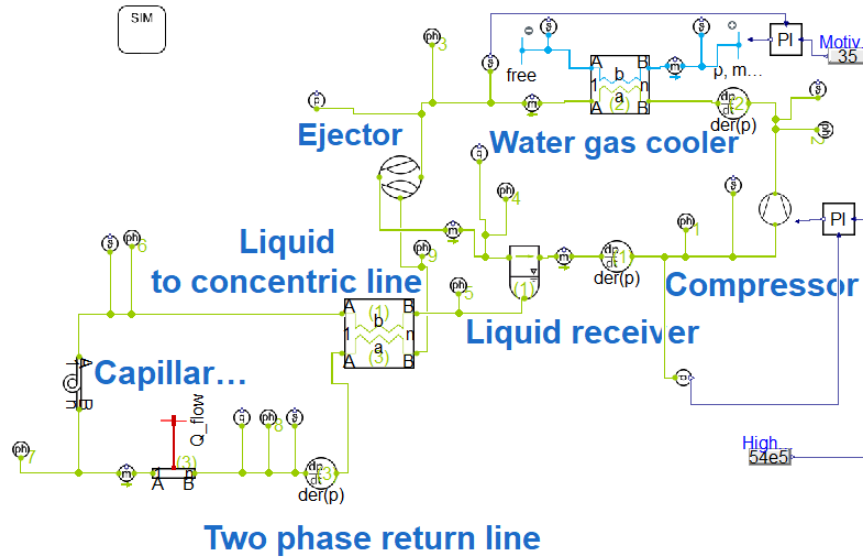
Figure 22: Modelica model of transcritical CO$_2$ cycle
(Illustration made by Jerve 2022)

Figure 22 shows the model made in Modelica. The Modelica model has three pressure states at 90 bar, 54 bar, and 50.58 bar. These pressure states are used in Modelica whenever a VLEfluid with a volume is used. This is because Modelcia uses steady-state models. This means that the assumption is that the time derivative of pressure dp/dt is constant along the direction of flow for each pressure level in the system. Each pressure ID uses the same derivative of pressure with respect to time. Pressure ID gives an initial pressure for the location.

Compressor

The compressor is a compressor based on efficiency with a mechanical port. The mechanical port controls the rotational speed n with a PI-regulator based on the pressure. The measurement for the PI-regulator is the pressure into the compressor. The real expression set as the set point is 54 bar. The pressure will go up if there is high vapor content in the receiver, more vapor should be removed to maintain the pressure level, and therefore the rotational speed goes up. The PI-regulator regulates the with a proportional gain of k = 1e2 and a time constant Ti = 1s. The initial value is 1, with a max limit of 40 and a minimum limit of 0.00001. The PI-regualtor ensures the pressure in the compressor, but not more than the compressor is designed for. Volumetric, isentropic, and effective isentropic efficiency is set to 70%.

Gas cooler

The gas cooler in this simple model combines the Krypton model's first and second gas coolers. This gas cooler covers the heat loss to the input of the ejector. No cold gas bypass valve is included in this model because the operation is simplified. For the gas cooler, an internal heat exchanger is used. It is a plate heat exchanger with parallel flow with water as the cooling medium. The water side is set by an underdetermined boundary on the entry side and an overdetermined boundary on the output side. A PI-regulator sets the temperature of the output. The measurement into the PI-regulator is the temperature that goes in the motive of the ejector. The set point is at 35 °C. It regulates the mass flow with an initial value of 0.028 m/s, a max limit of 1 m/s, and a minimum value of 0.0000001 m/s. The setting parameters are given as k = 1e-4 and Ti = 2s.

Ejector

The ejector is an effective ejector with a constant driving flow area of 2e-7m^2. The efficiency is set to 20%. The ejector mixes the output from the gas cooler as the motive and the output from

the internal heat exchanger connected to the passive loop as the suction stream. The output of the ejector is a two-phase high-pressure fluid that is the input of the separator. The input in the motive is high pressure, and the input in the suction stream is lower pressure. The result after the mixing is a medium pressure, based on how much of the streams can go through the effective area. For the Modelica model, the flow area is set, but in the actual model, it would be possible to change the flow area of the motive and the suction stream.

Separator

The separator is the liquid receiver, it receives two-phase fluid from the ejector's output, separating the gas from the liquid at a constant pressure. The gas goes back to the compressor, and the liquid goes to the internal heat exchanger.

3.2.2   Passive loop

The passive loop represents the part of the system that cools down the detectors. The premise for this cooling system is the heat load from the detectors. Figure 23 show a Modelica model of the passive loop of the transcritical CO_2 cycle.
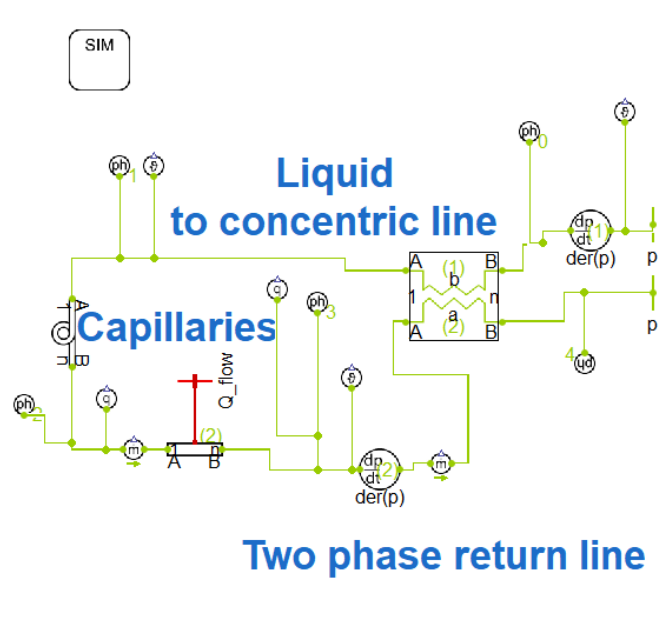
Figure 23: Modelica model of the passive loop of the transcritical CO_2 cycle
(Illustration made by Jerve 2022)

Internal heat exchanger

The internal heat exchanger is a tube-in-tube heat exchanger to avoid double insulation in the real system. These are the lines connecting the experimental cave to the surface.

Capillaries

The capillaries are used here as an expansion valve. It is a long tube with a small diameter, and the pressure losses inside the tube cause the expansion. The current diameter is set to 1.5 mm, and the tube length is 0.11172 m. The roughness determines the pressure loss inside the tube and is set to 1e-04 m. More subcooling at the inlet results in less pressure loss. Moreover, less pressure loss leads to less subcooling in the refrigeration cycle.

Heater

A dummy load is used to simulate the heat that needs to be removed from the detectors. It is

a tube with a multi-port heat boundary with a fixed heat flow of 1000 W. This will work as the evaporator for the system.

3.3   Numerical calculations of the ejector using Matlab

A mathematical model of the Modelica system has been made to look at the effects of changing variables. Figure 24 shows a structure of the model, including the mass flow rates that are the base for the calculations. Out of the compressor comes $\dot{m}_{dot}$, which will be regulated until it is the same as $\dot{m}_{gas}$, which comes out of the gas cooler. In the motive nozzle of the ejector, the new mass flow rate, $\dot{m}_c$, is calculated using the speed of sound. This is regulated until it is equal to the two previous mass flow rates by changing the vapor quality. The vapor quality sets the liquid mass flow rate $\dot{m}_{liq}$. The two mass flow rates are added in the ejector to create $\dot{m}_{feed}$ into the separator, which again is separated into the two phases. The figure also shows how the components are connected. The red boxes are the components that are high-pressure and in the gas phase. The green figures are low pressure and liquid and two-phase; this is the passive loop, as previously described. The yellow figures are at medium pressure in the two-phase region and connect the two loops.
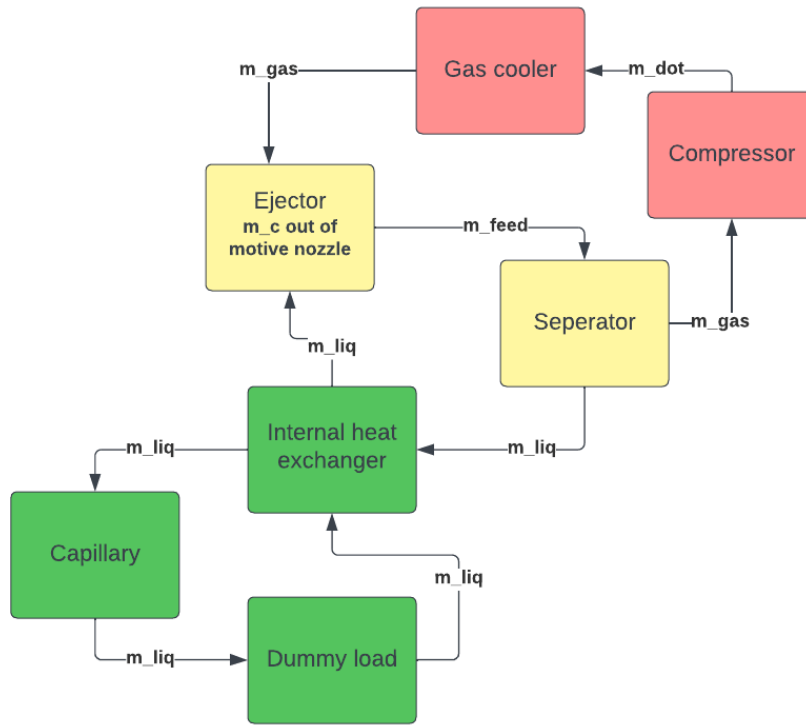
Figure 24: Matlab structure for ejector cycle
(Illustration made by Jerve 2023)

The calculations are based on the description of how Modelica calculates the components. Most calculation methods are gathered from the "info" section for each component; this documentation is also referenced in the figures. To further calculate the points, the REFPROP addition to Matlab is used. REFPROP is an acronym for REFerence fluid PROPerties. This program, developed by the National Institute of Standards and Technology (NIST), calculates fluids' thermodynamic and transport properties and their mixtures. National Institute of Standards and Technology (2022) The addition uses a library to calculate thermodynamic properties based on two set properties and given the substance.

$$result = refpropm(prop_req, spec1, value1, spec2, value2, substance1)$$

The set requirements for the system are the same as for the Modelica model: 35 °C at the point after the gas cooler comes into the ejector The heat from the dummy load is set; this represents the heat load from the sensors. Q_{evap}= 1kW.

3.3.1 Compressor

The first point is suction into the compressor. This point is set by the medium pressure at 54 bar and vapor quality of 100 %.

For the calculations of the compressor, the following parameters are set by the Modelica model:
Speed: $n = 50$ Hertz
Volumetric displacement $= 0.0000031$ m^3
Isentropic enthalpy of discharge $= h_{isen}$
Enthalpy of discharge $= h_{dis}$
Enthalpy of suction $= h_{suc}$

The volumetric efficiency is calculated and set as:

$$\lambda_{eff} = \frac{\dot{m}}{\dot{V} n \rho} = 0.7 \tag{8}$$

The isentropic efficiency is calculated and set as:

$$\eta_{isen} = \frac{h_{isen} - h_{suc}}{h_{dis} - h_{suc}} = 0.7 \tag{9}$$
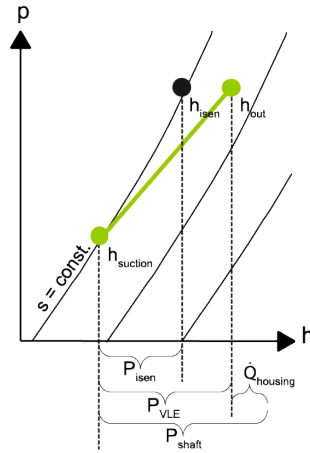
Figure 25: Illustration of isentropic efficiency of a compressor

Source: TLK-THermo GmbH (2023a)

The effective isentropic efficiency is calculated and set as:

$$\eta_{effisen} = \frac{\dot{m}(h_{isen} - h_{suc})}{P_{shaft}} = 0.7 \tag{10}$$

The Modelica simulation shows in figure 26 that P_{shaft} is almost equal to P_{VLE} and that $Q_{housing}$ is marginally small. This means that the effective isentropic efficiency is the same as the isentropic efficiency.
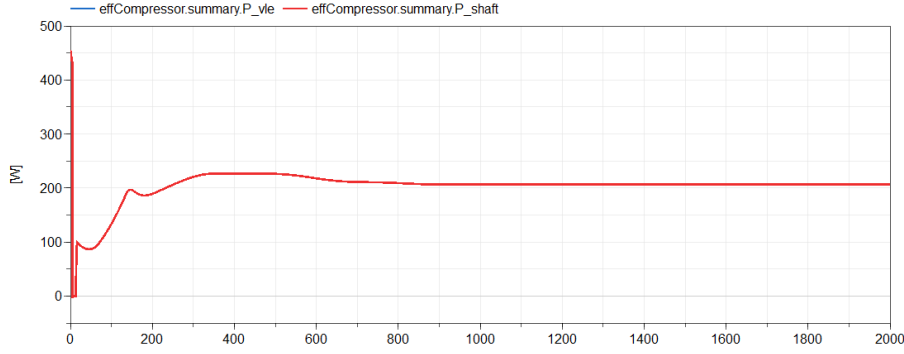
Figure 26: Results of P_{shaft} and P_{VLE} from Modelica

To calculate h_{isen}, the entropy of point A first has to be calculated. h_{isen} is then calculated with the third pressure ID and using the same entropy as point A.

The density ρ is calculated using refprop with the pressure of point A and vapor quality of 100% since point A is at the vapor line as the input in the compressor.

A positive displacement compressor can usually be calculated by the ideal gas law using from $PV^n = constant$ and $PV = mRT$

$$\frac{p_2}{p_1} = (\frac{V_1}{V_2})^n \tag{11}$$

Where n is equal to k in an isentropic process, and k is the ratio of specific heats C_p/C_v. This process is beyond the critical pressure for CO_2, which is $p_{crit} = 73.77bar$. Therefore there are relations between the change in mass flow rate and pressure, but it is specific for each compressor. To estimate the pressure relationship for this compressor, the simulation was run in Modelica for 2000 seconds until stabilization. Then the inlet pressure, outlet pressure, and mass flow rate were exported to Microsoft Excel. There is a relation between pressure ratio p_2/p_1 and mass flow rate for each measuring point created. The resulting line is the surge line for this specific compressor. Below are the first results presented in a scatter plot in figure 27.
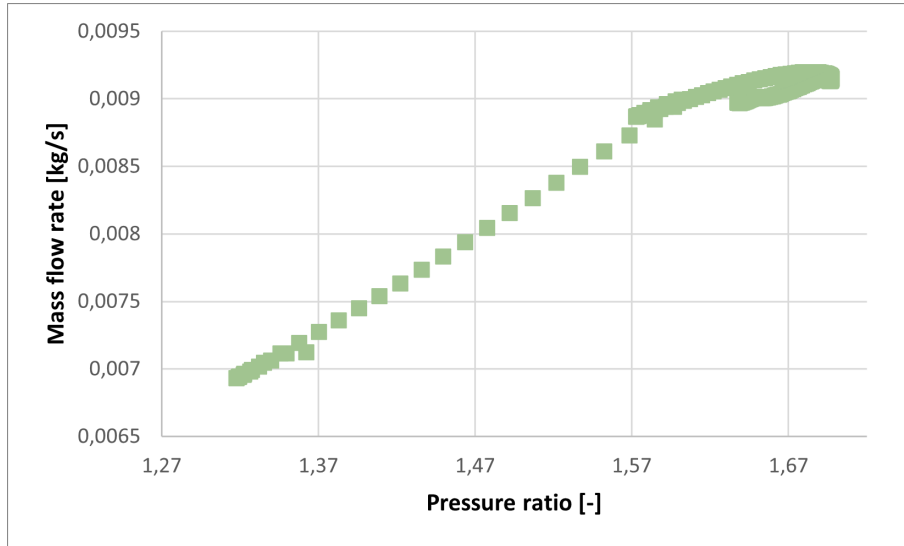
Figure 27: Experimental results of relation between pressure ratio and
mass flow rate in compressor
(Illustration made by Jerve 2023)

As figure 27 shows, most results are located at a pressure ratio higher than 1,57 and a mass flow rate of around 0,009 m/s. They are more likely to represent the actual surge line for the compressor.

To create a linearization, the first 400 seconds, and the first 100 measuring points, are excluded in the second figure, where there is a clear relationship between pressure ratio and mass flow rate, as presented in figure 28.
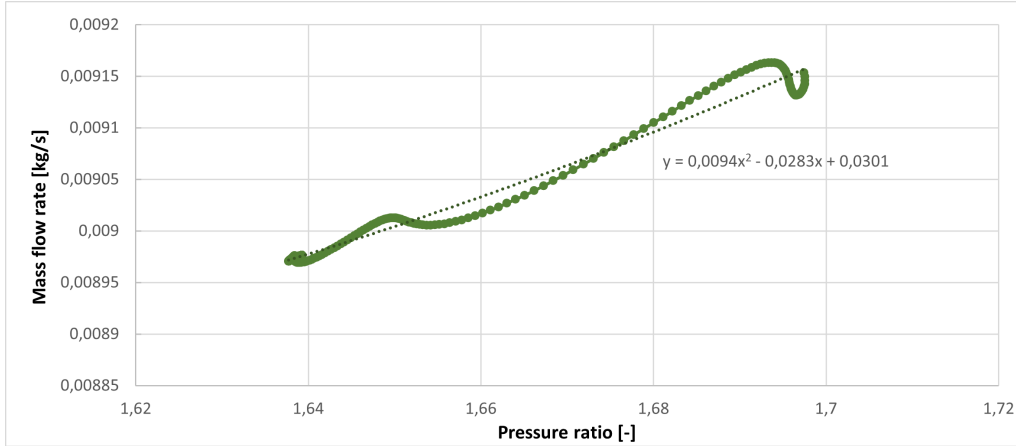
Figure 28: Relation between Pressure ratio and mass flow rate in more
defined area and trend line
(Illustration made by Jerve 2023)

Using Excel for this scatter chart, a trend line has been inserted. It is a second-degree polynomial, and the resulting relationship is given below.

$$Y = 0.0094x^2 - 0.00283x + 0.0301 \tag{12}$$

Y is the mass flow rate, and X is the pressure ratio. Surge lines are normally second-degree polynomials, although this model is for such a small increment that the trend line resembles a linear relation.

Modelica uses a PI regulator to regulate the volumetric displacement until the mass flow rate of the compressor is the same as the mass flow rate out of the gas cooler. Therefore there is an additional variable in the calculation as the relative displacement is multiplied by the volumetric displacement. Since the trend line is a second-degree polynomial to be solved for the pressure ratio, the solution can not contain complex numbers from the square root. Therefore the starting value for the mass flow rate is 0.00879973404, and the starting value for the relative displacement is 0.461.

3.3.2 Gas cooler with water

The transferred heat must be calculated first to calculate the mass flow rate out of the gas cooler on the refrigerant side. The liquid side of the gas cooler is calculated using VDI-plate calculations as described in the TIL documentation; these calculations are based on the VDI heat atlas, Chemieingenieurwesen (GVC) Editor (2010). It uses the Nusselt number to calculate the heat transfer coefficient.

$$Nu = \frac{\alpha d_h}{\lambda} \tag{13}$$

where α is the heat transfer coefficient, Nu is the Nusselt number, d_h is the hydraulic diameter and λ_w is the heat conductivity of steel. This is set to 45 W/(Km).

$$d_h = \frac{4\hat{a}}{\Phi} \tag{14}$$

The hydraulic diameter is calculated using equation14 where $\hat{a}$ is the amplitude of the sinusoidal corrugation pattern and Φ is the ratio of the wavy plate surface. Based on the set parameter in Modelica these can be calculated as from the equations 15 and 16.

$$\Phi(X) = (1/6)(1 + \sqrt{1 + X^2} + 4\sqrt{1 + X^2/2} \tag{15}$$

$$X = 2\pi\hat{a}/\Lambda \tag{16}$$

The two subfigures in figure 29 shows the geometry of a VDI plate and how the measurements are set. The amplitude $\hat{a}$ is 2 mm, the wavelength is Λ is 12.6 mm, the wall thickness is s_w is 0.75 mm . Using these variables results in $X = 0.9973$, $\Phi = 1.218$ and hydraulic diameter of $d_h = 6.568$ mm. This is confirmed from the Modelica model.

(a) Outside of VDI Plate   (b) Inside of VDI Plate
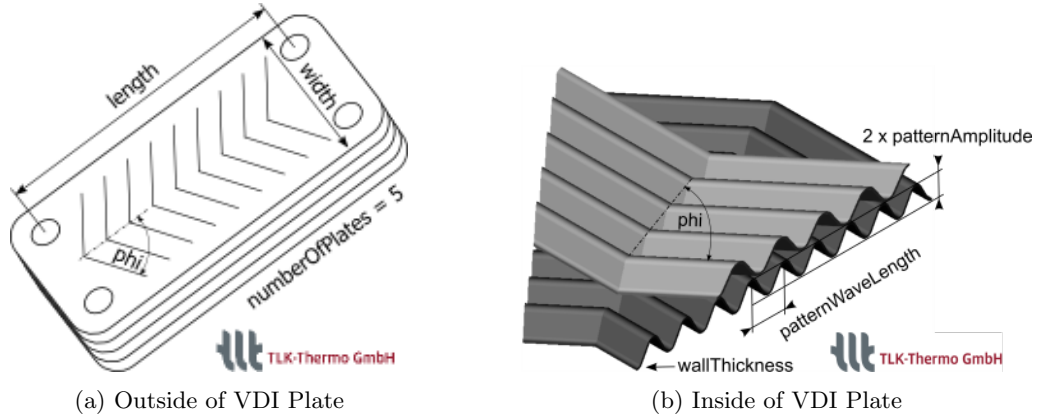
Figure 29: Plate geometry of a VDI plate heat exchange

To calculate the Nusselt number, equation 17 is used, where Pr is the Prandtl number, η is the dynamic viscosity, η_w is the bulk dynamic viscosity, and $\eta/\eta_w \approx 1$. The inclination angle $\phi = 35$ °.

$$Nu = 0.122Pr^{1/3}\frac{\eta}{\eta_w}[2Hg\sin(2\phi)]^{0.374} \tag{17}$$

The calculation of the Hagen number, Hg, is needed for the Nusselt number. This is given by equation 18

$$\xi Re^2 = 2\frac{\rho\delta pd_h^3}{\eta^2 L_p} = 2Hg \tag{18}$$

Re is the Reynolds number, and ξ is the friction number. The Hagen number is proportional to the pressure gradient $\frac{\delta p}{L_p}$ and set to 0.1 bar/m. The physical properties density and Prandtl number are calculated using refprop with water pressure 3 bar and inlet water temperature 15 °C.

To calculate the overall heat transfer coefficient, the conductivity through the wall is also included as in equation 19

$$\frac{1}{U} = \frac{2}{\alpha} + \frac{s_w}{\lambda_w} \tag{19}$$

Further the area of heat transfer, the reference area A_p is calculated by the plane surface A_0 and the factor to include the enlarged surface inside the gaskets.

$$A_p = \Phi A_0 = \Phi L_p B_p \tag{20}$$

where L_p is the length of 0.3m and B_p the width of 0.1 m Next the logarithmic mean temperature difference (LMTD) is calculated by parallel flow.

$$LMTD = \frac{\Delta T_o - \Delta T_i}{log \frac{\Delta T_o}{\Delta T_i}} \tag{21}$$

$\Delta T_i = t_{pi} - t_{si}$
$\Delta T_o = t_{po} - t_{so}$
t_{pi} is the primary flow inlet temperature = 56 °C.
t_{po} is the primary flow outlet temperature = 35 °C.
t_{si} is the secondary flow inlet temperature = 51 °C.
t_{so} is the secondary flow outlet temperature = 15 °C.

This gives a heat flow transfer is calculated by this equation

$$Q = UA_pLMTD \tag{22}$$

One the refrigerant side the heat transfer is calculated as

$$Q = \dot{m}_{dot}h_B + \dot{m}_{gas}h_B \tag{23}$$

The Modelica model uses a PI-regulator in the gas cooler to regulate the temperature of the water inlet so that point C reaches the desired temperature of 35 degrees C. For the numerical calculations in this thesis, the gas cooler calculations are made in a separate script with the temperatures from Modelica, and the heat transfer is set at a set value in the heat cycle script. This is done to simplify the script.

3.3.3 Ejector

As described in the theory section, the ejector has two input streams of different pressure: high and low. The output is a pressure between the two. The input in the motive is the output from the gas cooler. The input in the suction comes from the passive loop from the internal heat exchanger. There are some specifications from the Modelica model:
Efficiency of the ejector: $\eta_{ejector} = 0.2$
Flow area, A = 2e-07 m^2
First, calculate the mass entertainment ratio:

$$\mu = \frac{\dot{m}_I}{\dot{m}_C} \tag{24}$$

$$x_D = \frac{1}{1+\mu} = \frac{\dot{m}_{vapour}}{\dot{m}_{feed}} = \frac{\dot{m}_{vapour}}{\dot{m}_{liquid} + \dot{m}_{vapour}} \tag{25}$$

To calculate the mass flow rate in the throat it is based on the velocity,

$$u_{throat} = \sqrt{2(h_d - h_{throat})} \tag{26}$$

$$\dot{m} = A_{throat}\rho_{throat}u_{throat} \tag{27}$$

A_{throat} is set as the flow area. ρ_{throat} is calculated by the pressure in the ejector and the entropy at the driving nozzle.

The flow within the motive nozzle is assumed to be at sonic speed and therefore the Mach number is 1

$$Ma = \frac{u_{throat}}{c} = 1 \tag{28}$$

To calculate the Brennen method, as described in the theory chapter is uses, Brennen (2009).

$$\frac{1}{\rho c^2} = \frac{\alpha k_V}{p} + \frac{(1-\alpha)k_L}{p^{1+\eta}}$$

And to calculate the the void fraction the Pietrzak and Płaczek (2019) was chosen with the slip ratio calculated from equation 6

$$\alpha = \frac{1}{(1 + S(\frac{\rho_g}{\rho_l})(\frac{1-x}{x}))}$$

The ejector efficiency is calculated by this correlation.

$$\eta_{ejector} = \frac{\dot{m}_s(h'_{s,isen} - h_s)}{\dot{m}_d(h_d - h'_{d,isen})}$$

The subscript s is the suction inlet, and d is the driver inlet. The enthalpy h_d is h_C in the model as the entry into the driving nozzle into the ejector, and $h_{d,isen}$ is calculated by the entropy at point C and the pressure in the ejector. In the same way, h_s and $h_{s,isen}$ are the enthalpies at the suction nozzle and are h_I. In this model, the efficiency is not set as a requirement for the simulation. This is done to look at the changes in ejector efficiency when the mass flow rates are changed through the flow area.

3.3.4 Separator

The separator is a vertical separator, separating vapor and liquid. It assumes perfect phase separation that happens between 10% and 90 % filling level as shown in 30. The initial filling level in Modelica is set as 0.5 and a volume of 2 liters.
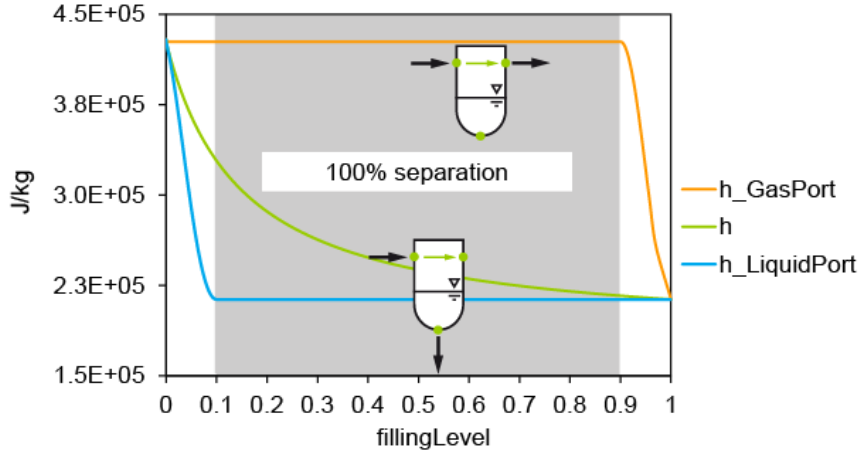
Figure 30: The ideal separation characteristic

Source: TLK-THermo GmbH (2023c)

The calculation for the filling level is given in equation 29 gathered from Modelica. TLK-THermo GmbH (2023c)

$$filling level = \frac{V_{liq}}{V} = \frac{\rho}{\rho_{liq}} \frac{h_{vap} - h}{h_{vap} - h_{liq}} \tag{29}$$

The enthalpy at the outlet of the gaseous and the liquid flow is are calculated on the set pressure in the separator and a vapour quality of 0 % for the liquid and 100 % for the vapor.

3.3.5 Passive loop

The passive loop, as defined from the liquid outlet of the separator to the suction inlet in the ejector from point E to point I, is calculated as a whole. The known factor of the passive loop is that the mass flow rate, $\dot{m}_{liq}$ is the same for the whole loop. For the internal heat exchanger, this means that the heat transferred, and therefore the enthalpy change between point E and point F is the same as between point H and point I. It is also known that point E and point G is both at the saturation liquid line. Further, the heat transferred between point G and point H is known as the dummy load sets. Lastly, the enthalpy at points F and G is the same but at different pressures.

To calculate this loop, the first point that needs to be calculated is the pressure difference between the set pressure for the separator at point D and the pressure after the capillary.

3.3.6 Capilliary

The capillary is based on pressure drop from friction inside the tubes. From the Modelica model some values are set
Length of pipe, L = 0.11172 m
Diameter of pipe, D = 0.0015 m
Roughness of the pipe, e = 0.0001 m
The Darcy-Weisbach equation defines the pressure loss for pressure drop in cylindrical pipes. This assumes a uniform diameter and full flowing in the pipes; for this application, this can be adopted.

$$\Delta p = f \frac{L}{D} \frac{\rho_F}{2} V^2 \tag{30}$$

Equation 30 uses the Darcy friction factor. Modelica calculates this using the Swamee-Jain equation since it is assumed to be a full-flowing fluid in circular pipes. This method is an approximation of the Colebrook-White equation.

$$f = \frac{0.25}{[log(\frac{e}{3.7D} + \frac{5.74}{Re^{0.9}}]^2} \tag{31}$$

The Reynolds number of the flow is calculated using the following formula. The volumetric flow rate is calculated from the mass flow rate, the area, and the density at the inlet. ν_F is the kinematic viscosity at the inlet, and D is the diameter of the pipe.

$$Re = V D \nu_F = \frac{\dot{m}_{liq}}{\rho_F A} D \nu_F \tag{32}$$

The inlet point F is partly unknown when this calculation is done; the pressure and liquid phase are known. To simplify the calculations, the density and kinematic viscosity is calculated using point E since this is known. Table 1 compares the thermodynamic proprieties of point F and point E, where the enthalpy and pressure are exported from the Modelica Model. It shows that the difference is about 2.5 %.

Unit		Point E	Point F	Differnce
kPa	Pressure	5400	5400	0,00 %
kJ/kg	Enthalpy	247,7	242,9	1,92 %
kg/m^2	Density	798,63	814,84	-2,03 %
cm^2/s	Kenmatic Viscosity	0,00088086	0,00089898	-2,06 %

Table 1: Table comparing thermodynamic properties of point E and point F

Out of the capillary, the pressure of point G is known. Since this point is also on the saturation liquid line, the enthalpy of point G can be calculated. This is the same enthalpy as point F. Therefore, that point is also determined.

3.3.7 Heater

Point G is the entry to the heater. The heater is set as a dummy load of Q_{load} = -1000 W = 1kW as it is in Modelica. This is used to calculate the exit enthalpy from after the heater, h_H.

$$Q_{load} = \dot{m}_{liq}(h_H - h_G) \tag{33}$$

3.3.8 Internal heat exchanger

The internal heat exchanger is calculated by first using the two known enthalpies of point E and point F.

$$Q_{EF} = \dot{m}_{liq}(h_E - h_F) \tag{34}$$

This is the same as the difference in point H and I. Point H was calculated out of the heater, and point I can be calculated.

$$Q_{EF} = Q_{HI} = m_{liq}(h_I - h_H) \tag{35}$$

3.3.9 System structure in Matlab

The calculations described in the previous chapters are calculated using the flow chart model shown in figure 31 in Matlab. The model is not cyclic as it calculates the values based on the starting point A without any changes to this point based on the output values from the separator. The model is based on calculating mass flow rates, which is essential when changing the flow area and stabilizing the system.
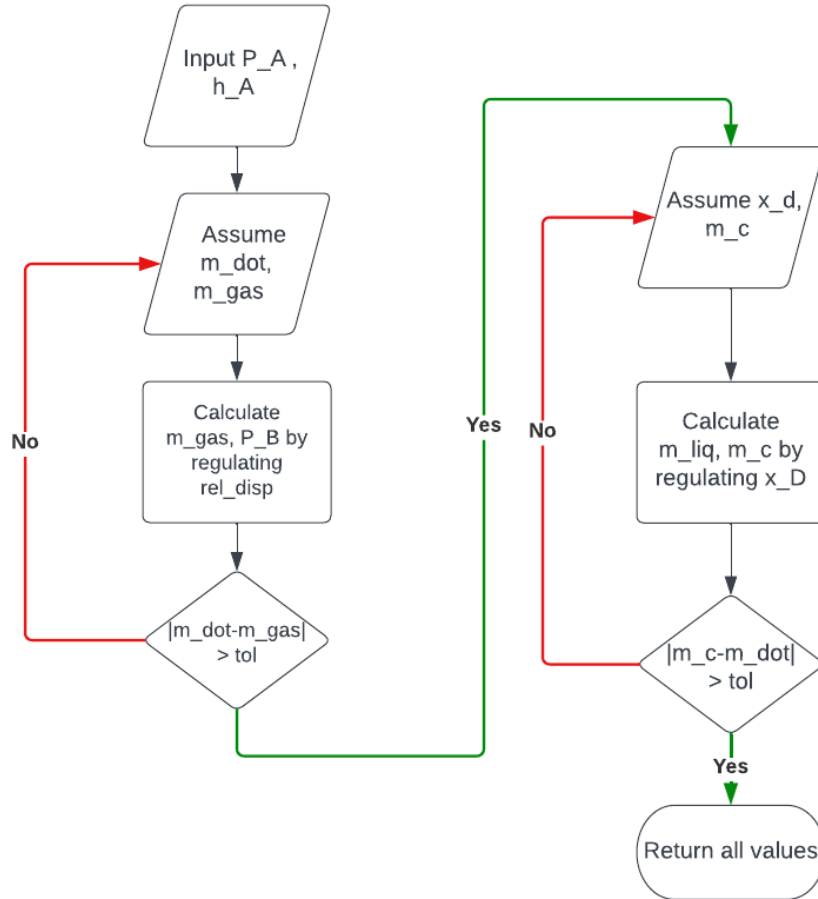
Figure 31: Flow chart for simulation of the ejector cycle
(Illustration made by Jerve 2023)

Firstly the input pressure and vapor quality in the compressor are set. The first mass flow rate, $\dot{m}_{dot}$, is calculated using these values and the set values from the compressor. This is then used in a while loop where the relative displacement is changed until the outlet mass flow rate out of the gas cooler, $\dot{m}_{gas}$, is within a tolerance limit of $\dot{m}_{dot}$. The tolerance limit that is used is 1e06. This while loop also calculates the heat transfers from the gas cooler and the outlet compressor pressure.

The following while loop uses the Brennen method to change the mass flow rate out of the motive nozzle in the ejector, $\dot{m}_c$. It changes the vapor quality until $\dot{m}_c$ is within the tolerance for $\dot{m}_{gas}$, which now is set as almost equal til $\dot{m}_{dot}$. The tolerance for this while loop is the same as the previous one. All of the passive loop values are calculated within this while loop.

To look at the effect of different flow areas in the motive nozzle in steady state, the flow area is changed from 1.5E-07 m^2 to 2.2E-07 m^2 in 0.1E07 m^2 increments. The diameters are shown in table 2. Since $\dot{m}_c$ is set to change the vapor quality until $\dot{m}_c$ is within a tolerance of $\dot{m}_{gas}$, the high-pressure part of the cycle is not relevant to look at. The interesting part of the results will be what happens in the passive loop.

Area [m]	1,5E-07	1,6E-07	1,7E-07	1,8E-07	1,9E-07	2,0E-07	2,1E-07	2,2E-07
Diameter [mm]	0,43702	0,45135	0,46524	0,47873	0,49185	0,50463	0,51709	0,52926

Table 2: Table showing different areas of motive nozzle that is tested

Unlike in Modelica, the ejector efficiency is not set at a constant value. In Modelica, it is set to 20%. It is not set in the mathematical model so that it can be calculated and looked at for different flow areas. The changes in flow area were chosen based on testing for the limits of the calculations; it showed that vapor quality would be too high or too low for other values than this.

3.4 Uncertainty analysis

There is no active hardware in the passive loop because the system has to be controlled from the surface. Therefore, the sensors used in the passive loop are the only measurement of how well the system performs in the passive loop. To ensure that the system is running on the suitable parameters, there needs to be an evaluation of how precise the sensors should be.

A part of this thesis examines the effects of measurement errors to evaluate the sensors. To evaluate the effect of the error, the program REFPROP has been used.

A bad sensor will not properly measure the real properties of the fluid. If the errors are significant enough, this could lead to under-compression or over-compression since the compressor is used at the design point. It could also lead to the system failing to reach the desired cooling effect. Several different types of errors can occur in a sensor. The first is a zero-point error where the starting value for the error is not set correctly. The next type of error is span error, where the increments between each value are offset. The last is non-linearity, meaning that the increments between values are different. Lukat (2021). In sensors, it is also important to separate between the accuracy and precision of a measurement. Accuracy is how close a value is to the true value, and precision is how close it is to the other measurements. The error types evaluated here are zero-point errors with poor accuracy.

Different types of sensor error are evaluated in this assignment, given an assessment of how precise sensors the test rig should have.

3.4.1 Temperature difference

The first six sensors have a temperature error of 0.1 K, 0.5 K, and 1 K. A overview and numbering are given in table 3. The choices for the temperature accuracy is based on Lucas and Koehler (2012).

Name	Error
Sensor 1	Δ T = +0.1 K
Sensor 2	Δ T = -0.1 K
Sensor 3	Δ T = +0.5 K
Sensor 4	Δ T = -0.5 K
Sensor 5	Δ T = 1 K
Sensor 6	Δ T = -1 K

Table 3: List of sensors with different temperature errors

Thermocouple type K are the most common temperature sensor because they are inexpensive, accurate, reliable, and have a wide temperature range. They are made with a combination of nickel-chromium or nickel-alumel. Two resources are used to determine the typical accuracy for these. The first source states that for type K, the standard accuracy is whichever is the greatest of +/- 2.2C or +/- 0.75% (Thermocoupleinfo.com (2023)). The second source used the accuracy 0.5 to 5.0 °C (www.rs-components.com (2023)). This may vary from the different manufacturers.

Another type of temperature sensor is platinum resistance made with platinum rhodium -13% or platinum. It is more accurate and stable than other temperature sensors, making it more expensive. The first source states that the accuracy is whichever is the greatest of +/- 1.5 °C or

+/- 0.25% (Thermocoupleinfo.com (2023)). The second source uses an accuracy of 0.1 to 1 °C (www.rs-components.com (2023)).

3.4.2 Pressure difference

The first six sensors have a pressure error of 10kPa, 50kPa and 100 kPa. A overview and numbering is given in table 4. The choices of errors are also based on the accuracy from Lucas and Koehler (2012).

Name	Error
Sensor 7	Δ p = +10 kPa
Sensor 8	Δ p = -10 kPa
Sensor 9	Δ p = +50 kPa
Sensor 10	Δ p = -50 kPa
Sensor 11	Δ p = +100 kPa
Sensor 12	Δ p = -100 kPa

Table 4: List of sensors with different pressure errors

There are several types of pressure sensors. Two actual pressure sensors that are relevant to compare are the CS-HTP Miniature High-Temperature Pressure Sensor and the CCT pressure/ temperature sensor.

The CS-HTP is a miniature high-temperature pressure sensor. It can withstand pressures up to 30 000 psi and is used for test stands, autosports, and cryogenics. It has an accuracy of $\pm$ 0.15%. 0.15% of 90 bar is 0.135 bar (sensors (2023)).

The CCT sensor ranges from 1-100 bar and is usually used in air-conditioning systems with a heat pump or thermal management. It has an accuracy of $\pm$ 0.5 %. To compare this to the high-pressure side of this heat cycle, 0.5% of 90 bar is 0.45 bar (Ampenol company (2023))

3.5 Validation of results

To look further into the uncertainty analysis, this section will look at how the errors in pressure and temperature affect the heat exchanged in the gas cooler. Calculating this for the internal heat exchanger is not feasible since one side of the heat exchange is set in the two-phase state. In the two-phase state, the effects of temperature will affect the pressure simultaneously.

This analysis is based on the refrigerant side of the gas cooler. The water side would be marginally affected by the changes in pressure; therefore, the pressure sensors would not be notable to investigate. For the refrigerant side in the gas cooler, the specific heat capacity changes with the temperature, it is therefore more significant to investigate given the sensors errors chosen.

The method used in this thesis is based on the article "Describing the Uncertainties in Experimental Results" from Moffat (1988). The true value of a measurement is unknown; therefore, an assessment of the uncertainty has to be done. The best estimate of a measured value will be $X_i = X_{i,measured} \pm \delta X_i$ where δX_i is the uncertainty. It is common to give the uncertainty within a confidence interval of 95 %. The uncertainty is based on the standard deviation, σ, set by $\pm 2\sigma$.

In uncertainty analysis, there are two essential factors, the precision index and the bias error. The precision index is an estimate of the standard deviation of the mean of a number of measurements and may vary for different experiments. The bias is also called the fixed error and represents the limit of each measurement. The manufacturer usually supplies this number. The overall uncertainty is calculated as the root of the sum square bias and the precision index. As this thesis does not have any experimental data validation, the uncertainty will only be done for the bias, as this is the set error in the sensors.

The sensors presented in table 39 and 40 will be combined to look at the total uncertainty in the cooling capacity. The temperature differences tested are $\Delta T = 0.1K$, $\Delta T = 0.5K$ and $\Delta T = 1K$. The pressure differences tested are $\Delta p = 10kPa$, $\Delta p = 50kPa$ and $\Delta p = 100kPaK$. This will give insight into what type of sensor it is important that has the most precision.

This thesis has not looked at differences in mass flow meters; for this calculation, an uncertainty of $\pm 0.2\%$ is used. The values used are the mass flow rate $\dot{m} = 0.08887$ kg/s and deviation in mass flow rate $\delta \dot{m} = 1.7774\text{E-}05$ kg/s. This value will be the same for all of the calculations.

The refrigerant side is calculated by $\dot{Q} = \dot{m}_{ref}(h_2 - h_1)$ and the overall uncertainty in cooling capacity is based on the following:

$$\delta \dot{Q}_{ref} = \sqrt{[(\frac{\partial \dot{Q}_{ref}}{\partial \dot{m}_{ref}})\delta \dot{m}_{ref}]^2 + [(\frac{\partial \dot{Q}_{ref}}{\partial \dot{m}_{ref}})\delta h_2]^2 + [(\frac{\partial \dot{Q}_{ref}}{\partial \dot{m}_{ref}})\delta h_2]^2} \tag{36}$$

The partial derivative are calculated as following:

$$\frac{\partial \dot{Q}_{ref}}{\partial \dot{m}_{ref}} = h_2 - h_1 \tag{37}$$

$$\frac{\partial \dot{Q}_{ref}}{\partial h_2} = \dot{m}_{ref} \tag{38}$$

$$\frac{\partial \dot{Q}_{ref}}{\partial h_1} = -\dot{m}_{ref} \tag{39}$$

Equation 36 can be rewritten to this:

$$\delta \dot{Q}_{ref} = \sqrt{[(h_2 - h_1)\dot{m}_{ref}]^2 + [\dot{m}_{ref}\partial h_2]^2 + [-\dot{m}_{ref}\partial h_1]^2} \tag{40}$$

The uncertainty at each enthalpy has to be calculated by the changes in local temperature and pressure.

$$\delta h_i = \sqrt{[\frac{\partial h_i}{\partial T_i}\delta T_i]^2 + [\frac{\partial h_i}{\partial p_i}\delta p_i]^2} \tag{41}$$

The partial derivative of enthalpy and temperature can be calculated by the following. The specific heat capacity is calculated using refprop.

$$\frac{\partial h_i}{\partial T_i} = c_{p,ref}(T_i, p_i) \tag{42}$$

The change in temperature is calculated by

$$\delta T_i = \sqrt{(1/N)^2(N\Delta t^2)} \tag{43}$$

Where N is the number of measurements and Δt is the accuracy of a single temperature sensor. The number of measurements for this calculation is 1, as they calculate the fixed error, and there are no experimental data. The partial derivative of enthalpy and pressure is calculated by the following, where Δp is the pressure error.

$$\frac{\partial h_i}{\partial p_i} = \frac{h(T_i, p_i + \Delta p) - h(T_i, p_i)}{\Delta p} \tag{44}$$

4 Results

This chapter presents the achieved results using the methods presented in the method chapter. It presents the results from the Modelica simulation, the Matlab simulation and the uncertainty analysis.

4.1 Simulated CO₂ hybrid cycle using Modelica

Figure 32 shows the log pH diagram for the simplified two-phase CO_2 Modelica cycle. The red line is the transcritical cycle, and the green line is the passive loop. The blue line shows the temperature 35 °C, and as figure 32 shows, the outlet of the gas cooler reaches that temperature when it reaches steady-sate.
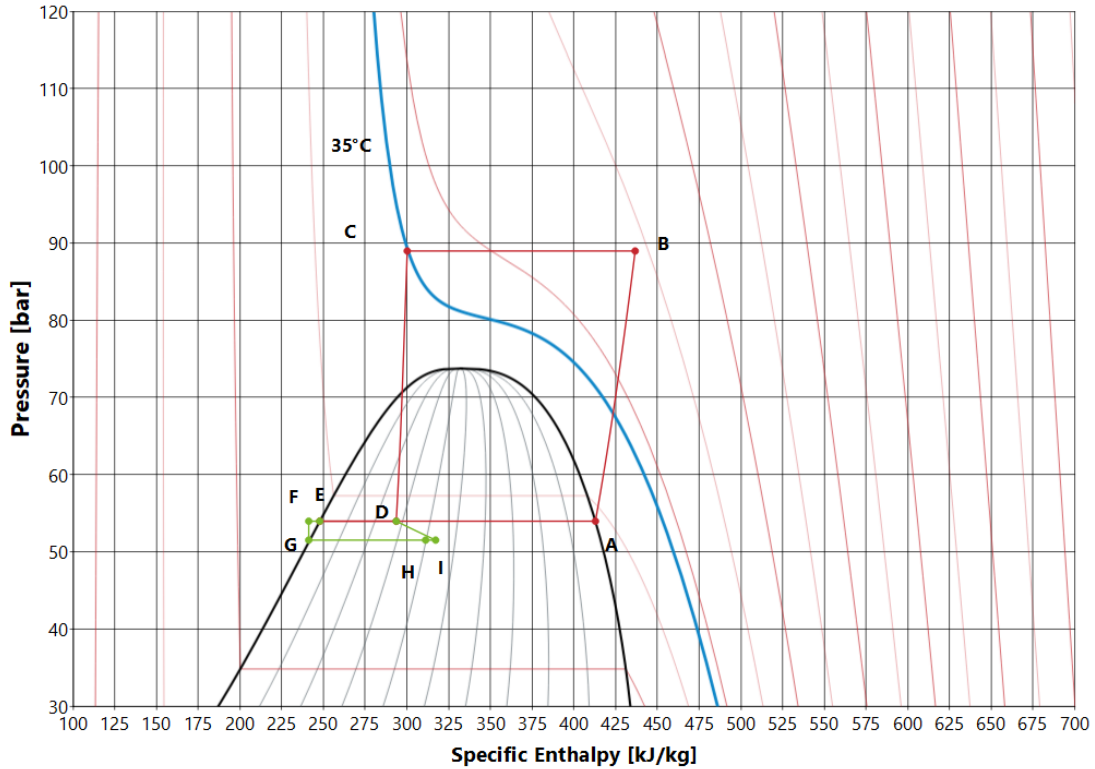
Figure 32: Results from the Modelica model
(Illustration made by Jerve 2022)

Point A to B is the compression from the liquid saturation line at 54 bar up to 88.52 bar. The compressor compresses the fluid until it reaches 88.52 bar in the supercritical state. This ensures that the outlet temperature after the gas cooler is 35 °C.

Point B to C is the gas cooler, with water on the other side. This is an isobaric process at 88.52 bar.

Point C to D is the motive for the ejector that combines the suction fluid at 51.59 bar in the mixing chamber, bringing the medium pressure to 54 bar in the two-phase region.

Points D, E, and A are the connectors to the liquid receiver, with D-A as the gas from the two-phase state. Constant pressure and temperature bring the fluid to the vapor saturation line and back to the compressor. The line from point D to E is the liquid from the liquid receiver, and it is at a constant temperature and pressure.

From E-F is the concentric line in the internal heat exchanger. The liquid is subcooled at constant pressure. The heat exchanged is $Q_{EF} = 0.0142 kg/s (247.6 - 241.6) kJ/kg = 84.96 W$

After the subcooling, the liquid is expanded isenthalpic through the capillary down to the saturation line from point F to G.

Point G to H is the supplied heat, representing the heat coming from the sensors.

Point I to H is the outer part of the concentric line in the internal heat exchanger. The liquid is subcooled at constant pressure. The heat exchanged is $Q_{IH} = 0.0142 kg/s(318.3 - 312.2)kJ/kg = 86.38W$

The model converges after about 1000 seconds of simulation, resulting in a steady-state. The efficiency of the Modelica hybrid cycle is calculated by COP and is shown to be 4.48.

$$COP_{Modelica} = \frac{\dot{Q}_{evap}}{P_{comp}} = \frac{1kW}{((435.7kJ/kg - 412.7kJ/kg)0.008976kg/s)} = 4.84 \tag{45}$$

4.2 Calculated CO$_2$ hybrid cycle using Matlab

Figure 33 shows the log PH diagram for the hybrid ejector cycle, based on the calculations from Matlab. The naming of the points are the same as the results from the Modelica model presented in chapter 4.1. A line between point I and D and between point D and A are drawn after the simulation, to show the whole cycle.
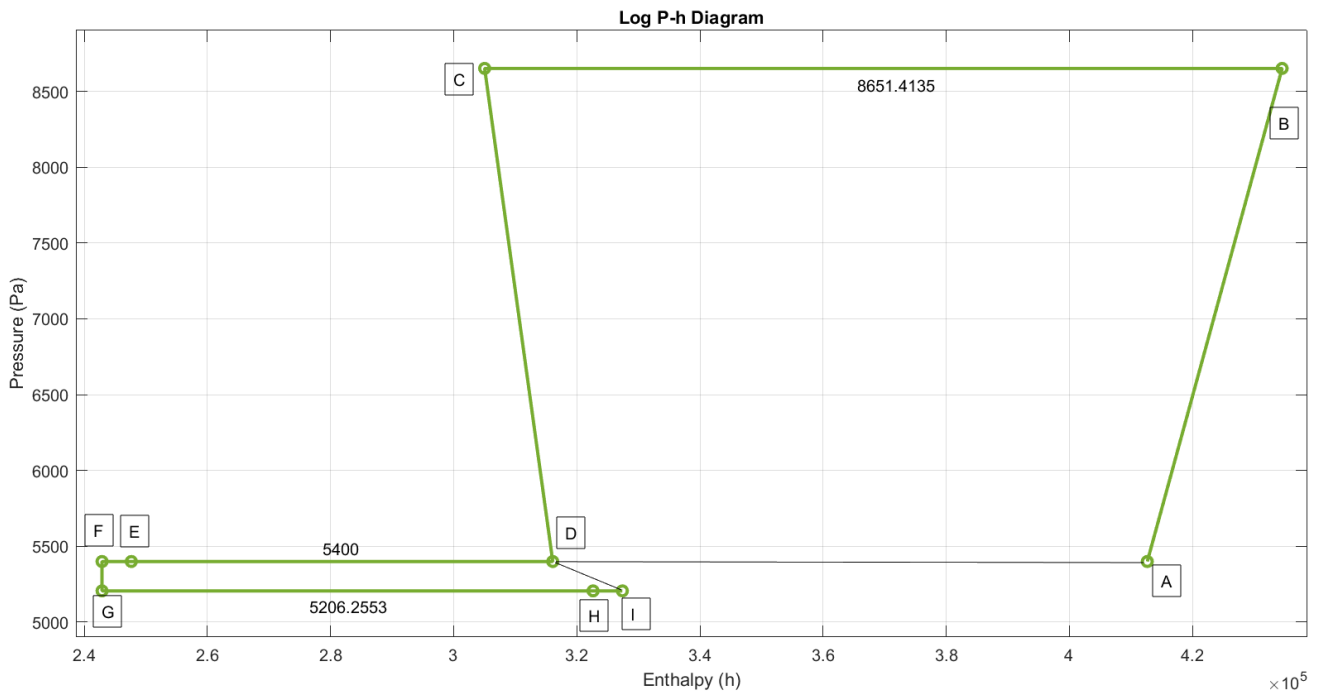
Figure 33: Results of the ejector heat pump from Matlab
(Illustration made by Jerve 2023)

The heat transferred to the gas cooler with water is 1.206 kW. The mass flow rate is the same for points A, B, and C and into the motive nozzle of the ejector. The mass flow rate is also the same for the passive loop at points E, F, G, H, and I and into the suction nozzle in the ejector. For point D, the separator, the vapor quality is 0.415 kg/kg and a combined mass flow rate from the supercritical and passive loop. The Matlab models show that the internal heat exchanger transfers a low amount of heat, close to the same amount of heat on each side.
$Q_{EF} = 0.0125kg/s(247.6 - 242.9)kJ/kg = 59.38kW$
$Q_{IH} = 0.0125kg/s(327.4 - 322.7)kJ/kg = 59.50kW$

The efficiency of the Matlab hybrid cycle is calculated by COP and is shown to be 5.14.

$$COP_{Matlab} = \frac{\dot{Q}_{evap}}{P_{comp}} = \frac{1kW}{((434.6kJ/kg - 412.7kJ/kg)0.008887kg/s)} = 5.14 \qquad (46)$$

A further calculation in table 5 shows how different correlations for void fraction would have affected the simulation. All of the correlations are presented in the theory chapter. The Pietrzak and Placzek method is used for this simulation with a slip ratio of S = 1.268.

Method	α	k_L	Speed of sound [m/s]
Pietrzak and Placzek	0,718	11627	116,6
Zivi	0,661	10707	116,8
Smith	0,855	13857	119,6

Table 5: Table of how different correlations for void fraction would have affected the simulation

Table 6 shows the output values from the Modelica model and the Matlab calculations. In the final column, the percentage difference between them is shown.

Unit	Variable	Modelica	Matlab	Difference
kPa	P_A	5400	5400	0,000 %
kPa	P_B	8852	8651	-2,271 %
kPa	P_G	5159	5206	0,911 %
kg/s	$\dot{m}_{dot}$	0,008976	0,008887	-0,992 %
kg/s	$\dot{m}_{liq}$	0,0142	0,0125	-11,723 %
kg/s	$\dot{m}_{feed}$	0,0231	0,0214	-7,519 %
-	x_D	0,388	0,4149	6,933 %
kJ/kg	h_A	412,7	412,7	-0,010 %
kJ/kg	h_B	435,7	434,6	-0,262 %
kJ/kg	h_C	301,3	305,0	1,241 %
kJ/kg	h_D	311,7	316,1	1,412 %
kJ/kg	h_E	247,6	247,7	0,020 %
kJ/kg	h_F	241,6	242,9	0,538 %
kJ/kg	h_G	241,6	242,9	0,538 %
kJ/kg	h_H	312,2	322,7	3,347 %
kJ/kg	h_I	318,3	327,4	2,862 %

Table 6: Table of resulting variables comparing the Modelica model and the Matlab model

Some values have minor differences, such as P_A and h_A, the pressure, and the enthalpy at the inlet to the compressor. Then it shows that pressure after the compressor, P_B is lower for the Matlab calculations. This affects the high-pressure enthalpies h_B and h_C, but the differences are minor at about 0.2% and 1.2%. The mass flow rate for the high-pressure loop, $\dot{m}_{dot}$, also has a minor difference, at less than 1%. In the passive loop, the differences are bigger. The biggest difference is for the liquid mass flow rate at 11%. This affects the vapor quality x_D and the mass flow rate for the feed $\dot{m}_{feed}$; they have less differences at about 7% for each. The enthalpies in the passive loop are still relatively minor, with the biggest at h_H with 3 %.

4.2.1 Changing flow area in driver nozzle

The results from the different values of flow area in the driver nozzle are presented in the following subchapter. This gives a further overview of the limitation of the calculations and the effects of a smaller flow area on the passive loop. These calculations are based on the Matlab simulation.

Figure 34 shows the results on the liquid mass flow rate by different flow areas in the motive nozzle in the ejector. The smallest mass flow rate is for the smallest area, at 0.0017 kg/s for a diameter

of 0.2185 mm. The biggest liquid mass flow rate is for the biggest area at 0.02472 kg/s for 0.2821 mm. The relation is exponential with a trend line of $\dot{m}_{liq} = 1E - 08e^{27.51d}$.
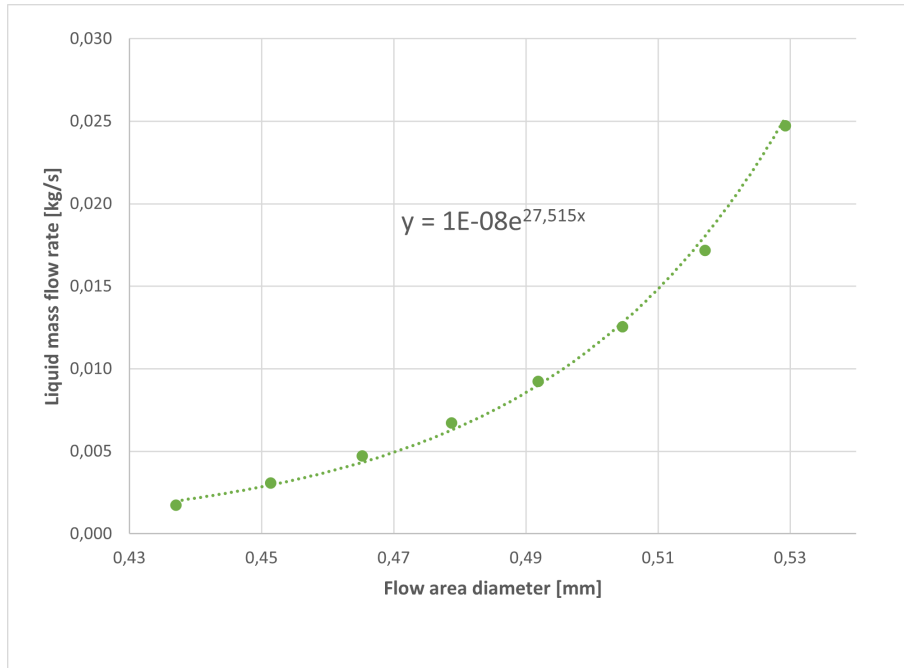
Figure 34: Scatter plot of the effect of different motive nozzle flow area on liquid
mass flow rate including a trendline
(Illustration made by Jerve 2023)

Figure 35 shows the effect of the vapor quality out of the ejector by different flow areas. The highest vapor quality is at the lowest flow diameter, with a value of $x_D = 0.8356$. The lowest vapor quality is at the highest flow diameter, with a value of $x_D = 0.2645$. The relation between the two can be described as a linear trend line of $x_D = -6.1515d + 3.5188$.
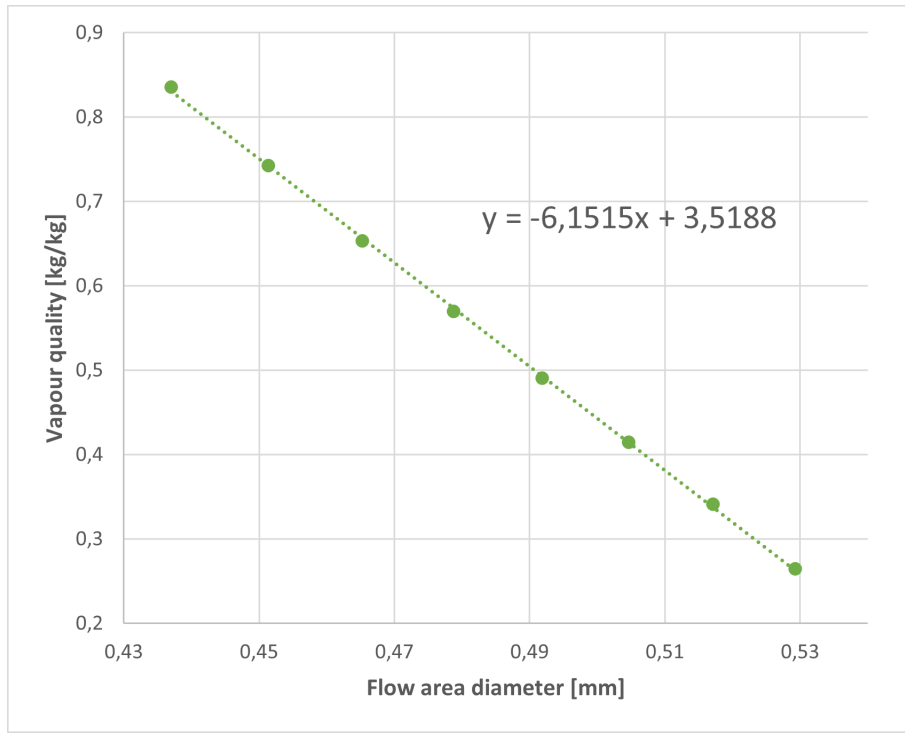
Figure 35: Scatter plot of the effect of different motive nozzle flow area on vapour
quality including a trendline
(Illustration made by Jerve 2023)

Figure 36 shows the effects of different flow areas on the enthalpies in the passive loop. It shows that h_D has a linear decreasing form, almost the same as the vapor quality. Since they are directly dependent on each other, this seems reasonable. It has quite a big difference in enthalpy, ranging from 385.52 kJ/kg to 291.28 kJ/kg. h_E is constant for all the flow areas since it only depends on the set pressure, P_A, and the liquid saturation line, which is the same for all calculations. h_F and h_G have the same enthalpy and are represented by the same plot. The difference in enthalpy is smaller than the other enthalpies, with a bigger difference for bigger flow areas than for the larger flow areas. The relation is almost constant for the areas below the original diameter, 0.2523 mm, but after the original diameter, it reduces. h_H has large differences in enthalpy for the different flow areas; for the smallest flow area, it is almost the same as h_I and at above 800 kJ/kg. For the bigger areas, it is closer to h_H and h_D. h_I follows h_H for most of the values until the biggest flow areas where h_I is somewhat higher.
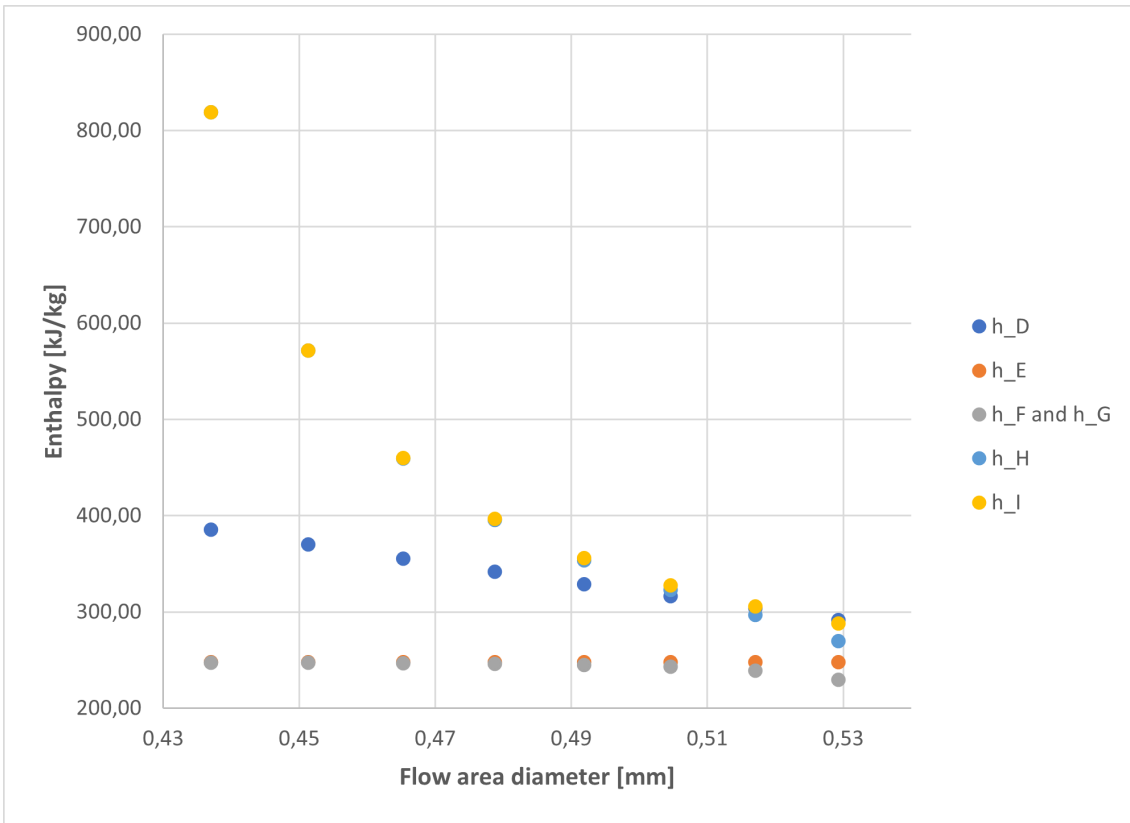
Figure 36: Scatter plot of the effect of different motive nozzle flow area on the
enthalpies in the passive loop
(Illustration made by Jerve 2023)

Figure 37 shows the relation between flow areas in the nozzle flow and the ejector efficiency. The ejector efficiency is calculated by the entertainment ratio from the liquid and gas mass flow rate and en enthalpies into the ejector. The efficiency is smallest for the smallest flow area and then exponentially higher for bigger areas, ranging from 0,2% to 91 %. The relation can be describes as $\eta_{ejector} = 1E - 14e^{59.927d}$.
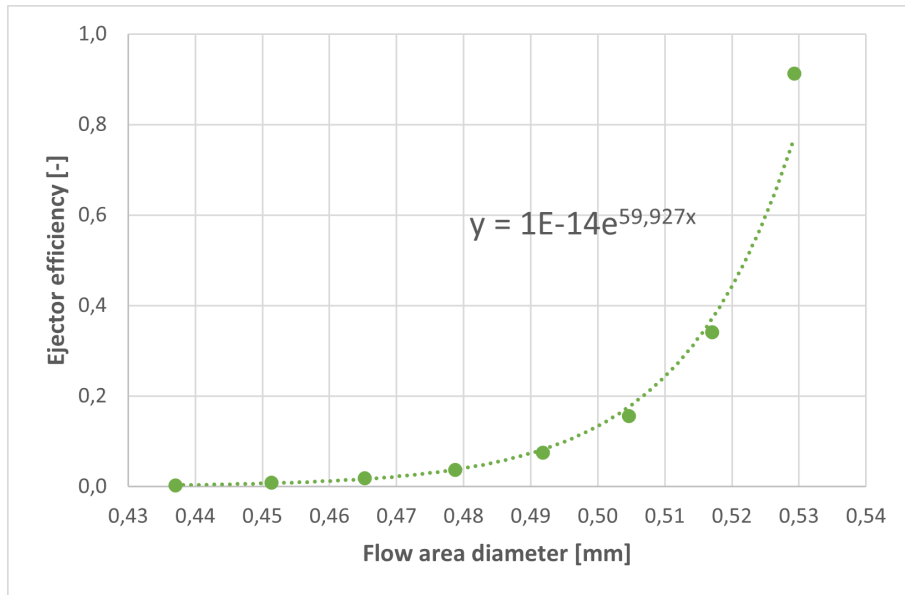
Figure 37: Scatter plot of the effect of different motive nozzle flow area on the
ejector efficiency including a trendline
(Illustration made by Jerve 2023)

Figure 38 shows the relation between flow areas in the nozzle flow and the difference in pressure in the passive loop, that is, the difference between the separator pressure and the pressure after the capillary. There is almost no pressure difference for the small flow areas, with P_G being 53.96 bar. The relation between the pressure and the flow area is exponential, and for the biggest flow area, the pressure is 46.48 bar, meaning that the bigger the flow is, the bigger the pressure difference. The relation can be expressed as $\Delta p = 2E - 10e^{54.812d}$.
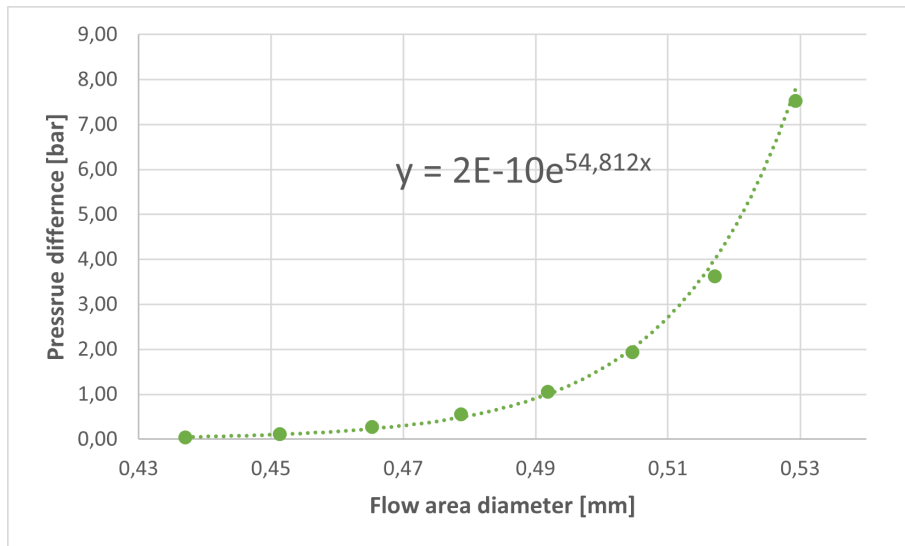
Figure 38: Scatter plot of the effect of different motive nozzle flow area on pressure
difference in the passive loop including a trendline
(Illustration made by Jerve 2023)

Table 7 shows the effect of different flow areas on the void fraction calculations and the resulting sound speed. The biggest void fraction is for the smallest flow area, this results in the highest speed of sound. The highest diameter results in the smallest void fraction, resulting in the lowest speed of sound. The speed of sound for gas at 54 bar is 199 m/s, and for liquid at the same pressure, it

is 365 m/s.

Diameter [mm]	Void fraction [-]	Speed of sound [m/s]
0,4370	0,92	155,59
0,4514	0,87	145,88
0,4652	0,82	137,29
0,4787	0,78	129,67
0,4918	0,73	122,84
0,5046	0,67	116,70
0,5171	0,61	111,14
0,5293	0,54	106,09

Table 7: Table of resulting speed of sound and void fraction for different nozzle diameters

4.3 Uncertainty analysis

This subchapter presents the uncertainty analysis results of the temperature and pressure sensors. Only a summary of the effect on the enthalpy is presented, the numbers behind the calculations can be found in the appendix B.

Changes in enthalpy given diffrent fixed errors						
Point:	ΔT = 0.1K	ΔT = -0.1K	ΔT = 0.5K	ΔT = -0.5K	ΔT = 1K	ΔT = -1K
A	0 %	-40 %	0 %	-40 %	1 %	-41 %
B	0 %	0 %	0 %	0 %	1 %	-1 %
C	0 %	0 %	1 %	-1 %	2 %	-2 %
D	33 %	-21 %	33 %	-21 %	34 %	-22 %
E	67 %	0 %	67 %	-1 %	68 %	-1 %
F	0 %	0 %	1 %	-1 %	1 %	-1 %
G	72 %	0 %	73 %	-1 %	73 %	-1 %
H	33 %	-23 %	34 %	-23 %	34 %	-24 %
I	31 %	-24 %	31 %	-25 %	32 %	-25 %

Figure 39: Table of the changes in enthalpy for different errors in temperature measurements

Table 39 shows the changes in enthalpy for constant pressure and small differences in temperature for each point as presented in 4.1. The table presents the differences in percentage compared to the original value. The colors are a gradient showing how much the enthalpy has changed and if it is positive or negative. None of the numbers are 0, but some are minuscule. These calculations will not work for the points in the two-phase state, H, G, and D. These calculations are made by changing the temperature and keeping the pressure the same as if only the temperature sensor has an error. But in the two-phase state, pressure and temperature depend on each other. For this method, the enthalpy changed to the enthalpy of the saturated lines of the temperature, so for an increase in temperature, it returned the enthalpy of the liquid saturation line. For the negative temperature error, it returned the enthalpy of the gas saturation line. The actual calculation would be that the temperature changes, so the pressure error is the same. The enthalpy should be the same regardless of the error in pressure or temperature within the two-phase state.

The set pressure and the liquid saturation line determine point A. When the temperature error is negative, there is a large difference in enthalpy because the pressure is the same, but the temperature sets into the liquid phase. For the positive temperature error, the temperature follows the pressure lines in a two-phase flow. The temperature lines are steep in the liquid phase, so the difference is large.

Both point B and C is above the critical point for CO_2, therefore the effect of temperature error follows the temperature lines where they are less steep.

Points E and G are defined by being at a certain pressure and the gas saturation line. For negative temperature errors, the points are placed into the two-phase state. For the positive temperature error, the points are in a pure gas state, and the temperature lines are close to vertical, therefore it is a big change in enthalpy.

The last point, F, is also in a single phase, the gas phase. The temperature lines are close vertical in this phase, therefore, there are small proportional changes to the enthalpy for both negative and positive errors.

Changes in enthalpy given diffrent fixed errors						
	Δp = 10 kPa	Δp = -10kPa	Δp = 50 kPa	Δp = -50 kPa	Δp = 100 kPa	Δp = -100 kPa
A	-40 %	0 %	-40 %	1 %	-40 %	1 %
B	0 %	0 %	0 %	0 %	0 %	0 %
C	0 %	0 %	0 %	0 %	-1 %	1 %
D	-21 %	33 %	-21 %	33 %	-21 %	34 %
E	0 %	67 %	0 %	67 %	0 %	68 %
F	0 %	0 %	0 %	0 %	0 %	0 %
G	0 %	72 %	0 %	73 %	0 %	74 %
H	-23 %	33 %	-23 %	34 %	-23 %	34 %
I	-24 %	31 %	-24 %	31 %	-24 %	32 %

Figure 40: Table of the changes in enthalpy for different errors in pressure measurements

Table 40 shows the changes in enthalpy for different pressure errors in the sensors. The results are invalid for points D, H, and I as they are assumed to be at either one of the saturation lines. This is because the temperature and pressure lines in the two-phase state follow each other. at point A, before the compressor, the point is determined by pressure and the vapor quality. For this calculation, the chosen temperature is difference is the same. So for negative pressure errors, the point is put inside the two-phase state, and for positive pressure errors, it is set on the liquid saturation line.

In points E and G, the effect is the opposite. When the pressure error is negative, it is measured from the liquid saturation line where it is supposed to be and into the two-phase state. For positive errors, the point is measured to the gas saturation line.

Points B and C are above the critical point and therefore experience small changes in enthalpy and are the most realistic for how the sensor error will occur. The same is for point F, which is in the liquid state and continues to be in the same state with these changes.

The figures 44, 45, and 46 in the appendix shows the changes in enthalpy for temperature in and pressure in. The sets of figures have the same starting enthalpy. The plotting sets the points with the same absolute difference, so the first point is ±0.1 K for temperature and ±10 kPa for the pressure.

4.3.1 Validation of results

The next section presents the results from the uncertainty analysis described in the method chapter. It shows that the changes in enthalpies are affected by the inaccuracy of the measurements in temperature and pressure.

All the calculations are based on the refrigerant side of the gas cooler in the model. The heat transfer rate on refrigerant side is $Q_{ref} = (435.7 - 301.3)kJ/kg * 0.008887kg/s = 1194.4W$

The first results shown in figure 41 show the uncertainty in the heat transfer rates when the temperature measurement is precise at Δ T = 0.1 K, and there are different levels of the precision of the pressure at Δ p = 10 kPa, 50 kPa, and 100 kPa. The figure shows that the less precise the measurement is, the bigger the uncertainty in heat transfer rate is.
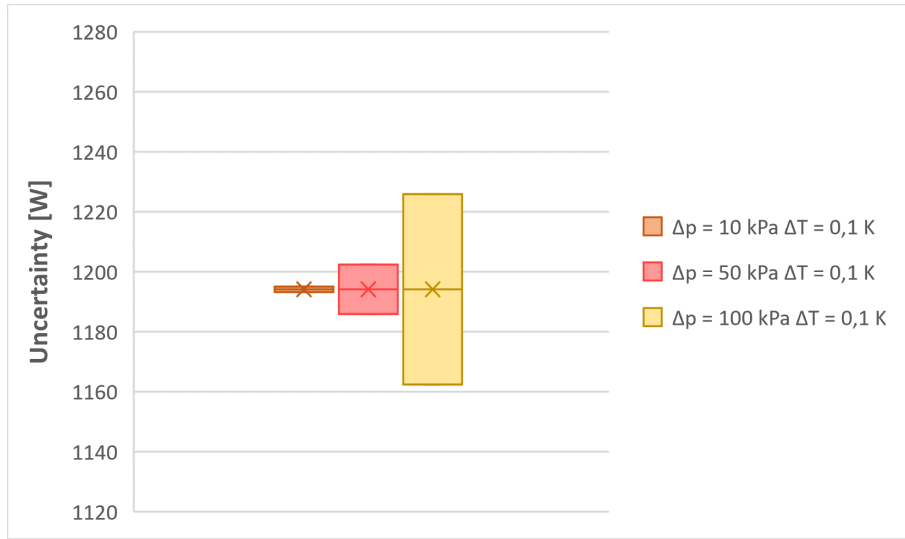
Figure 41: Boxplot showing the effect on uncertainty in heat transfer with precise temperature measurement, and different levels of accuracy of pressure measurement (Illustration made by Jerve 2023)

The next results shown in figure 41 show the uncertainty in the heat transfer rates when the pressure measurement is precise at Δ p = 10 kPa. There are different levels of the precision of the temperature at Δ T = 0.1 K, 0.5 K, and 1 K. This figure also shows that the less precise measurement, the bigger becomes the uncertainty in heat transfer rate. The scale of the two figures are the same and shows that the effect of inaccurate temperature sensors is bigger than inaccurate pressure sensors.
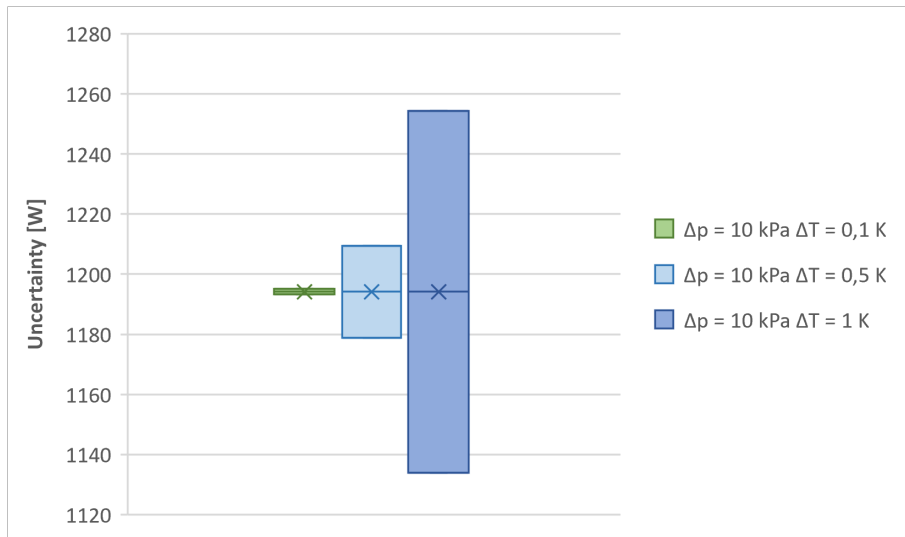
Figure 42: Boxplot showing the effect on uncertainty in heat transfer with precise pressure measurement, and different levels of accuracy of temperature measurement (Illustration made by Jerve 2023)

Figure 43 shows the effect on uncertainty for all the different combinations of temperature and

pressure sensors. The first three points are the most precise pressure sensor at Δ p = 10kPa; the next three are the middle precision pressure sensor at Δ p = 50kPa. The last three are the least precise pressure sensors at Δ p = 100kPa. The temperature sensors are in increasing order; the first point is the most precise temperature sensor at Δ T = 0.1 K, then the middle precision temperature sensor at Δ T = 0.5 K, and the third is the least precise temperature sensor at Δ T = 1 K. The order is then repeated. This plot shows the significant effect of the temperature sensors on the uncertainty in heat transfer rates.
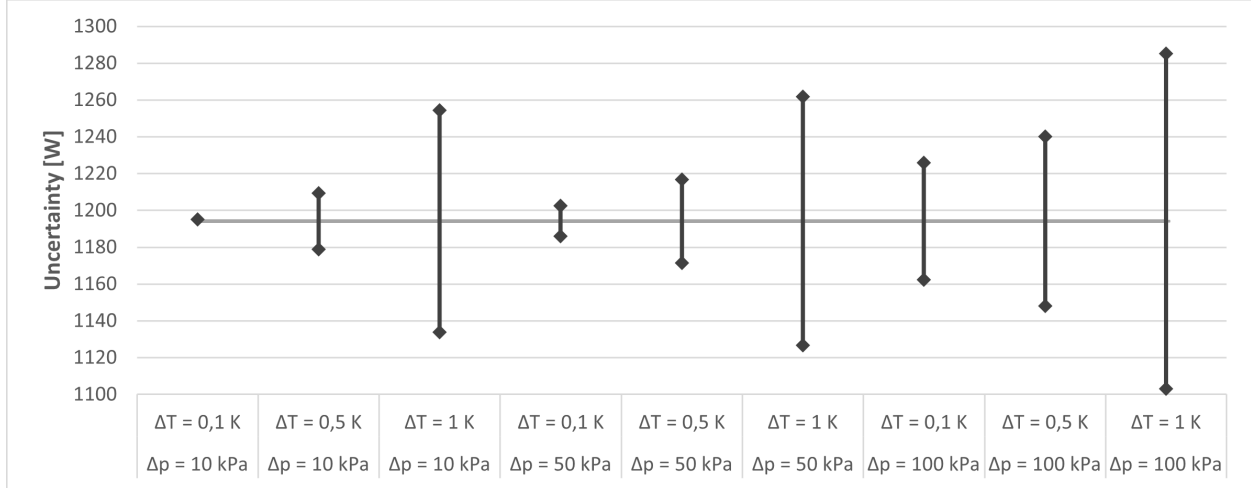
Figure 43: Plot showing the effect on uncertainty heat transfer of all combinations
or uncertainty in pressure and temperature sensors
(Illustration made by Jerve 2023)

The final result is table 8 showing all of the combinations of temperature and pressure accuracy, sorted in decreasing order. The highest value is for the greatest inaccuracy in both sensors, at 91 W and a 7.6 % difference in measurement. The smallest value is for the smallest inaccurate in both sensors, at 0.9 W and 0.1%.

Pressure accuracy	Temperature accuracy	Uncertainty [$\pm$ W]	Uncertainty in percentage
$\Delta p = 100$ kPa	$\Delta T = 1$ K	90,94	7,6 %
$\Delta p = 50$ kPa	$\Delta T = 1$ K	67,55	5,7 %
$\Delta p = 10$ kPa	$\Delta T = 1$ K	60,19	5,0 %
$\Delta p = 100$ kPa	$\Delta T = 0,5$ K	46,04	3,9 %
$\Delta p = 100$ kPa	$\Delta T = 0,1$ K	31,68	2,7 %
$\Delta p = 50$ kPa	$\Delta T = 0,5$ K	22,65	1,9 %
$\Delta p = 10$ kPa	$\Delta T = 0,5$ K	15,29	1,3 %
$\Delta p = 50$ kPa	$\Delta T = 0,1$ K	8,28	0,7 %
$\Delta p = 10$ kPa	$\Delta T = 0,1$ K	0,92	0,1 %

Table 8: Table of all the combinations of precision in temperature and pressure measurement and their effect on the uncertainty in heat transfer rates

5 Discussion

This chapter presents a discussion regarding the results from the previous chapters. The first part is about the simulation models, the Modelica model and the Matlab model, and then the differences between the two models. The next part looks at the uncertainty analysis of the sensor errors and how it affects the gas cooler.

5.1 Modelica model

As figure 32 shows, the hybrid heat pump cycle meets the system's requirements when it reaches a steady-state. The outlet of the compressor is in the supercritical area, and the outlet of the gas cooler reaches 35 °C. Then the ejector lowers the pressure, and the separator ensures that a liquid mass flow enters the evaporator at point G. Then it supplies 1kW of heat through the evaporator. To ensure this steady state, the model used pressure IDs and PI controllers for the compressors and the mass flow rate on the water side of the gas cooler.

From point E to point F, some small subcooling into the liquid phase exists. From point F to point G, there is a reduction in pressure. The reason behind the pressure reduction is the friction in the capillary and the length of the pipe. If a lower pressure is desired, the length of the pipe can be changed.

The internal heat exchanger that connects the passive loop to the high-pressure loop is small at about 85 W between points E and F and between points H and I. This heat exchanger ensures that the fluid in the capillary is in the liquid phase. The vapor quality out of the ejector is 0.388 kg/kg. The flow into the ejector from the gas cooler decreases the pressure, close to the isenthalpic process. The change in enthalpy is about 10kJ/kg.

If the pressure IDs were closer to the steady-state results, the simulation could achieve steady-state faster. The coefficient of efficiency for the simulation is 4.84, which can be considered highly efficient.

In the Modelica simulation, there as assumed few losses; the pressure losses are set to 0 for most components, except for the capillary. It does not consider imperfections in components, like inadequate insulation, refrigerant leaks, return flow into the compressor, or sensor errors.

5.2 Matlab model

The results from the Matlab calculations show that the hybrid cycle works for the given specifications. The Matlab model has a COP of 5.14, which is relatively high.

Overall the model is incomplete as it does not consider that the gas outlet of the separator goes back into the compressor. It does not consider that the efficiency is set for the ejector either. Therefore the model will likely only work for some specifications. The compressor is one of the restrictions for this, as the surge line is made for å specific range of mass flow rate. The gas cooler is also restricted as the heat transfer is set to a constant value instead of a dynamic variable based on temperatures.

The table of void fraction correlations shows that the Pietrzak and Placzek method is close to the Zivi method. The void fractions are not similar, but the resulting speed of sound is about 116 m/s. The Smith method results in a higher speed of sound, but the difference is not significant, at around 3 m/s. This method would not apply to this method of simulation. With an increase in velocity through a set flow area, the mass flow rate would increase, but the mass flow rate sets this out of the gas cooler. Therefore the vapor quality would increase too much in this simulation to try to compensate for the increase in the velocity.

5.3 Difference between Modelica and Matlab model

Mathematical calculations from the Matlab simulations are similar to the steady-state simulation of the Modelica model.

As described in the results chapter, some points have a minimal difference in the two simulations because those points are set but values independent of the previous variables. Point A is set by the starting pressure and the gas saturation line, and this does not change. The same is the case for point E, which is set by the starting pressure and the liquid saturation line. The slight difference in the enthalpies is most likely due to rounding error.

There is a more significant difference in the compressor outlet pressure, by 2.3% and about 2 bar. The mass flow rate in the compressor is quite similar, at less than 1% difference. Therefore, the difference in pressure error is most likely due to the surge line relation made for the compressor. The calculation should have been made on an actual surge line for the compressor to achieve a closer result, not based on the experimental results from the Modelica simulation. For a compressor in a test facility, more information would be available about the compressor. This difference in outlet pressure causes the differences in enthalpy at the outlet of the gas cooler.

There is also some uncertainty in the calculations for the gas cooler; as of this method, it is not set as a variable but calculated separately. The LMTD is assumed from previous temperature calculations and not a dynamic variable as it would be in the Modelica model.

The most significant difference is in the liquid mass flow rate in the passive loop, at 11%. As the mass flow rate in the compressor, after the gas cooler and out of the motive nozzle, is set to be the same and is close to the Modelica simulation, this difference comes from the error in the vapor quality out of the ejector. This has a difference of about 7%. This value is set as the changing value in the while loop, where the mass flow rate in and out of the motive nozzle is set to be the same. The calculations use the Brennen method to calculate the speed of sound in the two-phase flow. This is the same method used in Modelica, but in the documentation for Modelica, there is no specification of how to calculate the void fraction. There are different methods of doing this, and the one chosen for this simulation might not be the most precise. The calculation is also not constrained by the ejector efficiency.

The most significant differences between the two models are related to the effect on the vapor quality. This primarily affects the passive loop as the compressor sets the mass flow rate in the high-pressure loop.

There is also a pressure difference in the capillary. The low pressure in the Matlab system is about 1% and 0.5 bar, different from the Modelica model. Previous calculations show that the method is close correct if the mass flow rate is correct. Another effect is not using the proper kinematic viscosity and density value. The difference is presented in the method chapter, table 1, which shows that the difference is relatively small, at 2%. The kinematic does not have a big difference, as it is only used in the calculation of the Reynolds number and then in the calculation of the friction coefficient, which is used in the pressure loss equation. The density has a more significant effect as this is used both in calculating the Reynolds number and in pressure loss calculation.

The most significant change in enthalpy in the passive loop is seen at the outlet of the evaporator and the internal heat exchanger outlet. This is caused by the increase in the liquid mass flow rate, which is used to calculate the exit enthalpy of the evaporator h_H. This, in turn, affects the exit enthalpy of the internal heat exchanger, h_I.

The comparison shows that the amount of heat transferred in the internal heat exchanger is different for the two models, at about 85 W for the Modelica model and 59 W for the Matlab model. The difference in liquid mass flow rate causes the difference. The differences in enthalpies are closer for the Modelica model: $\Delta h_{EF} \approx \Delta h_{IH} \approx 6kJ/kg$ and for the Matlab model $\Delta h_{EF} \approx \Delta h_{IH} \approx 4.75kJ/kg$

Another advantage of the Modelica model that could be improved in the Matlab model is that the Modelica model has implemented the physical limits that a heat cycle presents. For example, the vapor quality could never become negative, and the pressure out of the compressor could not be lower than the input pressure. Some of these limitations are considered in the Matlab model since it uses the library refprop that includes limitations of its calculations.

5.4 Effect of changing flow area

The different areas in the motive nozzle affect several variables in the heat cycle. As the separator is not connected to the compressor, it does not affect the first three points in the high-pressure loop. The mass flow rate in the compressor, out of the gas cooler, and out of the motive nozzle in the ejector are set to be the same in the Matlab simulation. Therefore the vapor quality is adjusted

until the mass flow rate out of the motive nozzle is the same as into the motive nozzle. This means that this mass flow rate is constant for all areas. Therefore the variable that is adjusted is the liquid mass flow rate.

Since the mass flow rate in the motive nozzle is set to be the same, the main effect of changing area is the velocity, by the formula $\dot{m} = \rho V A$. The change in the vapor quality changes the velocity. There are no changes in the density since this is based on the entropy into the ejector, and point C remains the same for all these calculations.

The liquid mass flow rate is related to the gas mass flow rate through the entertainment ratio. The entertainment ratio, μ is the liquid mass flow rate divided by the gas mass flow rate. The vapor quality is a function of the entertainment ratio; if the entertainment ratio increases, the vapor quality decreases. The figures 34 and 35 show how the vapor quality and liquid mass flow rate are related. As the flow area diameter increases, the liquid mass flow rate also increases. The relationship between the liquid mass flow rate, the entertainment ratio, and the gaseous mass flow rate are not linear; therefore, the trend line is presented as exponential. The vapor quality is an effect of the liquid mass flow rate. Since there is a linear relation between those and the gaseous mass flow rate, the figure shows a linear relation. It shows that for an increasing flow area diameter, there is an increase in the vapor quality.

The following figure in the results chapter was the changes in enthalpies in the passive loop. The enthalpy in point D is set by the separator pressure and the vapor quality calculate the enthalpy h_D. Therefore, the relation only depends on how the vapor quality changes with the flow area. As the figures show, it is a linear decrease as the flow area increases, the same as the vapor quality. The same pressure is used to calculate h_E, and that is on the liquid saturation line. This is constant for all the calculations. h_G is calculated similarly; it is on the liquid saturation line but at the reduced pressure after the capillary. For the Δp calculations, the liquid mass flow rate is used; therefore, the enthalpy of point G changes with the flow area. Figure 38 shows an opposite relation from the Δp, where the change is small for a small flow area and increases with bigger relations. h_F is isenthalpic from point h_G, the enthalpy will therefore be the same. h_H is the exit from the evaporator. It is affected by the lower liquid mass flow rate for small flow areas. As the heat load supplied to the evaporator is set, and the enthalpy in point G has minor differences for the changes in flow areas, the enthalpy in point H has to compensate to cover the heat load. This sets the enthalpy far into the gaseous phase at above 800 kJ/kg. The enthalpy decreases exponentially for more significant liquid mass flow areas, opposite of the liquid mass flow and flow area relation. The same relation can be seen for h_I as it has the exact enthalpy change from point H, that point E has to point F. For the most significant flow areas, the liquid mass flow rate increases the heat exchanged in the internal heat exchanger, as is shown in the figure.

The ejector efficiency has been set as a free variable in this model, unlike the Modelica model. The efficiency is based on the specific enthalpies, the isentropic enthalpies, and the mass flow rate into the motive and suction nozzles. All of the variables for the motive nozzle are the same for all of the calculations, so the most significant change in efficiency comes from the change in liquid mass flow rate, where it is possible to see that the relationship is quite similar. An increase in flow area increases the ejector efficiency exponentially. This is also the same relation for the pressure difference in the ejector.

As previously described is, the relation between area and mass flow rate that if the mass flow rate is constant and the area increases, the velocity must decrease. This is the effect seen in the table 7 where the speed of sound decreases. The void fraction also decreases. They both have a linear decrease, which seems reasonable as the flow area increases linearly, and the same effect is seen in the vapor quality. This closely resembles the results from Aursand et al. (2013) where the model is a two-phase model with full chemical equilibrium and no slip, $c_{tf,\mu_g=\mu_l}$. The simulation is calculated with some slip; this slip ratio is 1.2, and, therefore, reasonable that the results are similar to no slip where the slip ratio is 1.

The overall reflection of the different flow area diameters is that the difference in area is relatively small and still changes the system a lot. The enthalpies of the internal heat exchanger are incredibly high, the ejector efficiency reaches almost 100%, and the vapor quality covers almost the whole two-phase state from above 0.8 to below 0.3. This means that even though the model is quite

similar to the Modelica model for steady state, it is not applicable as an adjustable position nozzle ejector. There are several ways this could be improved, to connect the gas outlet of the separator to the compressor to complete the cycle. The ejector efficiency should also be set as a requirement for the ejector loop. Another aspect of this calculation could have been to look at the flow coming through an adjustable position nozzle. For this model, it is assumed to be a full flow with slip. This might not be the case for an actual case of an adjustable position nozzle. The model does not consider the increase in friction losses due to the higher surface area of the positioning needle. Even though it is a flawed model for an adjustable position nozzle, most of the effects are the same as other experiments have shown previously.

An adjustable position nozzle is often used to control the system, especially during start-up and shut-down. As described in the theory section, this will be especially important in the collision point so as not to harm the sensors; it will require a slow and constant shutting down of the system. Both of these simulations are steady-state; they, therefore, are not applicable to describe the start-up of a system. However, the simulation has shown that the model for the adjustable position nozzle would not help control the system since such small changes result in significant changes. Other control strategies would provide more control over the system. Some methods involve charging the system, like a sequential start-up, where the components are started in a specific order. This can be after a charging process like the plan is for the Krypton cycle. This ensures that the refrigerant out of the compressor is in the transcritical state. Another control strategy is to use sensor-based control to regulate the start-up; this can be done by setting limits to avoid extreme conditions.

5.5 Uncertainty analysis

Firstly a look at the direct effects of errors in sensor readings. For point A, at the gaseous saturation line, a negative error in temperature reading will register the enthalpy at the same pressure but on the opposite side of the two-phase dome at the liquid saturation line. The same would happen for a positive pressure error. The same effect can be seen for the points at the liquid saturation line, points E and G. For a positive temperature error and a negative pressure error, the enthalpy would register it at the vapor-saturation line. This would provide confusing results but can be prevented by installing an instrument to measure steam quality to evaluate the state. It is also reasonable to assume that this error would be detected for an in-person experiment as a sight glass would indicate what state the fluid is in. This type of error is more critical to eliminate if the sensor readings are used directly in a simulation.

For the points in the two-phase state, points D, H, and I, the effects on enthalpy is great for all types of pressure. This is because the pressure and temperature lines are the same in this area. The resulting enthalpies are therefore based on the saturation lines. This means that for these three points, there can not only be temperature and pressure sensors; recalculations must be done based on the heat load through the system. Then it is possible to calculate the vapor quality as a function of pressure and enthalpy.

For point B, which is the output of the compressor, the results show that if the temperature error is positive, the compressor will over-compress the fluid and under-compress if the temperature error is negative. If the error is negative, the effect is smaller than with a positive error. If the pressure error is positive, the compressor will under-compress so that the temperature will be too low and the pressure too high compared to the design point. The opposite will happen for the same magnitude of negative pressure error, but the difference from the design point will be minor.

Point C is the gas cooler's exit and the ejector's input. For a positive temperature error, the gas cooler would do less work than the design point, and the ejector output would end up at a higher vapor quality. This would change the outputs of the separator, but not by a lot. For a negative temperature error, the opposite would happen. The gas cooler would overcool, and the ejector output would have lower vapor quality. Under the assumption that a pressure error also wrongly measures point B, point C would still be correct. The medium pressure out of the ejector would change, but this has not been considered here.

Point F is the entry into the capillary; it is an isenthalpic decrease in pressure to the saturation line. For the positive temperature error in sensor 5, the expansion would still happen as expected, but the simulation would assume that the lower pressure is higher than it is. If there is a positing needle in the ejector controlled by the sensors, this would significantly affect the system. For a negative temperature error, the error sets point F at a lower enthalpy, and it would assume that the pressure over the evaporator would be even lower. For errors in pressure, the capillaries would still work the same way as they do in the design case, but with higher pressure for sensor 11 and a lower pressure for sensor 12.

Figures 44, 45 and 46 in the appendix C show that the greater the error, the more significant the difference in enthalpy. This means that the more precise the sensors are, the easier the passive loop is to regulate correctly without much uncertainty.

The uncertainty analysis was performed by looking at uncertainty caused by inaccurate temperature, pressure, and mass flow rate sensors. The inaccuracy for the mass flow rate has been the same for all the calculations, so it will not affect the result. Table 8 shows all the resulting inaccuracies for the heat transfer rates in descending order. The three highest values are all for the most significant inaccuracies in temperature at 1K, with other inaccuracies in pressure. This means that the accuracy of the temperature sensors has the most significant effect on the heat transfer rates. The primary concern when assessing what kind of sensors to use would therefore be to have great accuracy in the temperature sensor.

The acceptable uncertainty is usually set at a 95% confidence level according to Moffat (1988). The highest uncertainty is using the least accurate pressure sensors and the least accurate temperature sensors; this is as expected. The uncertainty is at 7.6%, which is unacceptable within the confidence level but is not a significant difference. This measurement does not take into consideration the effect of random error, therefore a uncertainty analysis should also be done with the standard deviation from experimental results.

To look at the real at the actual sensors presented in the method chapter, none of the pressure sensors has an accuracy of less than 0.1 bar for 90 bar pressure. Since it is measured in percentage, this will be lower for lower pressures. The choice of pressure sensors will still be less critical than the choice of temperature sensors. For the pressure sensors, the most critical factor is the pressure range it measures. Both of the sensors presented in the method chapter could have been used. For the temperature sensor, the most favorable option would be to select the platinum resistance sensor, as this would lead to the least uncertainty in heat transfer rates.

6   Conclusion

The original goal of this master thesis was to help set up an experimental campaign for a Xenon hybrid cycle and test how the ejector would work for different operating conditions. As the semester went on, it became clear that doing these tests in Trondheim this semester, would not be possible. Therefore the results of this Masters's thesis are more theories, specific simulations and reflections regarding the system.

The first part of this thesis is a theory section and it begins by explaining the Large Hadron Collider, the collision points where the silicon sensors are placed, and how the detectors are affected by heat and radiation. This outlines critical requirements for the heat pump system, where the controlled start-up and shut-down of the system is one of them. The other essential requirement for the system is that the evaporating part, which is placed by the sensors, is closed off most of the year because of the high amounts of radiation. This introduces the need for a passive loop entirely controlled from the surface. Since this area is closed off, this area is also highly reliant on precise sensor measurements.

The second part of the theory section looks at the current system they use at CERN. It is a CO_2 system called the 2-phase Accumulator Controlled Loop. It uses cold transfer lines to the detectors, making it possible to run the system without any active hardware components like calves or heaters in the experimental cave. This system can provide the constant cooling required for the current

system. As a part of the future upgrade of the Large Hadron Collider, there will be an increase in the capability of the number of collisions that can occur, increasing the temperature. Therefore, a new cooling system is required, and CO_2 is no longer possible since the critical temperature is too high. An investigation into other refrigerants is therefore set in motion and the most promising type of refrigerant are so far Krypton. A hybrid cycle using Krypton is therefore being developed. This system is described in detail in the theory section. This system is the basis for the Xenon test rig to be built at NTNU in the spring of 2023. Xenon is more accessible and easier to use than Krypton and gives reasonable indications of how the system works. The Xenon hybrid heat pump testing did not happen at NTNU this spring. Therefore, this thesis focuses more on the modeling of the system and uncertainty analysis of the sensors in the system. The last part of the theory chapter describes details of the ejector and an ejector with an adjustable position nozzle. The motive nozzle of an ejector reaches the speed of sound in a two-phase state. Therefore, the calculations for the speed of sound and void fraction are also described.

The calculations in the method chapter are based on simplifying the Xenon hybrid cycle; it is done by combining two of the gas coolers into one and removing an internal heat exchanger. The refrigerant is also changed to CO_2. The cycle is still transcritical and uses an ejector. A dummy load is set in as the evaporator to simulate the cooling supplied to the detectors.

The first modeling of the system is made using Modelica. It consists of a PI-regulated compressor, a water gas cooler, and an ejector that uses the high-pressure flow from the gas cooler as the motive fluid and the liquid flow from the passive loop as the suction fluid. The outlet of the ejector diffuser goes into a two-phase separator, where the gas flow goes back to the compressors, and the liquid goes into an internal heat exchanger designed as a concentric line. This is the beginning of the passive loop. In the passive loop, there are capillaries that supply a pressure drop, and then the evaporator, and then the fluid goes back to the internal heat exchanger. The high-pressure side reaches 88 bar, and the compressor suction pressure is 54 bar. The system stabilizes after 1000 seconds and is then in steady-state. The Modelica model reaches a COP of 4.84, which can be considered highly effective. It reaches the requirement of the gas cooler outlet to be 35 °C to ensure the outlet of the compressors reaches a transcritical state.

The second modeling of the system is based on numerical calculations using Matlab. All of the formulas used are presented in the method chapter, primarily based on the documentation from the Modelica model. The results from the Modelica model were used to create a polynomial equation to calculate the surge line and the relation between the pressure ratio in the compressor and the mass flow rate. This is a significant limitation of the Matlab model since it was created for a small range of mass flow rates. The calculations for the gas cooler are also not based on a dynamic LMTD, but rather the LMTD that could be calculated from the Modelica model and then implemented with the output values from the Matlab system. This is a source of inaccuracy in the model since the outlet pressure of the compressor is different in the Modelica and the Matlab model. The outlet temperature of the gas cooler is still at 35 °C. The method of calculating the speed of sound and the void fraction needed to be calculated has also affected the system. The numerical model used the vapor quality to adjust the mass flow rate out of the ejector to be the same as the outlet of the gas cooler. This leads to a significant inaccuracy between the two models in the vapor quality at 6%. The consequential error is the 11% difference in liquid mass flow rate into the passive loop. This leads to differences in all values dependent on the passive loop that are dependent on the mass flow rate. The heat transfer in the concentric lines is smaller for the Matlab model than for the Modelica model as a result. The evaluation shows that using another correlation for the void fraction would be possible, but not all of them would be applicable. The Matlab model is made for a specific steady-state system, not a general one for all operational conditions.

The next part of the thesis looked at how the numerical model would be affected by changes in the flow area in the motive nozzle to emulate a simplified version of an adjustable position nozzle. The calculations were made by changing the diameter of the flow area and interpreting the results. The first effect was that a greater flow area led to a lower velocity since the mass flow rate in the motive nozzle was set to be constant. To compensate for this, a decrease in vapor quality again led to an increase in the liquid mass flow rate. This affected all of the enthalpies in the passive loop and set some of them far out of range of the twp-phase state. This was because the heat load in the evaporator was set as a constant, so the enthalpies had to compensate. Because of this, the

pressure difference before and after the capillaries also increased with the flow area. The changes in liquid mass flow rate also changed the efficiency of the ejector, with the same exponential growth as the pressure difference and the liquid mass flow rate. All of these effects are what would be expected of an adjustable position nozzle, but the method is still not applicable. This is because there were minor changes in the flow area, but the effect set many values close to out of bounds of where the system should operate. Small changes significantly affect the system because it is created for a particular set of operating conditions. To improve the model, it would have to be changed to be a more general model, like finding the proper compression ratio for a transcritical compressor.

The last part of the thesis looked at how the system would be affected by poorly measured sensors. The thesis looks at temperature and pressure sensors; accurate measurements are critical in the passive loop as that is the best insight into the system's performance as it is closed off. Three sensors were created for temperature and pressure to test the effect of errors in measurements. The offset was $\Delta T = 0.1$ K, 0.5 K, and 1K for temperature. The pressure of the offset was $\Delta p = 10$ kPa, 50 kPa, and 100 kPa. The first evaluation showed what would happen if the temperature or pressure sensors were correct and the other had a measurement error. The results in changing the enthalpy showed that the changes in enthalpy were small for the point in a single phase (out of the compressor, out of the gas cooler, and into the capillary). For the measurements in the two-phase state (into the separator and inlet and outlet of the concentric line after the evaporator), the enthalpy calculation set the enthalpy to the other saturation line. For the points already at the saturation line (into the compressor, out of the concentric line, and out of the capillary), the results were either small where it was set in a single phase or great where the saturation line changed. Many of these errors would be detected as off since the change in enthalpy was more significant than expected, but it would be essential to consider if the results were directly used in a computer model.

The uncertainty analysis looked at how the heat transfer rate on the refrigerant side of the gas cooler would be affected by the uncertainty in temperature and pressure sensors. The results were that the temperature sensors mainly affected the uncertainty, at a maximum of 7.6% difference from the reference heat transfer rate. This is above the standard confidence level of 95%. Therefore, The recommendation is to invest more in higher-accuracy temperature sensors to ensure the most accurate results.

7   Recommendation for further work

Several things are possible to work further on the Matlab simulation. The first would be to make it an actual heat cycle by improving the calculations of the gas cooler and connecting the outlet of the separator to the compressor. This would make the model more applicable to other operating conditions.

Another recommendation would be to change the set of variable so that it could be used for the requirements for a Xenon system. This would, among other things, involve improving the compressor calculations.

With more calculations, the Matlab model could accommodate for an adjustable position nozzle, which could be very important regarding the design of such equipment in an actual test facility. Being able to narrow down and predict a more accurate design of the position nozzle could save time and cost for the project due to the position nozzle being an expensive part of the equipment.

For the uncertainty analysis, it is essential to repeat the analysis for the test facility based on the actual sensors being installed ans set in operation. Then it would be possible to establish the bias within the equipment and the overall uncertainty. This would be especially important for the passive loop, as it is only possible to validate the results by the sensors as the area is closed for most of the year.

Bibliography

(CERN), EUROPEAN ORGANIZATION FOR NUCLEAR RESEARCH (2022a). *About CERN*. URL: https://home.cern/about (visited on 10th Dec. 2022).

— (2022b). *High-Luminosity LHC*. URL: https://home.cern/science/accelerators/high-luminosity-lhc (visited on 10th Dec. 2022).

— (2022c). *Silicon Pixels*. URL: https://cms.cern/detector/identifying-tracks/silicon-pixels (visited on 11th Dec. 2022).

Ampenol company, i2s- an (2023). *CCT pressure/ temperature sensor For air-conditioning systems with heat pumps*. URL: https://www.i2s-sensors.de/products/cct-pressure-temperature-sensor.html. (accessed: 21.06.2023).

Apollinari, G. et al. (2015). 'High-Luminosity Large Hadron Collider (HL-LHC) : Preliminary Design Report'. In: *(CERN Yellow Reports: Monographs)*.

Aursand, Peder et al. (2013). 'Pipeline transport of CO2 mixtures: Models for transient simulation'. In: *International Journal of Greenhouse Gas Control* 15, pp. 174–185. DOI: 10.1016/j.ijggc.2013.02.012.

Barroca, P. et al. (2021). 'An Ultra-Low Temperature Transcritical R744 Refrigeration System for Future Detectors at CERN LHC'. In: *Appl. Sci.*

Beattie, L. et al. (1997). 'Dependence of Depletion Voltage and Capacitance on Temperature and Frequency in Heavily Irradiated Silicon Diodes'. In: *ROSE Technical Note 97/4*.

Brennen, Christopher E (2009). *Fundamentals of Multiphase Flows*. URL: http://authors.library.caltech.edu/25021/2/cabook.pdf.

Chemieingenieurwesen (GVC) Editor, Verein Deutscher Ingenieure VDI-Gesellschaft Verfahrenstechnik und (2010). *VDI Heat Atlas*. URL: https://www.academia.edu/42980131/VDI_HeatAtlas.

CHISHOLM, D. (1985). 'Two-Phase Flow in Heat Exchangers and Pipelines'. In: *Heat Transfer Engineering* 6.2, pp. 48–57. DOI: 10.1080/01457638508939624. URL: https://doi.org/10.1080/01457638508939624.

Contiero, L., P. Barroca et al. (2022). 'Krypton, applied as refrigerant for cooling of silicon detector trackers'. In: *15th IIR-Gustav Lorentzen Conference on Natural Refrigerants (GL2022)*.

Contiero, L., A. Hafner et al. (2022). 'Hybrid cycle with Krypton for cooling of future silicon detectors in HEP'. In: *Forum on Tracking Detector Mechanics 2022*.

Eckert, Michael, Michael Kauffeld and Volker Siegismund (2022). *Natural refrigerants: Applications and practical guidelines*. VDE Verlag GmbH.

Elbel, S. and N. Lawrence (2016). 'Review of recent developments in advanced ejector technology'. In: *International Journal of Refrigeration* 62, pp. 1–18. ISSN: 0140-7007. DOI: https://doi.org/10.1016/j.ijrefrig.2015.10.031. URL: https://www.sciencedirect.com/science/article/pii/S0140700715003266.

European Parliament (2014). 'Regulation (EU) No 517/2014 of the European Parliament and of the Council of 16 April 2014 on fluorinated greenhouse gases and repealing'. In: *Regulation (EC) No 842/2006 Text with EEA relevance*.

Ferrari, M. et al. (2019). 'Experimental study of consistency degradation of different greases in mixed neutron and gamma radiation'. In: *Heliyon*.

Fretwurst, E. et al. (1994). 'Reverse annealing of the effective impurity concentration and long term operational scenario for silicon detectors in future collider experiments'. In: *Nuclear Instruments and Methods in Physics Research A 342*.

Furtado, J., F. De Proft and P. Geerlings (2015). 'The Noble Gases: How Their Electronegativity and Hardness Determines Their Chemistry'. In: *J. Phys. Chem. A*.

Ghosh, S. S. (2019). 'Highlights from the Compact Muon Solenoid(CMS) Experiment'. In: *Universe*.

Jerve, Frida (2022). *Advanced experimental analysis of a small-scale prototype with noble gases for the future upgrade of the detector cooling system at CERN*. Project report in TEP4530. Department of Energy, Process Engineering, NTNU – Norwegian University of Science and Technology.

Köhler, J et al. (2007). 'Experimental and theoretical study of a CO2 ejector refrigeration cycle'. In: *Vortrag, VDA Winter Meeting, Saalfelden*.

Kong, Ning and Zhaogang Qi (2018). 'Influence of speed of sound in two-phase region on 1-D ejector performance modelling'. In: 139, pp. 352–355. DOI: https://doi.org/10.1016/j.applthermaleng.

2018.04.120. URL: https://www.sciencedirect.com/science/article/pii/S1359431118305404#b0080.

Liu, Fang (2014). *Purdue e-Pubs Review on Ejector Efficiencies in Various Ejector Systems Review on Ejector Efficiencies in Various Ejector Systems*. URL: https://docs.lib.purdue.edu/cgi/viewcontent.cgi?article=2532&context=iracc.

Liu, Fang, Eckhard A Groll and Daqing Li (2012). 'Investigation on performance of variable geometry ejectors for CO 2 refrigeration cycles'. In: 45.1, pp. 829–839. DOI: https://doi.org/10.1016/j.energy.2012.07.008. URL: https://www.sciencedirect.com/science/article/pii/S0360544212005385?ref=pdf_download&fr=RR-2&rr=7d515ec84ccb0b06.

Liu, Ye, Mengqi Yu and Jianlin Yu (2021). 'An improved 1-D thermodynamic modeling of small two-phase ejector for performance prediction and design'. In: pp. 118006–118006. DOI: https://doi.org/10.1016/j.applthermaleng.2021.118006. URL: https://www.sciencedirect.com/science/article/pii/S1359431121014265#b0155.

Lucas, Christian and Juergen Koehler (2012). 'Experimental investigation of the COP improvement of a refrigeration cycle by use of an ejector'. In: 35.6, pp. 1595–1603. DOI: https://doi.org/10.1016/j.ijrefrig.2012.05.010. URL: https://www.sciencedirect.com/science/article/pii/S0140700712001247?via%5C%3Dihub.

Lukat, Robert (2021). *The 3 Main Errors That Affect Pressure Sensor Accuracy - WIKA blog*. URL: https://blog.wika.us/knowhow/pressure-sensor-accuracy-3-errors/.

Merrill, C. (2008). 'Nitrous Oxide Explosive Hazards (Preprint)'. In: *2008 Defense Explosives Safety Seminar*.

Moffat, R. J. (1988). 'Describing the Uncertainties in Experimental Results'. In: *Experimental Thermal and Fluid Science* 1, pp. 3–17.

National Institute of Standards and Technology (2022). *NIST Reference Fluid Thermodynamic and Transport Properties Database (REFPROP): Version 10*. URL: https://www.nist.gov/srd/refprop (visited on 16th Dec. 2022).

Petagna, P., B. Verlaat and A. Francescon (2019). 'Two-phase thermal management of silicon detectors for high energy physics'. In: *Encyclopedia of Two-Phase Heat Transfer and Flow III*, pp. 335–407.

Pietrzak, M and M Płaczek (2019). 'Void fraction predictive methods in two-phase flow across a small diameter channel'. In: 121, pp. 103115–103115. DOI: https://doi.org/10.1016/j.ijmultiphaseflow.2019.103115. URL: https://www.sciencedirect.com/science/article/pii/S0301932219304665.

sensors, Core (2023). *CS-HTP Miniature High Temperature Pressure Sensor*. URL: https://core-sensors.com/sensor-types/high-temperature-pressure-sensors/cshtp-high-temperature-pressure-sensor/. (accessed: 21.06.2023).

Smith, S. L. (1969). 'Void Fractions in Two-phase flow: A correlation based upon an equal velocity head model'. In: *Proceedings of the Institution of Mechanical Engineers* 184(1), pp. 647–664. DOI: https://doi.org/10.1243/PIME_PROC_1969_184_05.

The Modelica Association (2022). *Modelica Language*. URL: https://modelica.org/modelicalanguage.html (visited on 15th Dec. 2022).

Thermocoupleinfo.com (2023). *Types of Thermocouples - Comparison of Thermocouple Types 2023*. URL: https://www.thermocoupleinfo.com/thermocouple-types.htm. (accessed: 21.06.2023).

TLK-THermo GmbH (2023a). *TIL Eff.Compressor*. URL: file:///C:/PROGRA~2/TLK/Modelica/TIL%5C%203.12.1/help/TIL_VLEFluidComponents_Compressors.html#TIL.VLEFluidComponents.Compressors.EffCompressor (visited on 7th June 2023).

— (2023b). *TIL Heat Exchanger VDI plate*. URL: file:///C:/PROGRA~2/TLK/Modelica/TIL%5C%203.12.1/help/TIL_HeatExchangers_Plate_Geometry.html#TIL.HeatExchangers.Plate.Geometry (visited on 7th June 2023).

— (2023c). *TIL Separator*. URL: ffile:///C:/PROGRA~2/TLK/Modelica/TIL%5C%203.12.1/help/TIL_VLEFluidComponents_Separators.html#TIL.VLEFluidComponents.Separators.Separator (visited on 7th June 2023).

Verlaat, B. (2005). 'Thermal performance testing of the VTCS evaporator and VELO module'. In: *NIKHEF EN05-01*.

— (2007). 'Controlling a secondary 2-phase CO2 loop using a 2-phase accumulator'. In: *International Congress of Refrigeration 2007, Beijing*.

— (2013). 'Dimensioning of CO2 cooling pipes in detector structures'. In: *Detector Mechanics Forum Oxford, 20 June 2013*.

Verlaat, B., M. Van Beuzekom and A. Van Lysebetten (2008). 'CO2 cooling for HEP experiments'. In: *Proceedings of the Topical Workshop on Electronics for Particle Physics*.

Verlaat, B., A. Van Lysebetten and M. Van Beuzekom (2008). 'CO2 cooling for the LHCB-VELO experiment at CERN'. In: *8th IIF/IIR Gustav Lorentzen Conference on Natural Working Fluids*.

Verlaat, B. and other (2017). 'The ATLAS IBL CO2 cooling system'. In: *JINST*.

Why CO2 in refrigeration (2023). URL: https://natref.carel.com/why-co2-in-refrigeration.

www.rs-components.com (2023). *Thermocouple Selection Guide*. URL: https://docs.rs-online.com/96d5/0900766b815e5302.pdf. (accessed: 21.06.2023).

Zhu, Jingwei and Stefan Elbel (2016). 'A New Control Mechanism for Two-Phase Ejector in Vapor Compression Cycles Using Adjustable Motive Nozzle Inlet Vortex'. In.

Zivi, S. M . (1964). 'Estimation of Steady-State Steam Void-Fraction by Means of the Principle of Minimum Entropy Production'. In: *Journal of Heat Transfer* May, p. 252. DOI: https://doi.org/10.1115/1.3687115.

Appendix

A Mathematical calculations

A.1 Ejector hybrid cycle script

```
hybrid_ejector.m
%Set start-point
P_A = 5400;
h_A=refpropm('H', 'P', P_A, 'Q', 1, 'CO2');

%Compressor
vol_eff = 0.7; isen_eff = 0.7; n = 50;
vol_disp = 0.0000031;
rel_disp = 0.461; %has to start here 0.45988 or 461
m_dot = 0.00879973404;
m_gas = 0;
T_goal = 35+273.15;
Q_water = 1151.4;

while abs (m_dot - m_gas) > 1e-6
        s_A=refpropm('S', 'P', P_A, 'H', h_A, 'CO2');
        d_A=refpropm('D', 'P', P_A, 'Q', 1, 'CO2');
        m_dot = vol_disp*rel_disp*n*d_A*vol_eff;
        med = sqrt((0.0376*m_dot)-0.00033087);
        PR = (0.0283 + med)/0.0188;
        P_B = P_A *PR;
        h_isen = refpropm('H', 'P', P_B,'S', s_A, 'CO2');
        h_B = ((h_isen-h_A)/isen_eff)+h_A;
        h_C = refpropm('H', 'T', T_goal,'P', P_B, 'CO2');
        m_gas = -(Q_water - (m_dot*h_B ))/h_C;
        rel_disp = rel_disp + 0.00001;
end

T_B = refpropm('T', 'P', P_B, 'H', h_B, 'CO2');
s_C = refpropm('S', 'P', P_B,'H', h_C, 'CO2');
h_C_isen = refpropm('H', 'P', P_A,'S', s_C, 'CO2');
flowArea = 2e-07;

m_c = 0;
x_D = 0.2;

step_size = 0.0001;
iteration = 1;

while abs(m_c - m_gas) > 1e-6 && iteration <= 10000
    D_liq= refpropm('D', 'P', P_A,'Q', 0, 'CO2');
    D_gas= refpropm('D', 'P', P_A,'Q', 1, 'CO2');

    my = (1/x_D)-1;
    m_liq = my * m_dot;

    h_D = refpropm('H', 'P', P_A,'Q', x_D, 'CO2');
    h_E= refpropm('H', 'P', P_A,'Q', 0, 'CO2');
    h_A_new= refpropm('H', 'P', P_A,'Q', 1, 'CO2');
    L_cap = 0.11172; % length of pipe (m)
    Di_cap = 0.0015; %pipe diamenter (m)
```

```matlab
    A_cap = pi * ((Di_cap/2)^2);
    D_F = refpropm('D', 'P', 5400, 'Q', 0, 'CO2'); %(kg/m^3)
    v_kin = refpropm('$', 'P', 5400, 'Q', 0, 'CO2') /0.0000000001;
    w = m_liq / (D_F*A_cap); %from mass rate to velocity (m/s)
    Re = (w*Di_cap*v_kin) ;
    e = 0.0001; % roughness of pipe (m)
    f = 0.25/((log10(((e/Di_cap)/3.7)+(5.74/(Re^(0.9))))))^2; % f =
        pipe friction coefficient alternative Jain Swamee
    delta_p = ((f * (L_cap/Di_cap)*(D_F/2)*w^2)) / 1000; %delta_p =
        pressure drop (kPa)
    P_G = P_A- delta_p;%
    h_G= refpropm('H', 'P', P_G,'Q', 0, 'CO2');
    h_F = h_G;
    Q_load = 1000; %kiloWatt
    h_H =  (Q_load + (m_liq*h_G))/m_liq;
    Q_EF = m_liq*(h_E-h_F);
    h_I = -((-Q_EF/m_liq)-h_H);
    s_I = refpropm('S', 'P', P_G,'H', h_I, 'CO2');
    h_I_isen = refpropm('H', 'P', P_A,'S', s_I, 'CO2');

    D_D = refpropm('D', 'P', P_A, 'Q', x_D, 'CO2');
    S = sqrt(1-x_D*(1-(D_liq/D_gas)));

    alpha = 1/(1+(S*((1-x_D)/x_D)*(D_gas/D_liq)));

    S_drive = refpropm('S', 'H', h_C, 'P', P_B, 'CO2');
    D_th = refpropm('D',  'P', P_A,'S', S_drive, 'CO2');

    kl= 2.1*alpha*(7377000)^(0.566);
    first_part = ((alpha *1 )/5400000)*D_D;
    second_part = (((1-alpha) *kl )/5400000^(1+0.566))*D_D;
    c_1 = 1/ sqrt (abs( first_part + second_part));

    m_c = flowArea*D_th*c_1;

    if x_D < 1
        x_D = x_D + step_size;
    end

    iteration = iteration + 1;
end

m_feed = m_gas + m_liq;
eff_ejector_2 = my*((h_I_isen - h_I)/(h_C -h_C_isen));
```

A.2   Gas cooler script

```matlab
gas_cooler.m
area_plate = 0.3*0.1*1.218;
phi = 35; %angle
sw = 0.75/1000; %wall thickness m
eta_w = 45; %heat conductivity steel
p_water = 300; %pressure of water
T_start = 15+273;
dh = 0.00656909 ; %hydraulic diameter
d_w = refpropm('D', 'T', T_start, 'P', p_water, 'water'); % density
```

```matlab
v_w = refpropm('V', 'T', T_start, 'P', p_water, 'water'); % dynamic
    viscosity
cp_w = refpropm('C', 'T', T_start, 'P', p_water, 'water'); %
    spesific heat capacity
Pr = refpropm('^', 'T', T_start, 'P', p_water, 'water'); %Prandtl
    number
L = refpropm('L', 'T', T_start, 'P', p_water, 'water'); %Thermal
    conductivity
Hg = ((10000 * d_w*dh^3)/(v_w^2)); %Hagen number
Nu = 0.122*Pr^(1/3)*1^(1/6)*(2*Hg*sin(2*phi))^0.374; %Nusselt
    number
alf = (Nu*L)/dh; %overall heat transfer coefficent
k = 1/ ((2/alf)+(sw/eta_w));

UA = k*area_plate;

%Calculate LMTD
T_pi = 56;
T_po= 35;
T_si = 15;
T_so = 51;
d_Ti = T_pi-T_so;
d_To =T_po- T_si;
LMTD = (d_To-d_Ti)/(log(d_To/d_Ti));
Q = UA*LMTD;
```

B   Background for the uncertainty analysis

These figures are the results for from the errors in temperature and pressure. The caulations in the uncertiany analysis is based on these tables. **Initial values**

Location	Point	Temperature [K]	Pressure [bar]	Density [kg/m3̂]	Enthalpy [kJ/kg]	Entropy[kJ/kg-K]
In compressor	A	290,66	5,4	176,11	412,7	1,7289
In gas cooler	B	329,25	8,852	242,32	435,7	1,7498
In ejector	C	308,16	8,852	650,49	301,3	1,3242
In seperator	D	290,65	5,4	336,76	311,7	1,3814
In IHX	E	290,63	5,4	798,8	247,6	1,1608
In capiliary	F	288,95	5,4	819,17	241,6	1,1401
In dummy load	G	288,69	5,159	816,59	241,6	1,1412
In IHX	H	288,73	5,159	312,92	312,2	1,3857
In ejector	I	288,73	5,159	297,06	318,3	1,4068

Sensor 1

Sensor 1	Delta T:	0,1			
Point	Temperature [K]	Pressure [MPa]	Density [kg/m3̂]	Enthalpy [kJ/kg]	Entropy[kJ/kg-K]
A	290,76	5,4	175,57	413,09	1,7302
B	329,35	8,852	241,92	435,96	1,7506
C	308,26	8,852	647,89	301,96	1,3264
D	290,75	5,4	175,63	413,05	1,7301
E	290,73	5,4	175,73	412,98	1,7298
F	289,05	5,4	818,08	241,93	1,1413
G	288,79	5,159	163,91	415,96	1,745
H	288,83	5,159	163,74	416,09	1,7455
I	288,83	5,159	163,74	416,09	1,7455

Sensor 2

Sensor 2	Delta T:	-0,1			
Point	Temperature [K]	Pressure [MPa]	Density [kg/m3̂]	Enthalpy [kJ/kg]	Entropy[kJ/kg-K]
A	290,56	5,4	799,73	247,33	1,1599
B	329,15	8,852	242,73	435,44	1,749
C	308,06	8,852	652,82	300,7	1,3223
D	290,55	5,4	799,86	247,3	1,1598
E	290,53	5,4	800,12	247,22	1,1595
F	288,85	5,4	820,34	241,25	1,1389
G	288,59	5,159	817,79	241,24	1,1399
H	288,63	5,159	817,33	241,38	1,1404
I	288,63	5,159	817,33	241,38	1,1404

Sensor 3

Sensor 3	Delta T:	0,5			
Point	Temperature [K]	Pressure [MPa]	Density [kg/m3̂]	Enthalpy [kJ/kg]	Entropy[kJ/kg-K]
A	291,16	5,4	173,61	414,54	1,7352
B	329,75	8,852	240,34	436,98	1,7537
C	308,66	8,852	637,49	304,6	1,3349
D	291,15	5,4	173,66	414,5	1,7351
E	291,13	5,4	173,75	414,43	1,7348
F	289,45	5,4	813,45	243,31	1,1461
G	289,19	5,159	162,28	417,26	1,7495
H	289,23	5,159	162,12	417,39	1,75
I	289,23	5,159	162,12	417,39	1,75

Sensor 4

Sensor 4	Delta T:	-0,5			
Point	Temperature [K]	Pressure [MPa]	Density [kg/m3̂]	Enthalpy [kJ/kg]	Entropy[kJ/kg-K]
A	290,16	5,4	804,84	245,85	1,1548
B	328,75	8,852	244,37	434,39	1,7458
C	307,66	8,852	662,16	298,3	1,3145
D	290,15	5,4	804,96	245,82	1,1547
E	290,13	5,4	805,21	245,74	1,1544
F	288,45	5,4	824,75	239,9	1,1342
G	288,19	5,159	822,37	239,87	1,1351
H	288,23	5,159	821,92	240	1,1356
I	288,23	5,159	821,92	240	1,1356

Sensor 5

Sensor 5	Delta T:	1			
Point	Temperature [K]	Pressure [MPa]	Density [kg/m3̂]	Enthalpy [kJ/kg]	Entropy[kJ/kg-K]
A	291,66	5,4	171,32	416,26	1,7411
B	330,25	8,852	238,42	438,25	1,7576
C	309,16	8,852	623,28	308,15	1,3464
D	291,65	5,4	171,36	416,23	1,741
E	291,63	5,4	171,45	416,16	1,7408
F	289,95	5,4	807,44	245,09	1,1522
G	289,69	5,159	160,36	418,82	1,7549
H	289,73	5,159	160,21	418,94	1,7553
I	289,73	5,159	160,21	418,94	1,7553

Sensor 6

Sensor 6	Delta T:	-1			
Point	Temperature [K]	Pressure [MPa]	Density [kg/m3̂]	Enthalpy [kJ/kg]	Entropy[kJ/kg-K]
A	289,66	5,4	810,96	244,05	1,1486
B	328,25	8,852	246,49	433,05	1,7418
C	307,16	8,852	673,03	295,47	1,3053
D	289,65	5,4	811,08	244,02	1,1485
E	289,63	5,4	811,32	243,95	1,1483
F	287,95	5,4	830,09	238,25	1,1285
G	287,69	5,159	827,9	238,18	1,1293
H	287,73	5,159	827,47	238,32	1,1298
I	287,73	5,159	827,47	238,32	1,1298

Sensor 7

Sensor 7	Delta p:	0,01			
Point	Temperature [K]	Pressure [MPa]	Density [kg/m3̂]	Enthalpy [kJ/kg]	Entropy[kJ/kg-K]
A	290,66	5,41	798,7	247,66	1,161
B	329,25	8,862	242,87	435,51	1,7491
C	308,16	8,862	651,22	301,16	1,3237
D	290,65	5,41	798,83	247,63	1,1609
E	290,63	5,41	799,09	247,55	1,1606
F	288,95	5,41	819,44	241,55	1,1399
G	288,69	5,169	816,86	241,55	1,1409
H	288,73	5,169	816,39	241,69	1,1414
I	288,73	5,169	816,39	241,69	1,1414

Sensor 8

Sensor 8	Delta p:	-0,01			
Point	Temperature [K]	Pressure [MPa]	Density [kg/m3̂]	Enthalpy [kJ/kg]	Entropy[kJ/kg-K]
A	290,66	5,39	175,17	413,14	1,7306
B	329,25	8,842	241,78	435,88	1,7505
C	308,16	8,842	649,53	301,49	1,3249
D	290,65	5,39	175,22	413,1	1,7305
E	290,63	5,39	175,33	413,03	1,7302
F	288,95	5,39	818,99	241,62	1,1403
G	288,69	5,149	163,51	416,01	1,7454
H	288,73	5,149	163,35	416,15	1,7459
I	288,73	5,149	163,35	416,15	1,7459

Sensor 9

Sensor 9	Delta p:	0,05			
Point	Temperature [K]	Pressure [MPa]	Density [kg/m3̂]	Enthalpy [kJ/kg]	Entropy[kJ/kg-K]
A	290,66	5,45	799,82	247,48	1,1602
B	329,25	8,902	245,06	434,77	1,7464
C	308,16	8,902	654,48	300,53	1,3215
D	290,65	5,45	799,95	247,44	1,1601
E	290,63	5,45	800,21	247,36	1,1598
F	288,95	5,45	820,33	241,41	1,1393
G	288,69	5,209	817,8	241,4	1,1402
H	288,73	5,209	817,34	241,54	1,1407
I	288,73	5,209	817,34	241,54	1,1407

Sensor 10

Sensor 10	Delta p:	-0,05			
Point	Temperature [K]	Pressure [MPa]	Density [kg/m3̂]	Enthalpy [kJ/kg]	Entropy[kJ/kg-K]
A	290,66	5,35	171,65	414,79	1,737
B	329,25	8,802	239,63	436,62	1,7532
C	308,16	8,802	646,02	302,17	1,3273
D	290,65	5,35	171,69	414,75	1,7369
E	290,63	5,35	171,79	414,68	1,7367
F	288,95	5,35	818,08	241,77	1,1409
G	288,69	5,109	160,33	417,54	1,7516
H	288,73	5,109	160,17	417,66	1,752
I	288,73	5,109	160,17	417,66	1,752

Sensor 11

Sensor 11	Delta p:	0,1			
Point	Temperature [K]	Pressure [MPa]	Density [kg/m3̂]	Enthalpy [kJ/kg]	Entropy[kJ/kg-K]
A	290,66	5,5	801,2	247,25	1,1592
B	329,25	8,952	247,83	433,83	1,7429
C	308,16	8,952	658,37	299,78	1,3188
D	290,65	5,5	801,33	247,21	1,1591
E	290,63	5,5	801,58	247,14	1,1588
F	288,95	5,5	821,43	241,23	1,1384
G	288,69	5,259	818,96	241,21	1,1394
H	288,73	5,259	818,5	241,35	1,1399
I	288,73	5,259	818,5	241,35	1,1399

Sensor 12

Sensor 12	Delta p:	-0,1			
Point	Temperature [K]	Pressure [MPa]	Density [kg/m3̂]	Enthalpy [kJ/kg]	Entropy[kJ/kg-K]
A	290,66	5,3	167,49	416,73	1,7447
B	329,25	8,752	236,96	437,53	1,7567
C	308,16	8,752	641,38	303,08	1,3305
D	290,65	5,3	167,53	416,69	1,7446
E	290,63	5,3	167,62	416,63	1,7444
F	288,95	5,3	816,92	241,96	1,1418
G	288,69	5,059	156,55	419,35	1,7589
H	288,73	5,059	156,41	419,47	1,7593
I	288,73	5,059	156,41	419,47	1,7593

C   Figures of enthalpies of point B, C and F with sensor errors
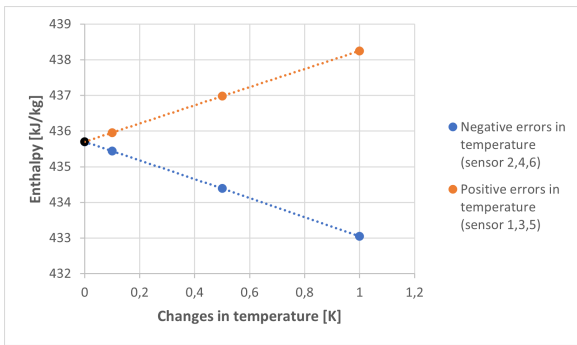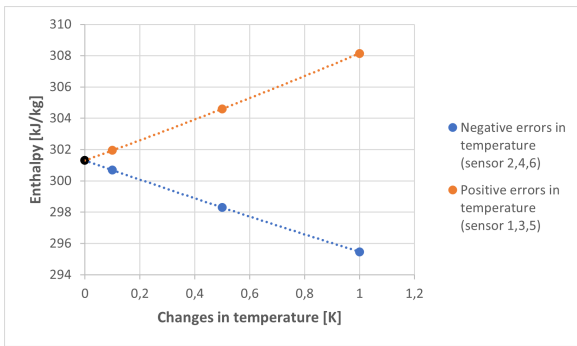

(a) Enthalpy of point B
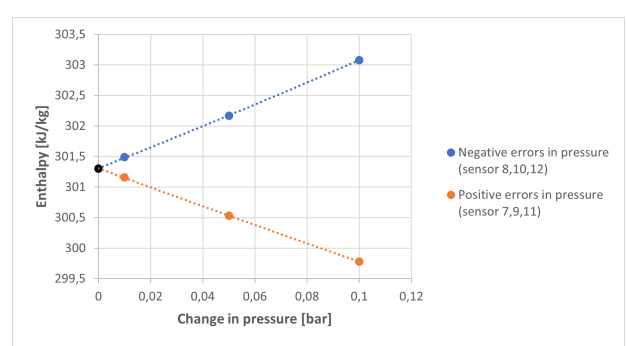for different temperature errors
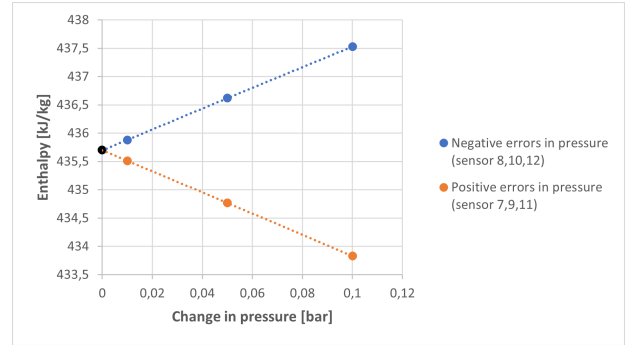
(b) Enthalpy of point B
for different pressure errors

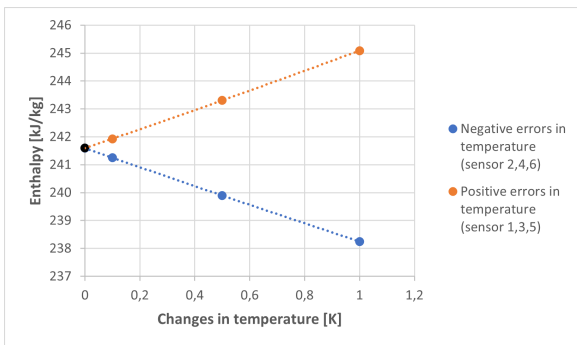Figure 44: Effect of sensor errors on point B

(a) Enthalpy of point C
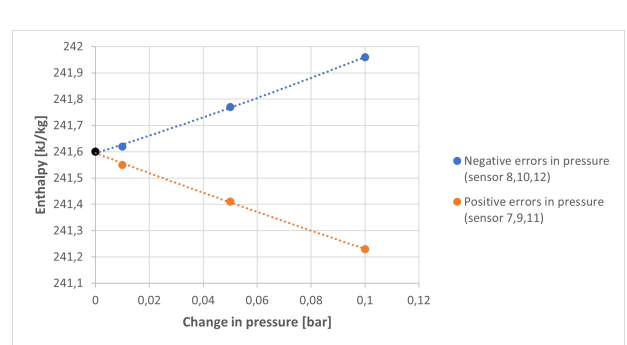for different temperature errors

(b) Enthalpy of point C
for different pressure errors

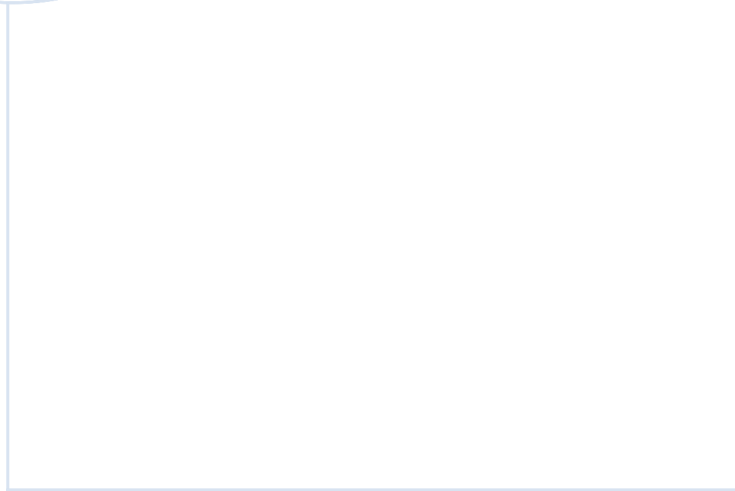Figure 45: Effect of sensor errors on point C

(a) Enthalpy of point F
for different temperature errors

(b) Enthalpy of point F
for different pressure errors

Figure 46: Effect of sensor errors on point F